2. Solar Wind Origins and Acceleration and Solar and Stellar Winds and Magnetic Activity

MHD Flow Equations (you can't escape MHD, but you can go beyond it)

$$\frac{\partial \rho}{\partial t} + \vec{\nabla} \cdot \rho \vec{U} = 0$$

$$\rho\left(\frac{\partial \vec{U}}{\partial t} + \vec{U} \cdot \vec{\nabla}\vec{U}\right) = -\vec{\nabla}\overline{\overline{p}} + \frac{1}{c}\vec{J} \times \vec{B} - \rho\vec{g}$$

$$\frac{\partial \vec{B}}{\partial t} = \vec{\nabla} \times \vec{U} \times \vec{B} + \vec{\nabla} \times \eta_m \vec{\nabla} \times \vec{B}$$

$$\frac{1}{\gamma - 1}\,\rho^{\gamma}\,\frac{\mathrm{D}}{\mathrm{Dt}}\left(P\,\rho^{-\gamma}\right) = Q - L$$

Viscosity...

Resistivity...

Viscoresistive heating

Radiation....

Whence the Solar Wind ?

Steady State Conservation Equations, Rotating Frame of Reference, neglecting centrifugal force (ok out to beyond 1 AU)

$$\nabla \cdot (\rho \vec{U}) = -\nabla \cdot < \delta\rho \, \delta\vec{U} >$$

$$\nabla \cdot (\rho \vec{U}\vec{U}) = -\nabla p^T + \frac{\vec{B} \cdot \nabla \vec{B}}{4\pi} - \rho \frac{GM_\odot \vec{R}}{R^3} - \nabla \frac{< \delta \vec{B}^2 >}{8\pi} -$$

$$-\nabla \cdot < (\rho \delta\vec{U} \delta\vec{U} - \frac{\delta\vec{B}\delta\vec{B}}{4\pi}) + \delta\rho \, (\delta\vec{U}\vec{U} + \vec{U}\delta\vec{U}) + \delta\rho \, \delta\vec{U}\delta\vec{U} >$$

Whence the Solar Wind ?

$$\nabla \cdot \left[\vec{U} \left(\frac{1}{2}\rho U^2 + \frac{5}{2}P - \rho \frac{GM_\odot}{R} \right) + \Pi_{ik} U_k + \vec{q} + \vec{S} \right] = -L_r$$

$$F_m = \int dA\, \vec{n} \cdot \vec{S} + |\dot{M}| \frac{1}{2} v_\perp^2$$

$$F_q = \int dA\, \vec{n} \cdot \vec{q} = - \int dA\, \kappa_\parallel^e \vec{n} \cdot \nabla_\parallel (kT_e)$$

$$F_r = \int_0^R dV L_r$$

$$F_{sw} = |\dot{M}| \left(\frac{1}{2} U^2 + \frac{5p}{2\rho} - \frac{GM_\odot}{R} \right)$$

$$\vec{S} = \frac{c}{4\pi} \vec{E} \times \vec{B} \qquad \vec{E} = -\frac{1}{c} \vec{V}_{ph} \times \vec{B}$$

$$\vec{S} \cdot \vec{n}_{ph} = \frac{B_\perp^2}{4\pi} \vec{V}_{ph} \cdot \vec{n}_{ph} - \frac{\vec{B} \cdot \vec{n}_{ph}}{4\pi} \vec{V}_{ph\perp} \cdot \vec{B}$$

$$F_0 = F_m + F_q + F_r + F_{sw}$$

$$U_E^2 = 2 \frac{F_{m,0} - F_{r,E}}{|\dot{M}|} - V_g^2$$

Solar wind speed and flux tube expansion

A detailed solar wind acceleration profile is obtained only by ensuring that the the velocity U also satisfy the momentum equation, and in particular that the solution smoothly pass through the critical point, where the speed becomes supersonic.

$$(U - \frac{V_T^2}{U})\frac{dU}{dr} = \frac{V_T^2}{A}\frac{dA}{dr} - \frac{V_g^2}{2}\frac{1}{r^2} \qquad r = R/R_\odot \quad r_c = \frac{1}{4}\frac{V_g^2}{\beta_c V_T^2}, \quad U_c = V_T$$

$$\beta = \frac{1}{2}\frac{r}{A}\frac{dA}{dr} = -\frac{1}{2}\frac{r}{B}\frac{dB}{dr} \qquad U_0 = V_T\frac{A_c}{A_0}\exp\left(-\left[\frac{V_g^2}{2V_T^2} + \frac{1}{2} - 2\beta_c\right]\right)$$

$$v_c^2 = v_T^2 + \frac{1}{4}\left(\frac{\rho_0}{\rho_c}\right)^{1/2}\frac{(1+3M_{Ac})}{(1+M_{Ac})^2}\langle \delta v_0^2 \rangle$$

Solar wind base speed is an increasing function of expansion factor at fixed temperature. Provided the mechanical energy flux is held constant, there is an inverse correlation of mass flux to asymptotic solar wind speed. Mass flux is proportional to speed at the coronal base, and therefore to the flux tube expansion close to the sun.

Weber and Davis 1967

:cond section presents Helios observations betw
AU, which can serve to infer the plasma and m
)arameters at the Alfvén critical point. A final

hich follow straightforwardly. Here and in the re
; paper, we restrict ourselves to the case $A = 1$,
sted by the almost isotropic total pressure fc
:h and Richter [1984].
m the equations of *Weber and Davis* [1967]
tion of (2) we then find the following expressions:

$$L_P + L_M = L = \Omega r_A^2$$

1D field aligned self consistent wind models (Lionello, Velli et al. 2014)

$$\frac{\partial \rho}{\partial t} = -\frac{1}{A}\frac{\partial}{\partial s}\left(AU\rho\right),$$

$$\rho\frac{\partial U}{\partial t} = -\rho U\frac{\partial U}{\partial s} - \frac{\partial}{\partial s}(p + p_w) + g_s\rho + \mathsf{R}_s + \frac{1}{s^2}\frac{\partial}{\partial s}\left(s^2\nu\rho\frac{\partial U}{\partial s}\right),$$

$$\frac{\partial T}{\partial t} = -U\frac{\partial T}{\partial s} - (\gamma - 1)\left(T\frac{1}{A}\frac{\partial}{\partial s}AU - \frac{m_p}{2k\rho}\left(\frac{1}{A}\frac{\partial}{\partial s}Aq - n_e n_p Q(T) + H\right)\right).$$

$$\frac{\partial z_\pm}{\partial t} = -[U \pm V_a]\frac{\partial z_\pm}{\partial s} + R_1^\pm z_\pm + R_2^\pm z_\mp - \frac{|z_\mp| z_\pm}{2\lambda_\perp},$$

$$R_1^\pm = -\frac{1}{2}[U \mp V_a]\left(\frac{\partial \log V_a}{\partial s} + \frac{\partial \log A}{\partial s}\right),\ R_2^\pm = \frac{1}{2}[U \mp V_a]\frac{\partial \log V_a}{\partial s},$$

$$p_w = \rho\frac{(z_- - z_+)^2}{8}, \qquad H = \rho\frac{|z_-| z_+^2 + |z_+| z_-^2}{4\lambda_\odot\sqrt{A/A_\odot}},$$

$$\mathsf{R}_s = \rho z_+ z_- \frac{\partial \log A}{\partial s}, \qquad p = 2nkT$$

Fast SC Models (Verdini et al./Li et al.)

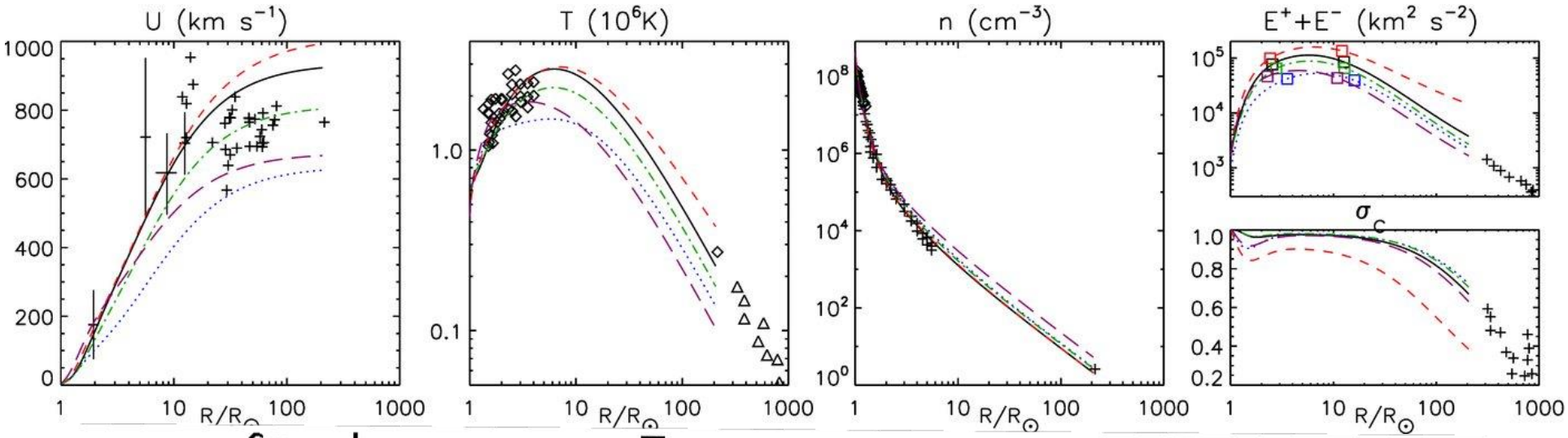

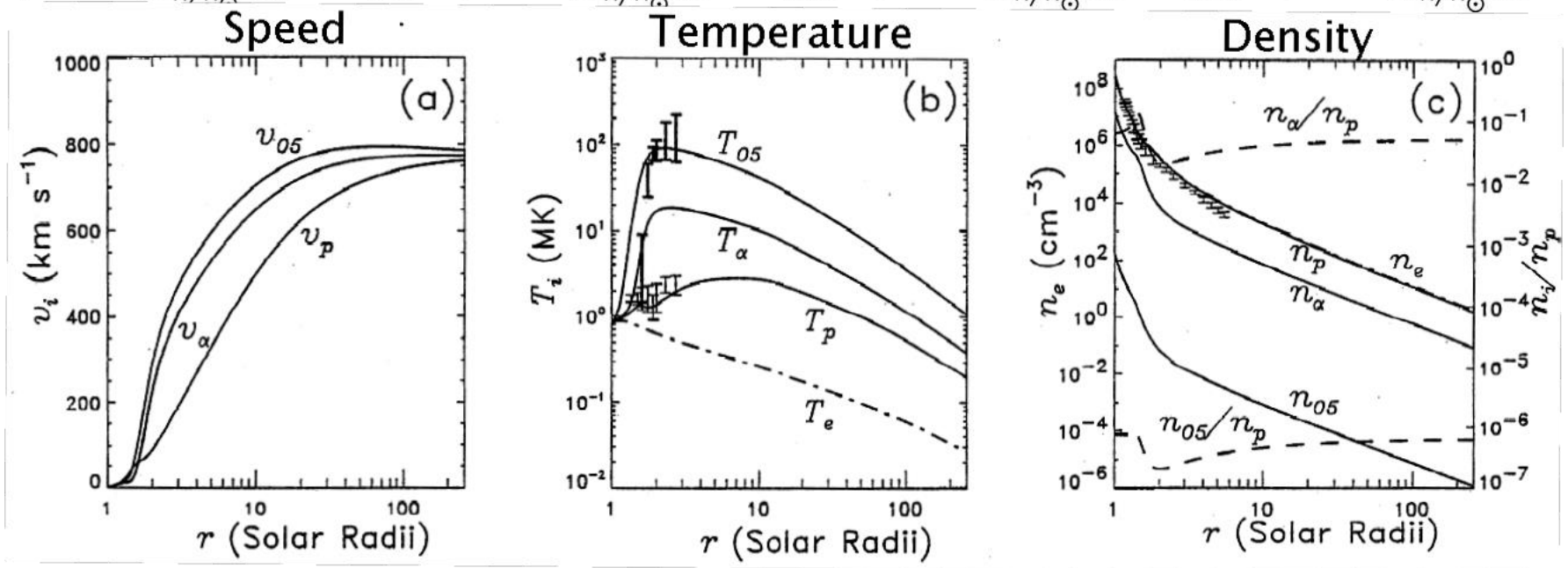

Alfvén Theorem

$$\frac{\partial \vec{B}}{\partial t} = \nabla \times (\vec{v} \times \vec{B}) + \eta \nabla^2 \vec{B}$$

$$\tau = \frac{\mathcal{L}}{\mathcal{U}} \qquad \tau_D = \frac{\mathcal{L}^2}{\eta}$$

$$\tau_D \simeq 10^{15}\mathrm{s}$$

Solar Corona

Alfvén velocity $v_A = \dfrac{B}{\sqrt{4\pi\rho}}$ $\tau_A = \dfrac{\mathcal{L}}{v_A}$ $\tau_A \simeq 10\mathrm{s}$

$$\mathcal{U} \sim v_A$$

$$S >> 1$$

Lundquist $S = \dfrac{\mathcal{L} v_A}{\eta} = \dfrac{\tau_D}{\tau_A}$

Alfvén Theorem: magnetic flux through a closed line which moves with the fluid is constant in time.

RECONNECTION PLACES

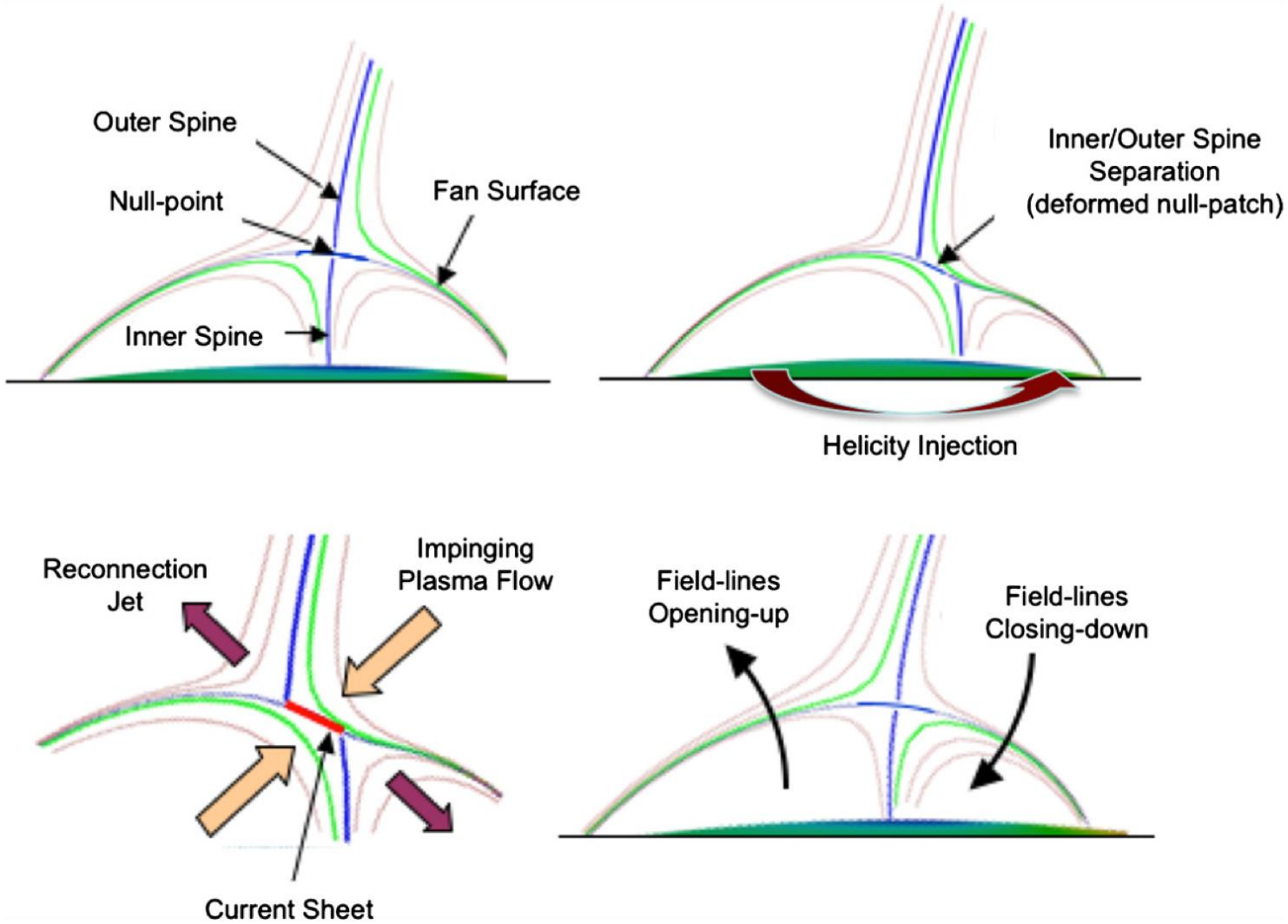

Heating the confined corona (DC)

"Reality"

Parker

Model

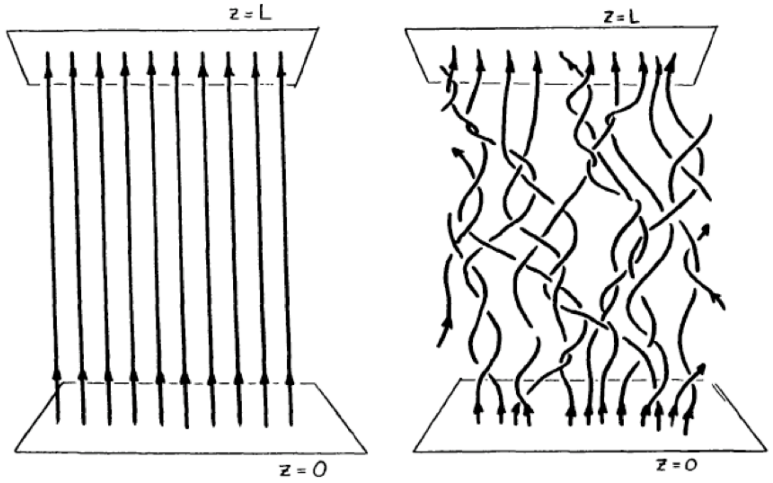

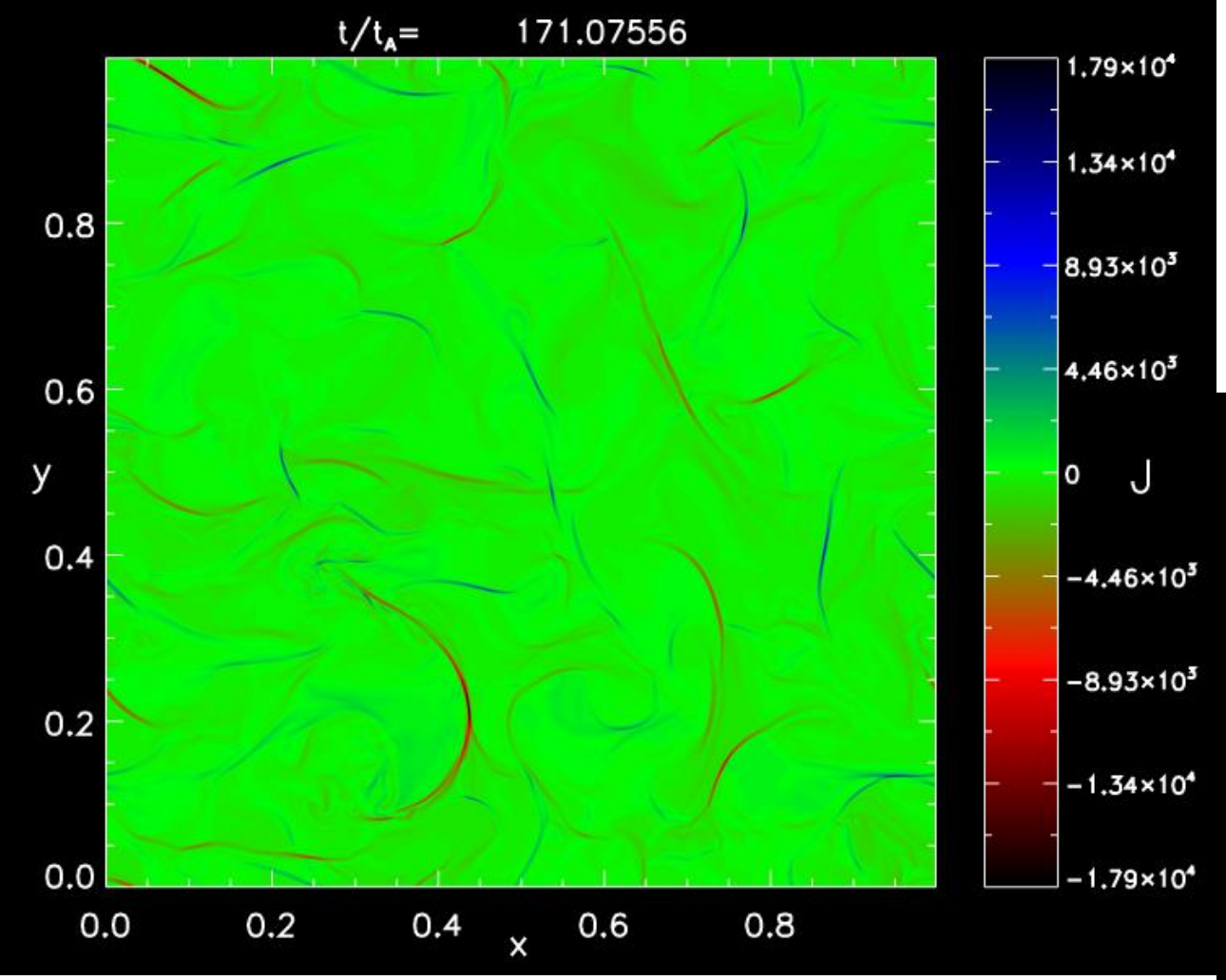
t/t_A= 171.07556
1.79×10^4
1.34×10^4
8.93×10^3
4.46×10^3
0
J
−4.46×10^3
−8.93×10^3
−1.34×10^4
−1.79×10^4
0.0
0.2
0.4
0.6
0.8
y
x

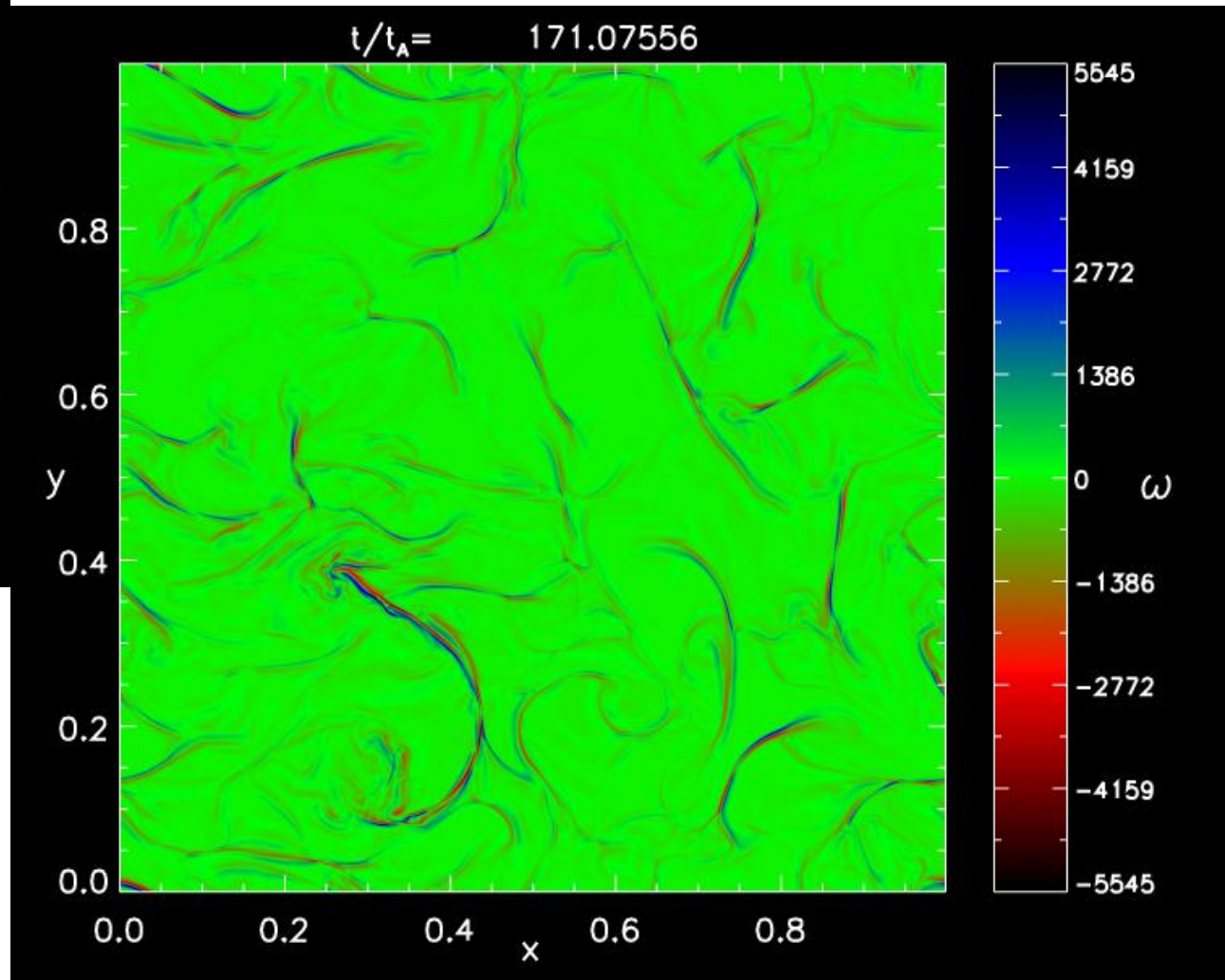
t/t_A= 171.07556
5545
4159
2772
1386
0
ω
−1386
−2772
−4159
−5545
0.0
0.2
0.4
0.6
0.8
y
x

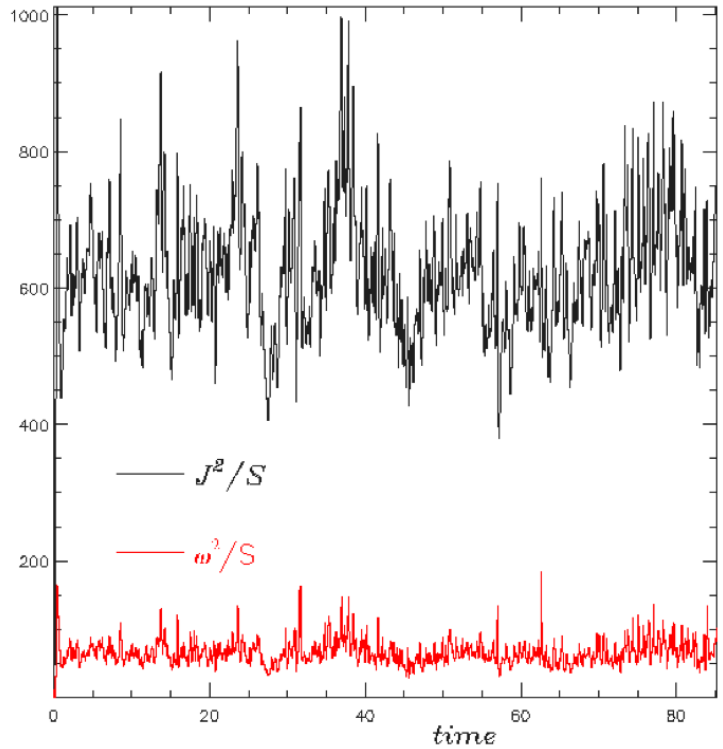

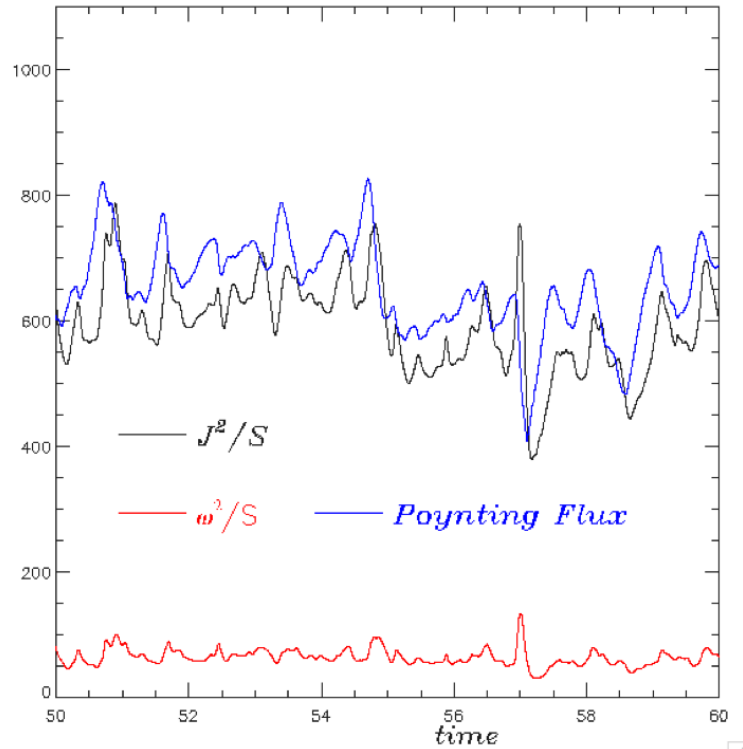

Chaotic time-series

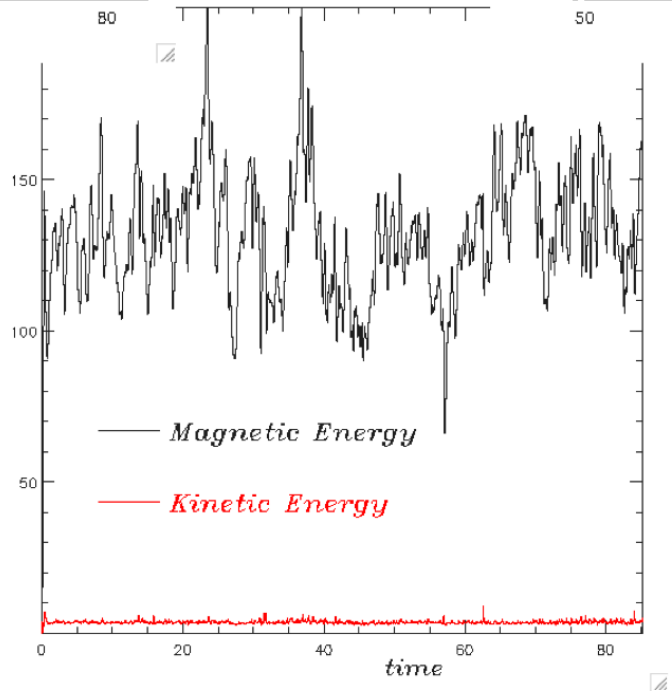

RMHD simulations

J^2/R

Red = 1000 Yellow = 350 Max = 2.7×10^4 min = 0

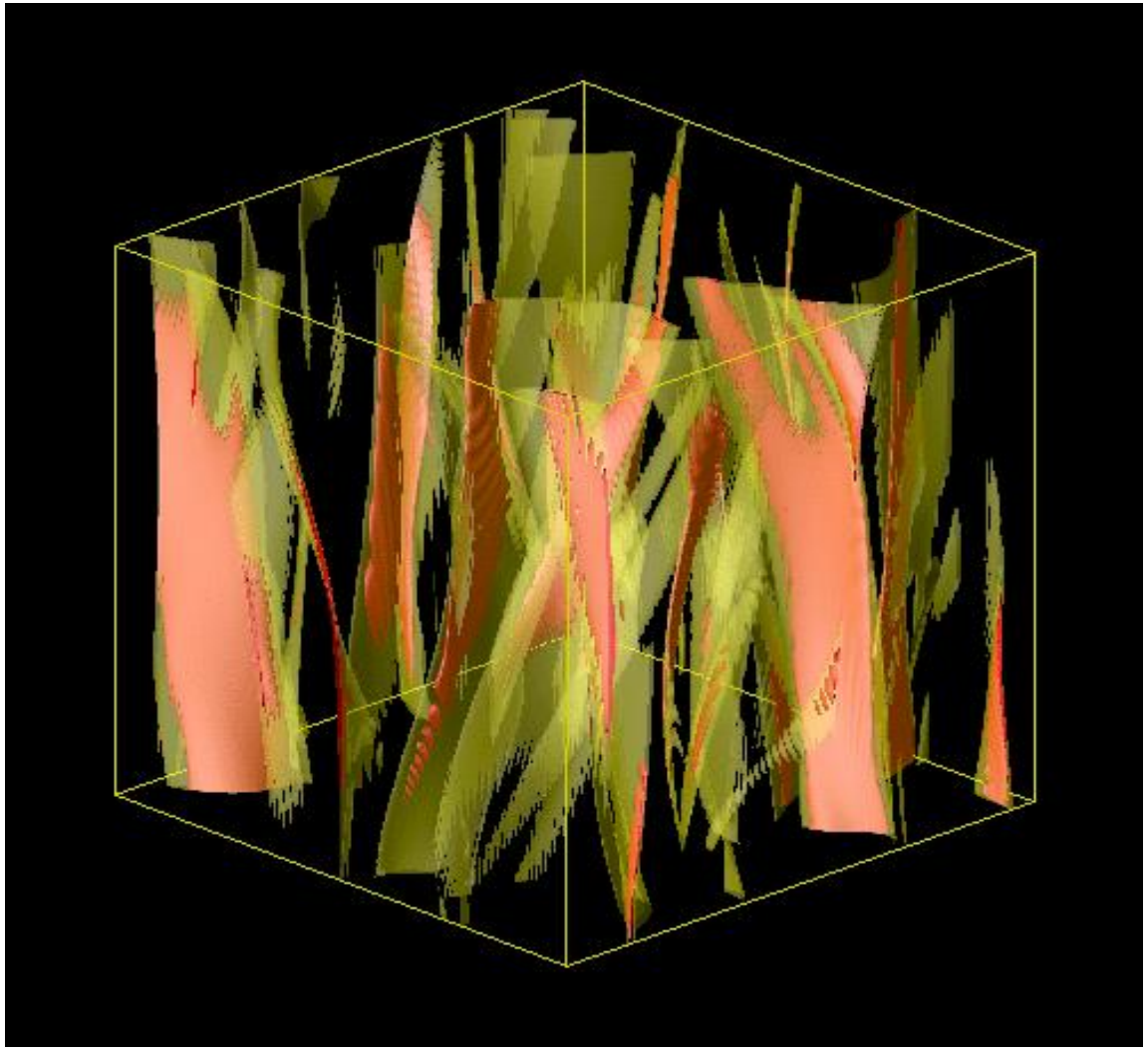

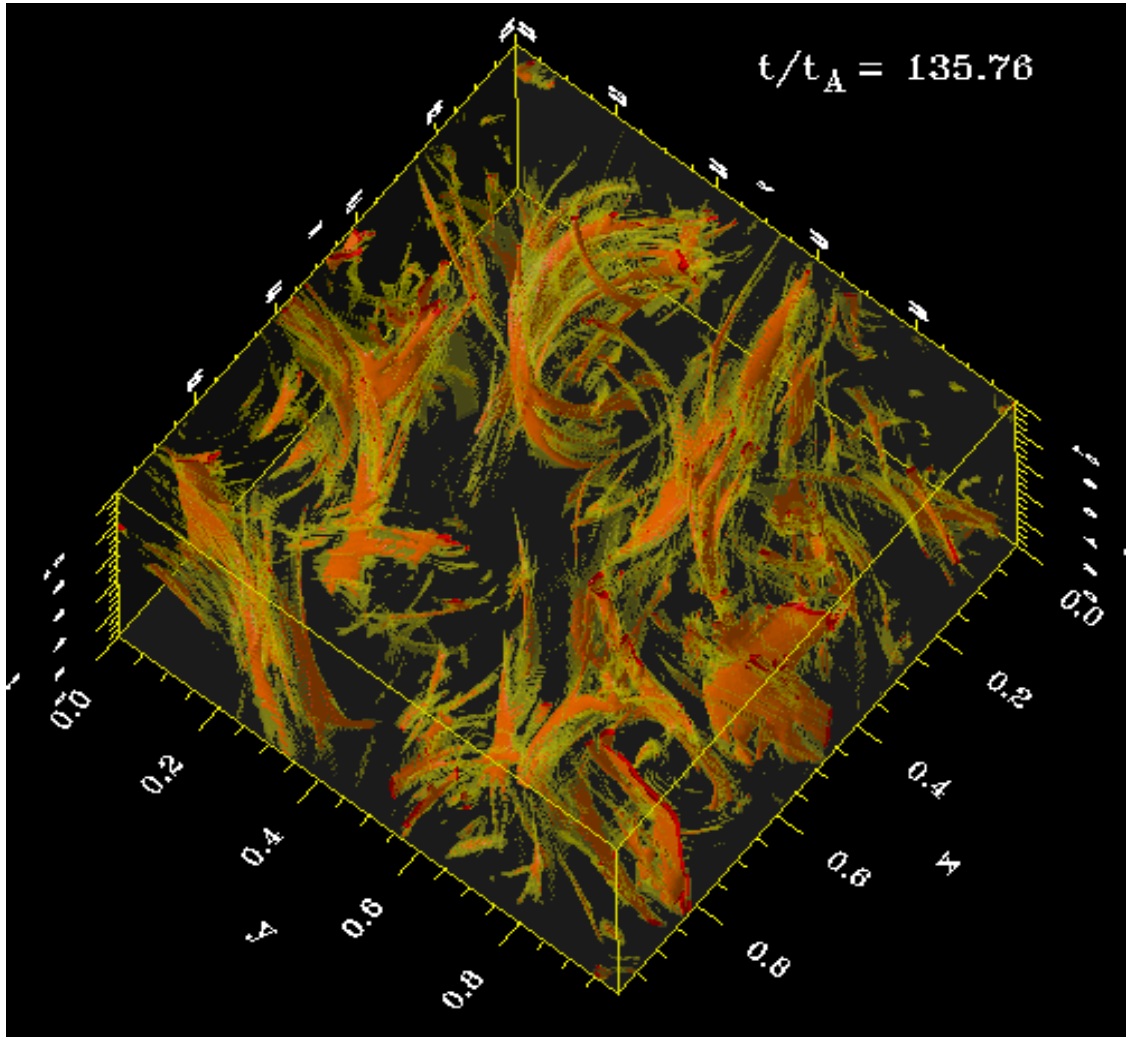

Component reconnection and wind source

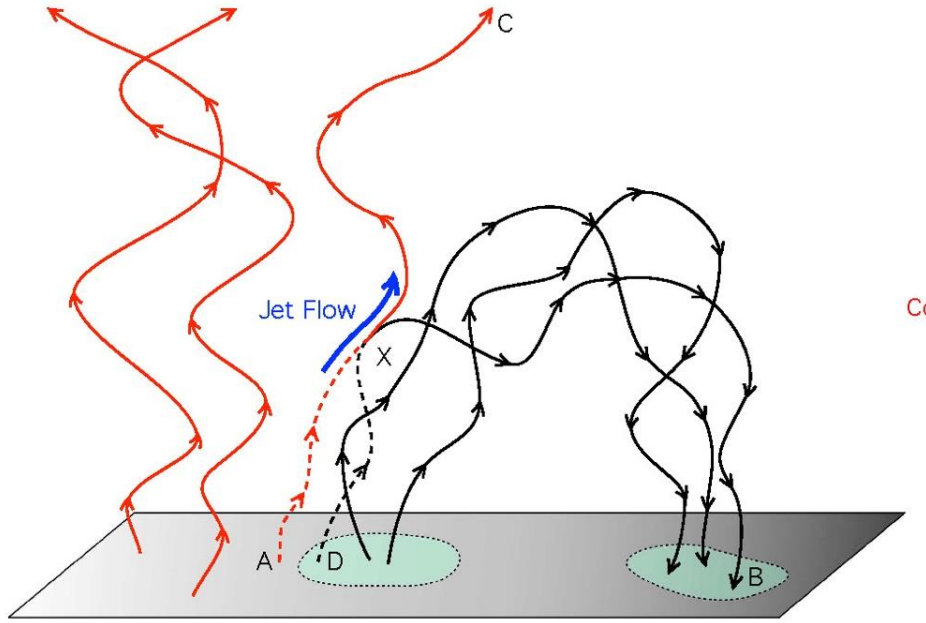

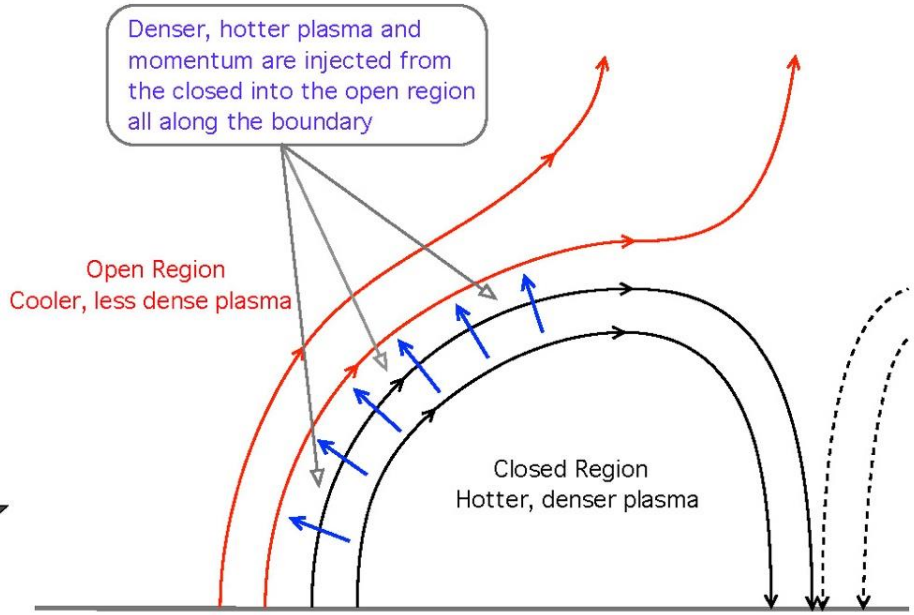

Component reconnection and wind source

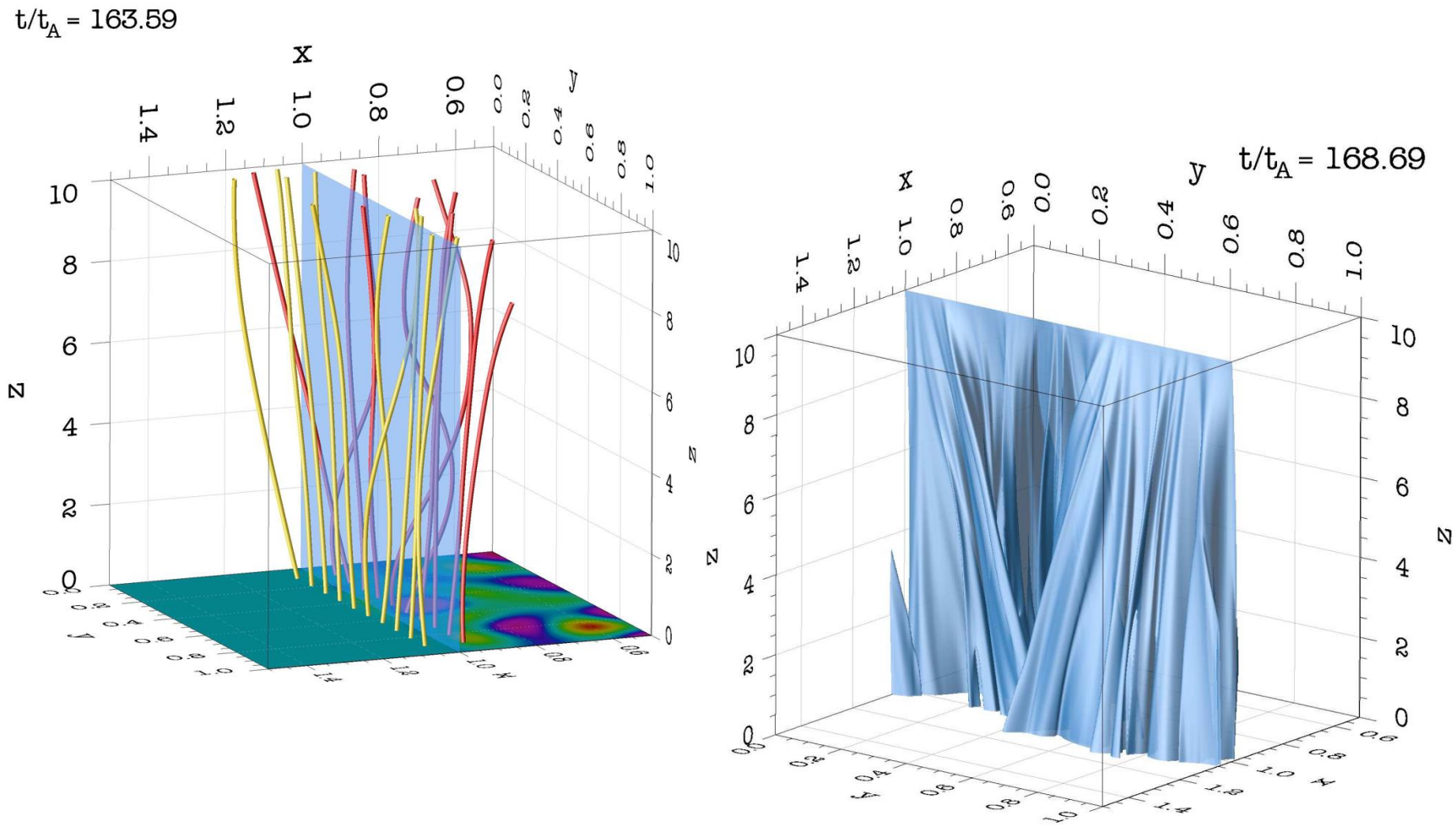

Sweet-Parker Current Sheets

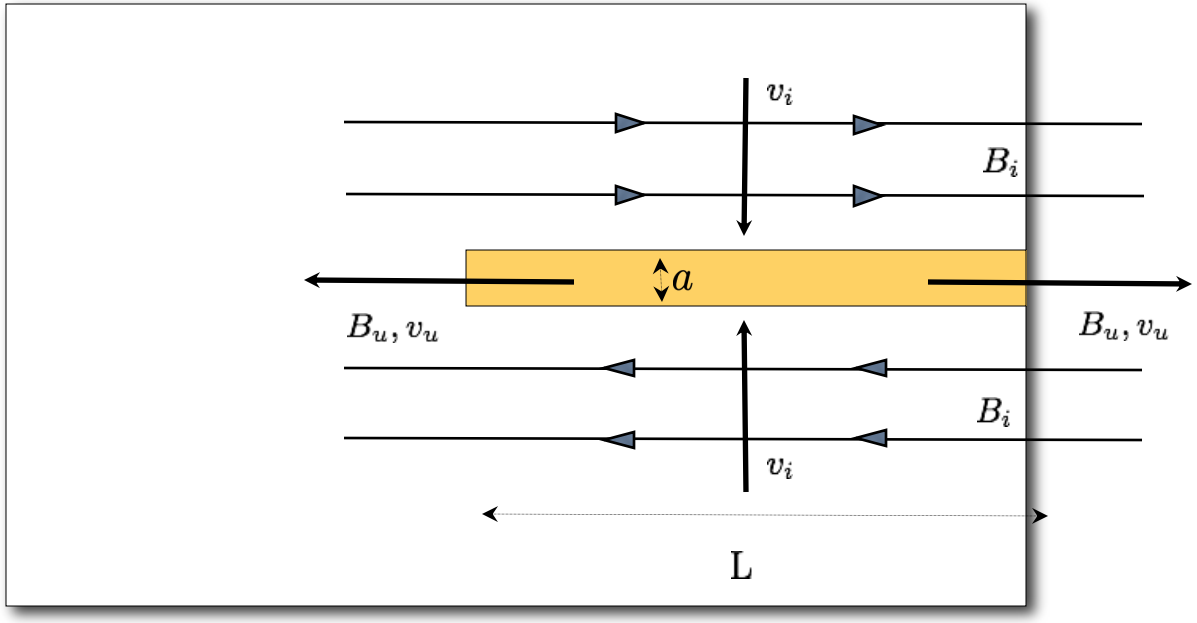

$$S = \frac{L v_A}{\eta}$$

$$\frac{a}{L} \sim S^{-1/2}$$

Energy dissipated in an Alfvén time in the sheet is proportional to:

$$L^2 v_i \tau_A = S^{-1/2} L^2 v_{Ai} \tau_A = L^3 S^{-1/2}$$

"The observational and theoretical difficulties with the hypothesis of magnetic-field line annihilation suggest that other alternatives for the flare must be explored." E. Parker, 1963

Tearing Mode Instability

$\Delta' > 0$ Instability $\gamma^2 = \frac{(k\,B_{0x})^2}{4\pi\rho_0}\frac{\delta}{a}\Delta'$ $\Delta' = 2\left(\frac{1}{ka} - ka\right)$ $ka < 1$

$$\gamma\,\tau_A \simeq 2.3\,(ka)^{-2/5}\,S^{-3/5}\left(1-k^2a^2\right)^{4/5} \qquad (kaS^{1/4} >> 1)$$

Numerical solution for the dispersion relation

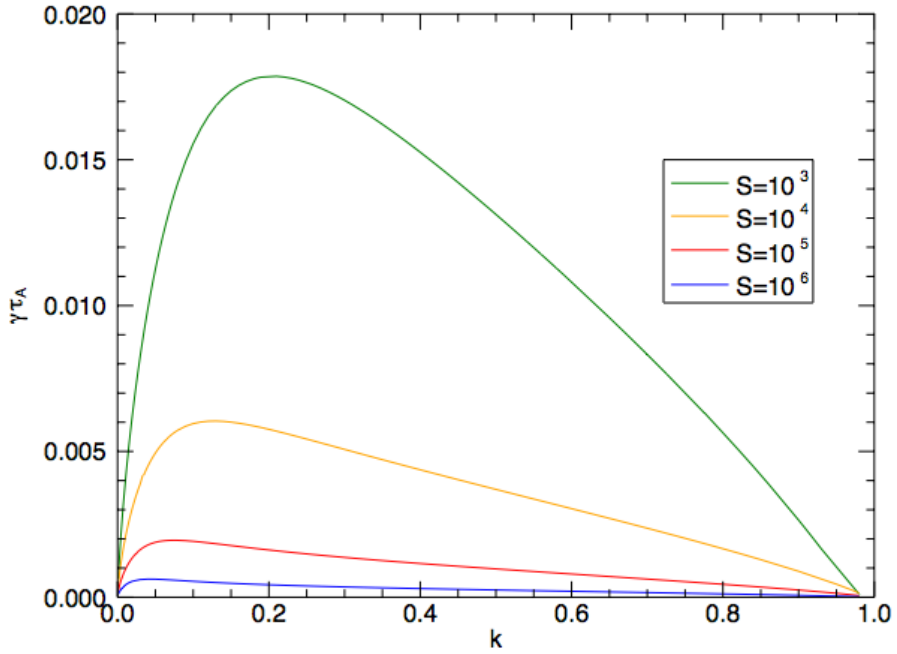

Eigenfunctions overlap out of the region where diffusivity is not negligible, for , $S = 10^6 \quad k = 0.01$

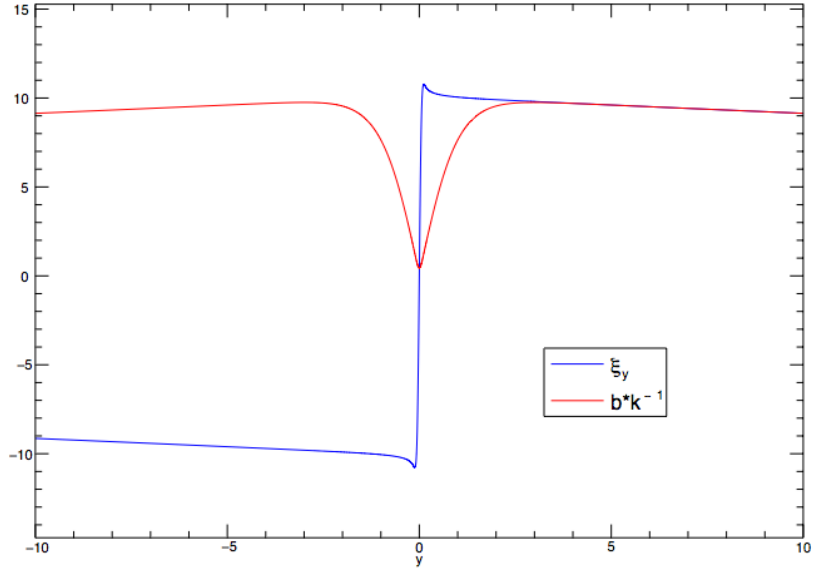

Tearing Mode Instability

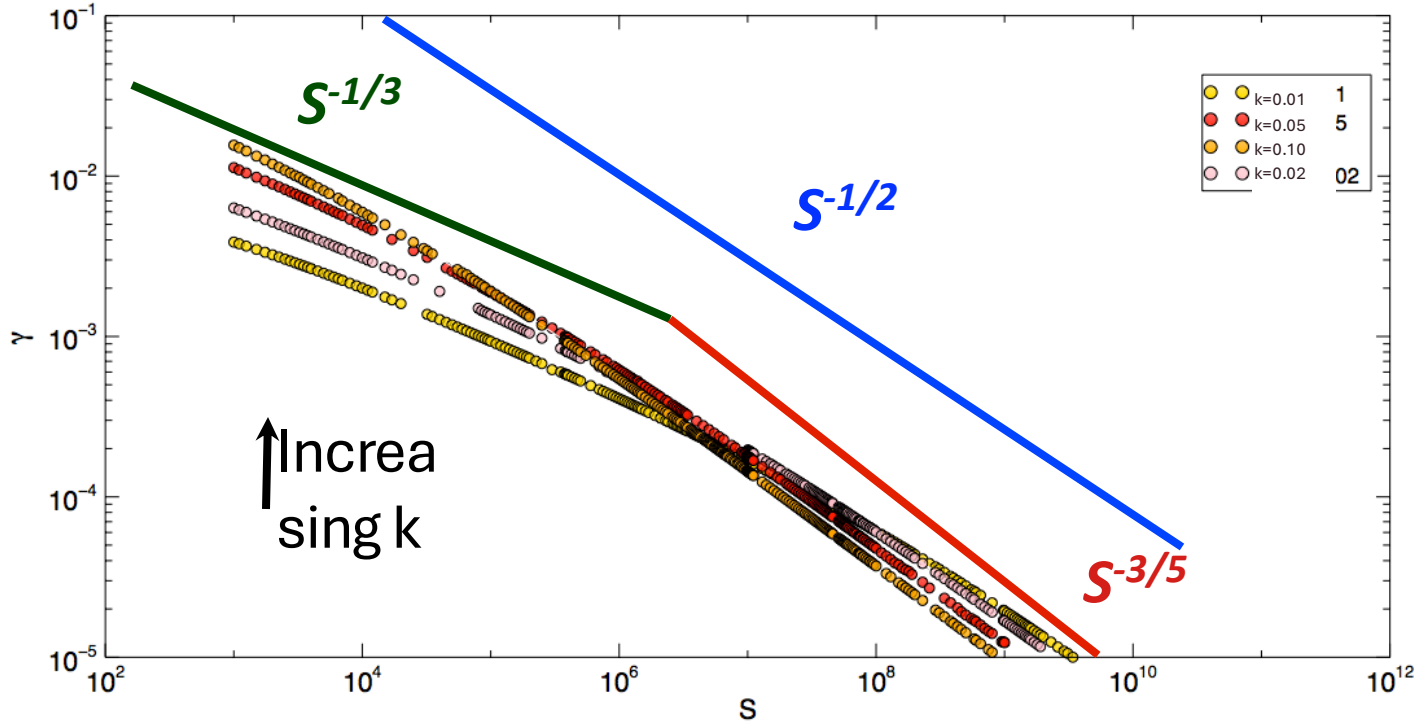

Three regimes:

$\gamma\tau_A \propto S^{-1/3}$

large Δ'

$\gamma_m\tau_A \propto S^{-1/2}$

Fastest Growing Mode

SLOW

$\gamma\tau_A \propto S^{-3/5}$

small Δ'

Plasmoid Instability of Sweet-Parker Current Sheet

Definition:

$$\tau_A = \frac{L}{v_A} \qquad S = \frac{Lv_A}{\eta} \qquad \tau_A^* = \frac{a}{v_A} \qquad S^* = \frac{av_A}{\eta}$$

Renormalizing: $(\tau = 1/\gamma)$

$$\tau = \tau_A^*(S^*)^{1/2} = \frac{L}{v_A}\left(\frac{Lv_A}{\eta}\right)^{1/2}\left(\frac{a}{L}\right)^{3/2} = \tau_A S^{1/2}\left(\frac{a}{L}\right)^{3/2} \qquad \gamma_{max}\frac{L}{V_a} \sim \left(\frac{a}{L}\right)^{-3/2} \times S^{-1/2}$$

For Sweet-Parker current sheet:

$$a/L \sim S^{-1/2}$$

$$\gamma\tau_a \sim S^{1/4} \qquad \tau \sim \tau_A S^{1/2} S^{-1/4} = \tau_A S^{-1/4}$$

PARADOX!

Threshold Lundquist Number for stable current sheets

- Early MHD simulations (Biskamp, 1986): S-P current sheets are **stable at $\boldsymbol{S} < \mathbf{10^4}$**
- The accelerating outflow stabilizes the current sheet (Bulanov et al., 1978)

- We carried out: linear MHD simulation & linear stabilitv analvsis for $S \leq 10^4$
- $\boldsymbol{u_0} = \Gamma x \hat{\boldsymbol{e}}_{\boldsymbol{x}} - \Gamma y \hat{\boldsymbol{e}}_{\boldsymbol{y}}$; $\boldsymbol{B_0} = B$
- $\frac{a}{L} = S^{-\frac{1}{2}}$
- $L_x \times L_y = 2L \times 2a$
- $n_x \times n_y = 256 \times 256$

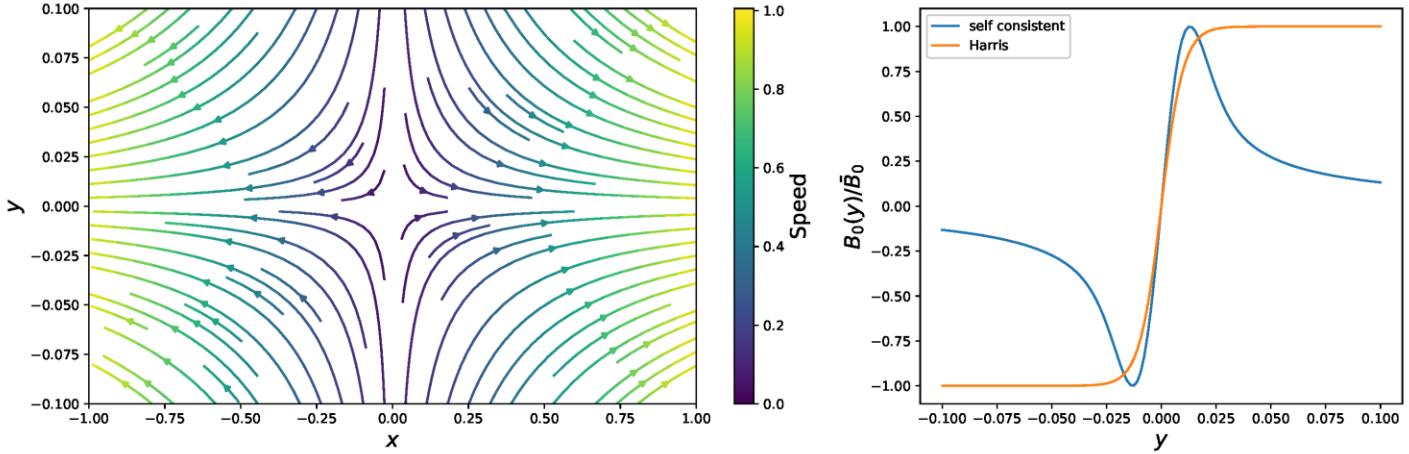

Background fields used in the simulation & stability analysis

- The inhomogeneous background outflow stabilizes the current sheet by
  1. stretching the growing magnetic islands:
     I. Decreases γ directly ($\gamma \sim \gamma_s - 1$)
     II. Decreases γ by increasing the wavelength
  2. Ejecting the magnetic islands within a finite time
- The critical Lundquist number should be several thousands (Shi et al., 2018)

Tearing Mode Instability

There exists a critical aspect ratio which scales with the non-ideal parameters of the system in question at which the reconnecting instability develops on a timescale that does not depend on the non-ideal terms themselves.

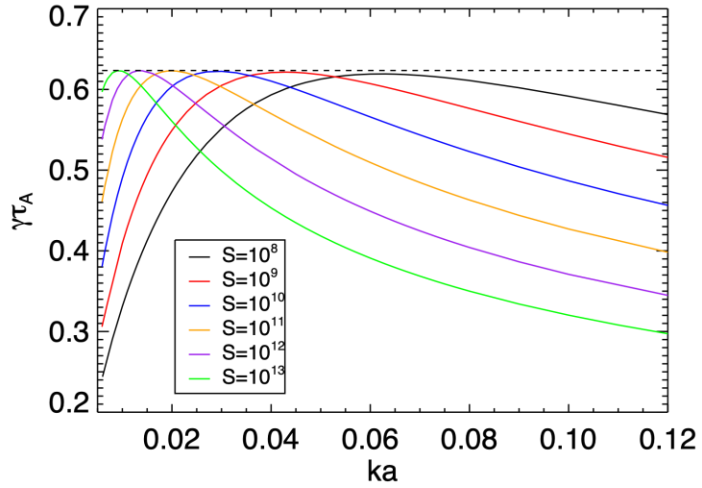

[Pucci and Velli 2014]

- Such critical aspect ratio $(L/a)_i$ provides a "sup" for current sheets that can naturally form
- Onset of "ideal" tearing can provide a scenario for the trigger of fast reconnection

$$a/L \sim S^{-1/3}$$

$$\delta/L \sim S^{-1/2}$$

Ah the viscosity

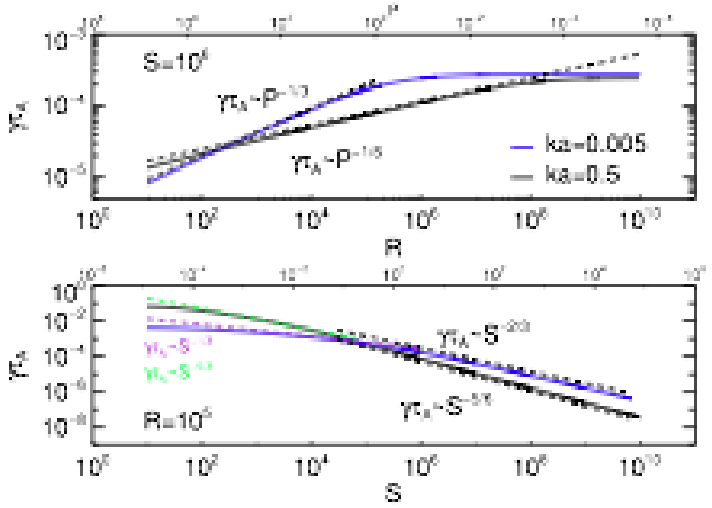

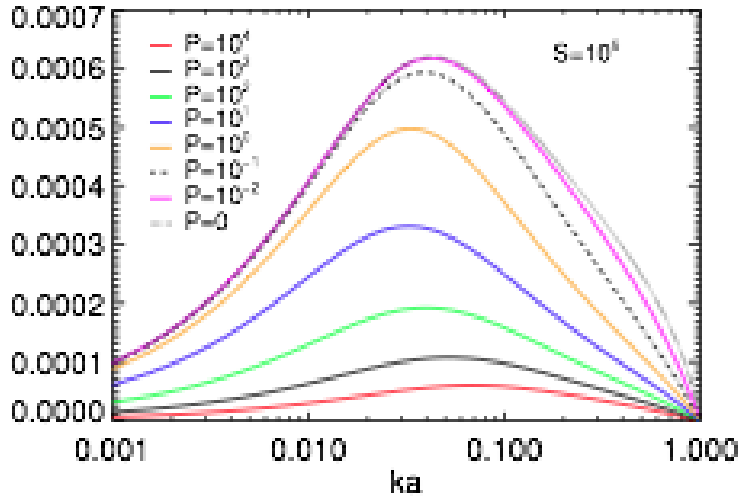

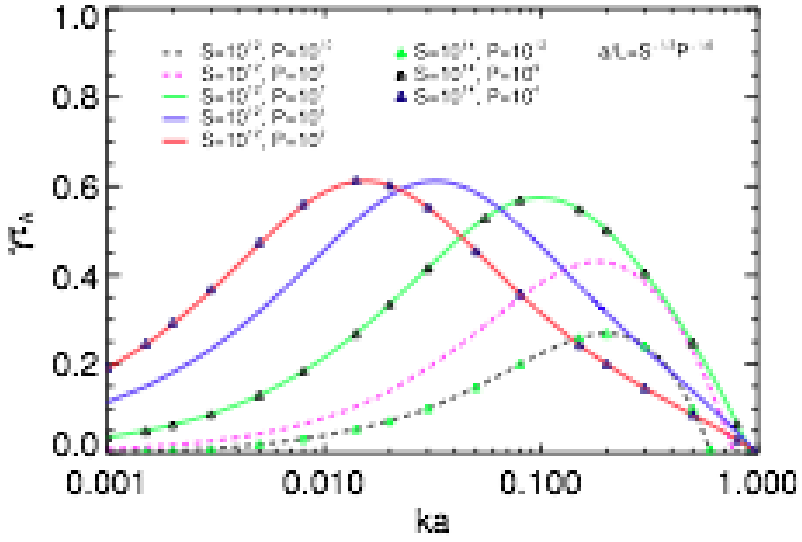

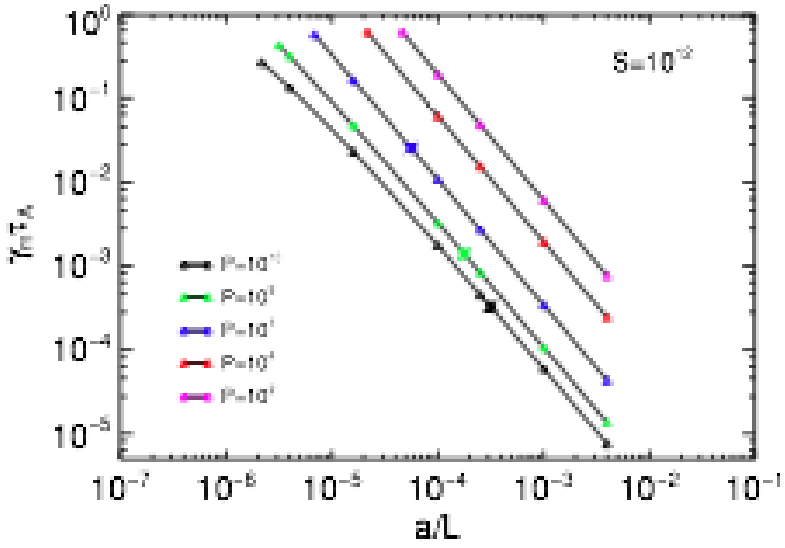

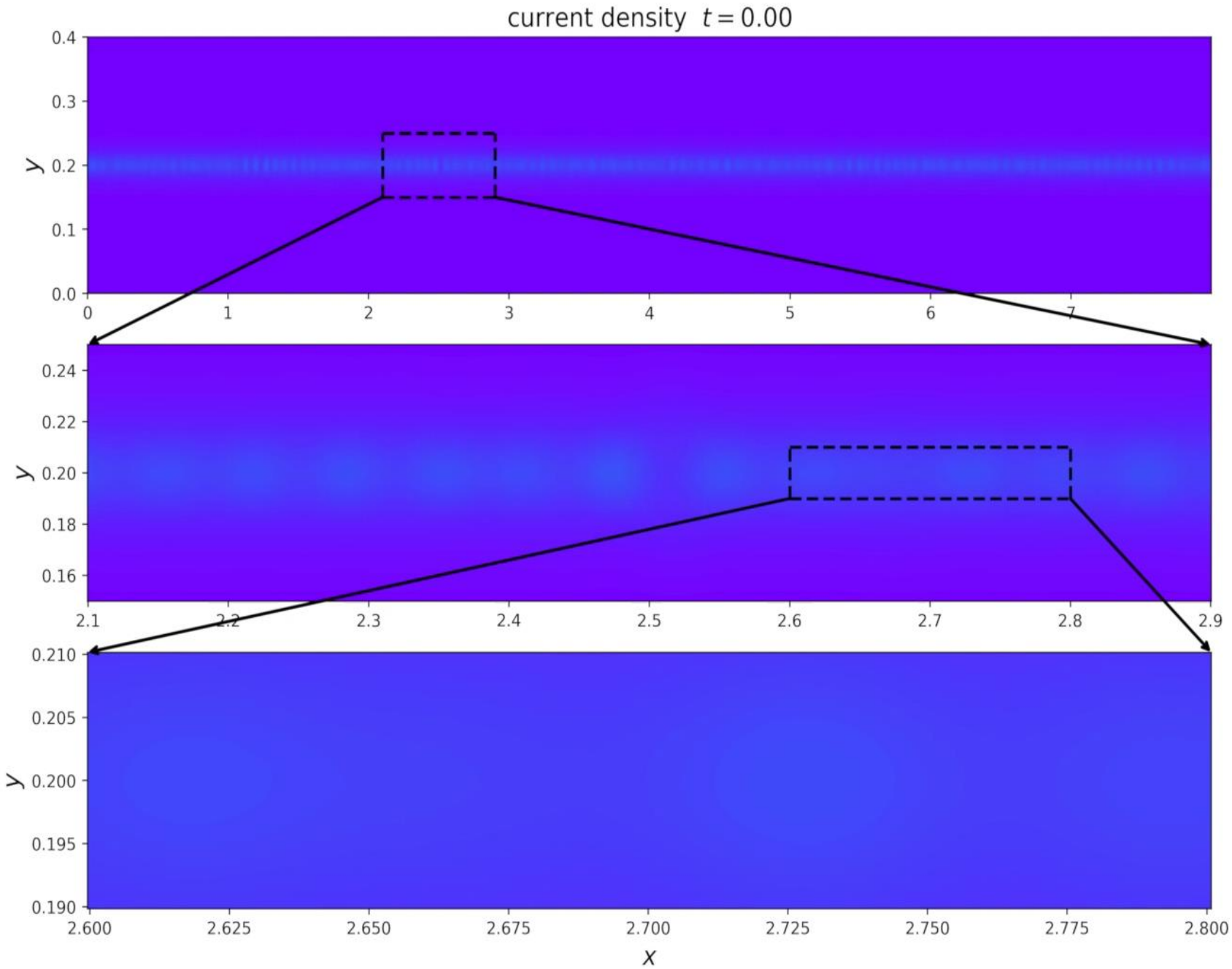
current density $t = 0.00$
y
x
0.4
0.3
0.2
0.1
0.0
0
1
2
3
4
5
6
7
0.24
0.22
0.20
0.18
0.16
2.1
2.2
2.3
2.4
2.5
2.6
2.7
2.8
2.9
0.210
0.205
0.200
0.195
0.190
2.600
2.625
2.650
2.675
2.700
2.725
2.750
2.775
2.800

Self similar current sheet collapse

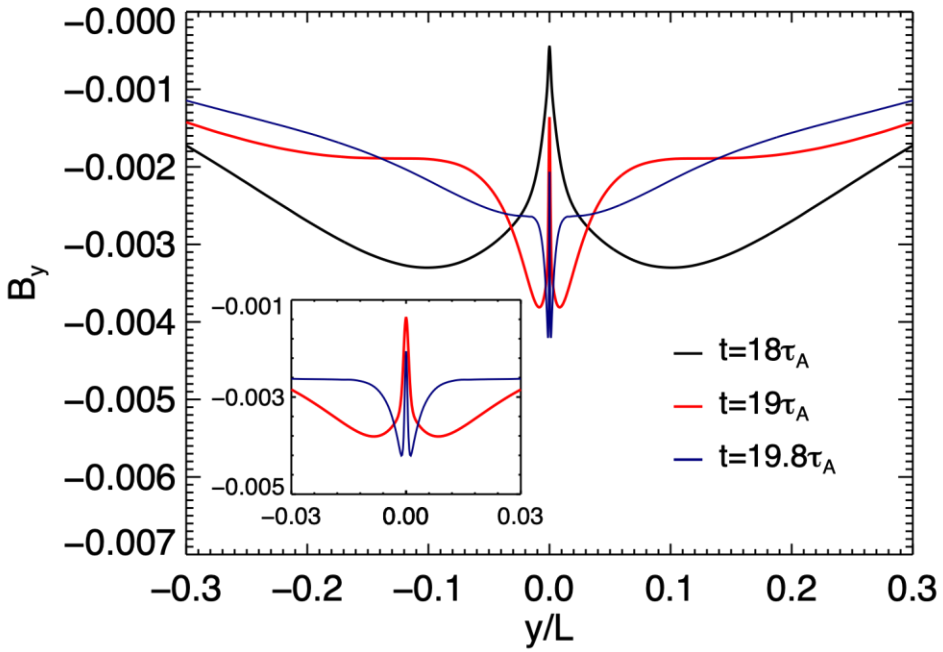

Evidence of "recursive" tearing mode-like instabilities during the nonlinear stage of a primary tearing mode within a Harris current sheet. New plasmoids appear to be generated, at each nth step, within smaller and smaller current sheets (CS), that consistently correspond to the inner layer of the (n-1)th unstable CS.

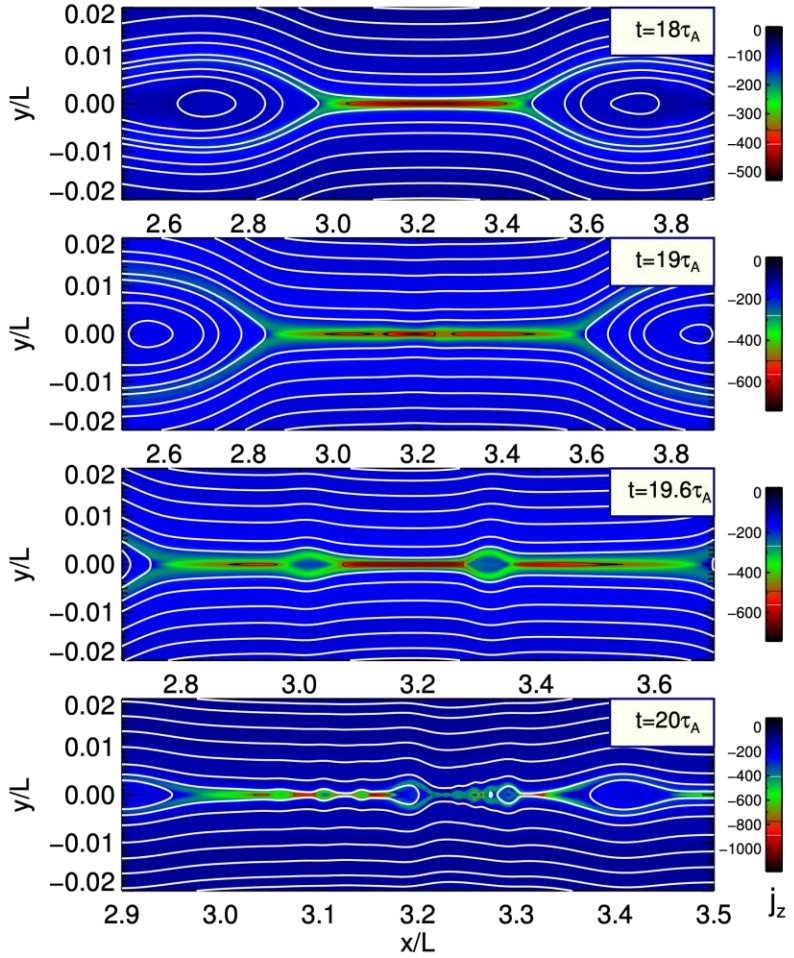

The fractal reconnection scenario

(1) Threshold for instability growth
(2) The nth unstable layer is the diffusion regions of layer (n-1)th

$$S = 10^{13} \rightarrow n_* = 4$$

$$a_n/L_n \sim S_n^{-1/3}$$

$$a_n/L_{n-1} \sim S_{n-1}^{-1/2}$$

$$S_n = S^{(3/4)^n}$$

$$L_n/L = S^{-1+(3/4)^n}$$

$$L_1/L \simeq 6.\,10^{-4}$$

$$L_2/L \simeq 2.\,10^{-6}$$

$$L_3/L \simeq 3.\,10^{-8}$$

$$L_4/L \simeq 10^{-9}$$

$$\tau_{tot} \simeq \Sigma_1^{n_*} \tau_{A,n} \simeq 10^{-4} \tau_A$$

$$n \rightarrow \infty,\ \tau_{A,n} = \tau_A S^{-1+(3/4)^n} \rightarrow \tau_A/S$$

$$S_n^* = 10^4$$

Tearing Mode in Hall MHD: faster

$$\gamma\tau_A \sim S^{-1/2}(a/L)^{-3/2}$$

$$kL \sim S^{-1/4}(a/L)^{-5/4}$$

$$\delta/L \sim S^{-1/4}(a/L)^{3/4}$$

$$\frac{a}{L} \sim S^{-1/3}$$

$$\frac{d_i}{L} \sim \frac{\delta}{L}$$

Plasma	$\mathcal{L}$	B	n	T	S	$\hat{\tilde{\delta}}$	h	a/L	ϵ_d
Solar Corona	10^9	100	10^9	10^6	2×10^{13}	2×10^{-7}	7×10^{-7}	10^{-4}	10^{-8}
Solar Cromosphere	5×10^8	$50-200$	10^{14}	10^4	3×10^8	6×10^{-5}	5×10^{-9}	$5-6\times10^{-6}$	10^{-10}
Solar Wind	10^{13}	3×10^{-5}	2	10^5	4×10^{13}	2×10^{-7}	2×10^{-6}	10^{-4}	4×10^8
Interstellar Gas	10^{15}	3×10^{-6}	1	10^4	2×10^{13}	2×10^{-7}	2×10^{-8}	TBD	5×10^{-10}
Magnetars Corona	3×10^6	10^{14}	10^{17}	10^7	3×10^{20}	6×10^{-11}	2×10^{-8}	TBD	6×10^{-10}
Magnetotail	$\times10^9$	10^{-4}	10^{-1}	10^7	4×10^{13}	6×10^6	7×10^{-2}	7×10^{-2}	3×10^{-6}

For magnetotail reconnection parameters, typical conditions in the plasma sheet during a substorm growth phase have been considered, [Eastwood et al., 2009][Coroniti, 1985][Angelopoulos et al., 2013] [Eastwood et al., 2009] [Sergeev et al., 1993] [Kivelson and Russell, 1995]

.

Tearing Mode in Hall MHD: faster

$$a/L \sim \bar{S}^{-\alpha} \bar{P}_h^{-\beta}$$

$$\alpha = -1/3 \qquad \beta = 0.29$$

$$\bar{P}_h = \frac{d_i}{L} \bar{S}^{1/2}$$

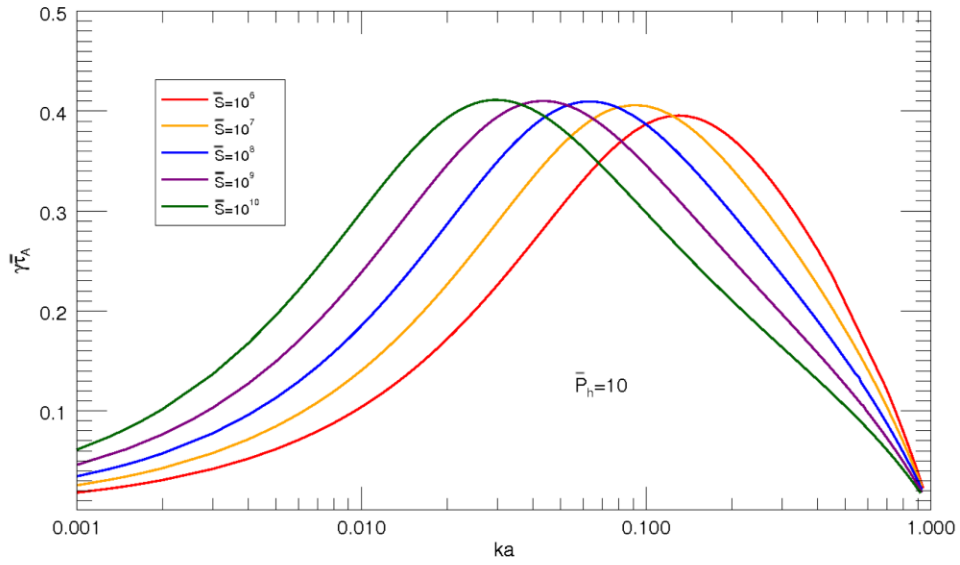

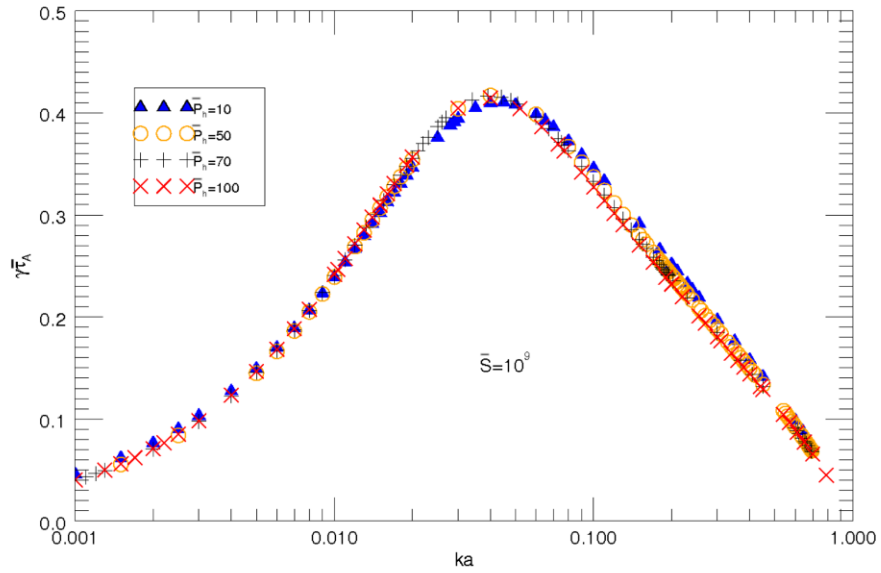

Pucci et al 2016

What if when the current sheet approaches ion kinetic scale? HALL

$d_i = 0$

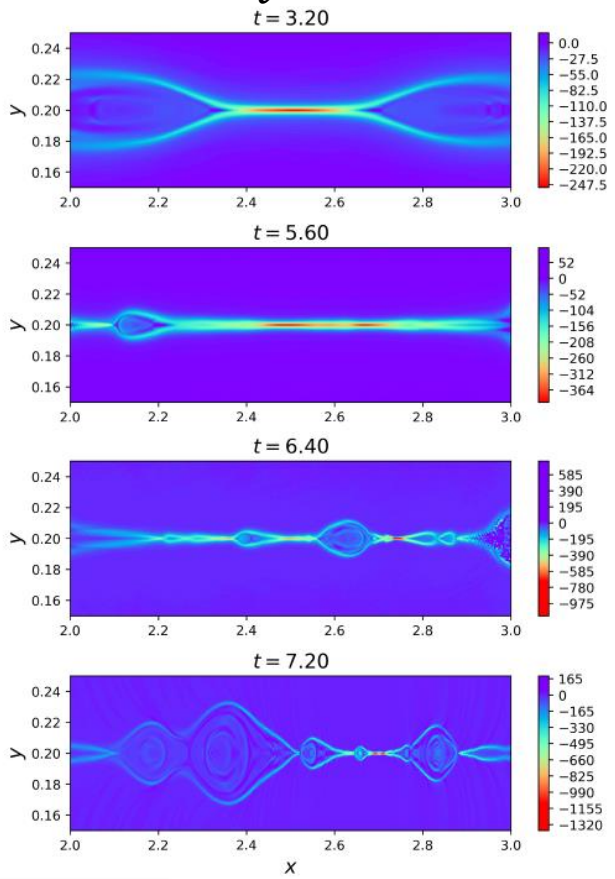

$d_i = 1 \times 10^{-3}$

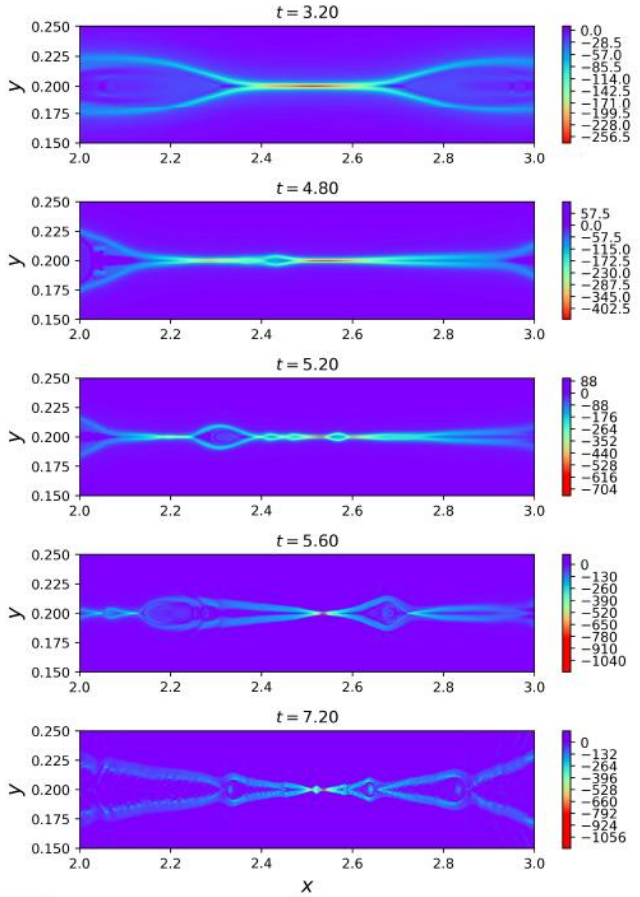

$d_i = 2 \times 10^{-3}$

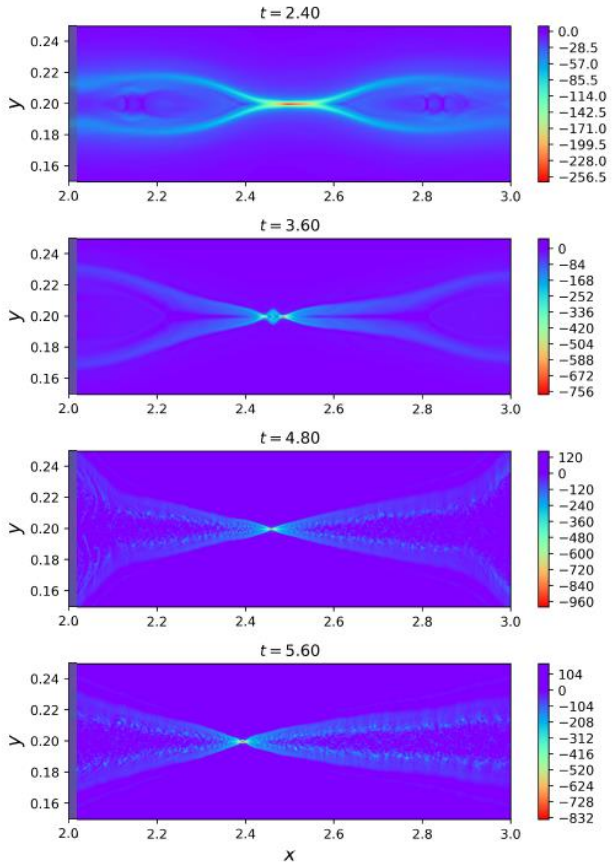

Shi+2019

Recursive plasmoids generation

Single “X”-point

Ohm's law: inertial reconnection in RMH, EMHD

$$E_i + \frac{1}{c}(\vec{U} \times \vec{B})_i - \cancel{\frac{J_i}{\sigma}} = \frac{m_e}{e^2 n_e}\left[\frac{\partial J_i}{\partial t} + \frac{\partial}{\partial x_k}(J_i U_k + J_k U_i)\right] + \frac{1}{e n_e c}\left(\vec{J} \times \vec{B}\right)_i - \frac{1}{e n_e}\frac{\partial P_{ik}^{(e)}}{\partial x_k}$$

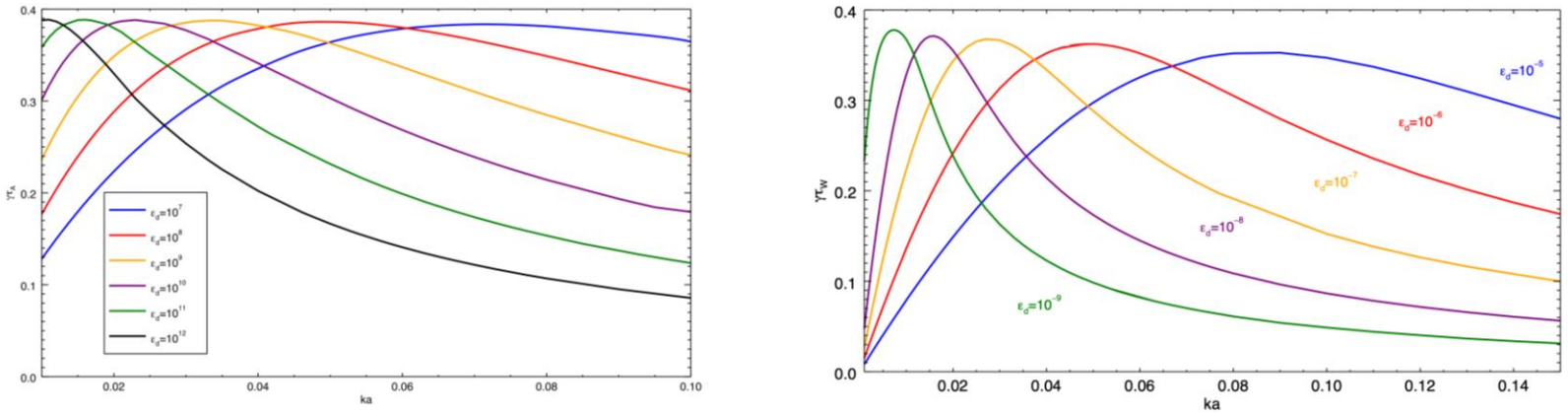

Dispersion relation at the critical width

$$\frac{a_i}{L} = \left(\frac{d_e}{L}\right)^{2/3} \qquad \frac{a_i}{L} = \left(\frac{d_e}{L}\right)^{5/14}$$

Del Sarto et al., 2016, JGR

Perihelion #	Date of Perihelion	Perihelion (Rs)	Time within			
			30 Rs	20 Rs	15 Rs	10 Rs
1	11/1/18	35.66				
2	3/31/19	35.66				
3	8/28/19	35.66				
4	1/24/20	27.85	61.04			
5	6/2/20	27.85	61.06			
6	9/22/20	20.35	104.22			
7	1/13/21	20.35	104.22			
8	4/24/21	15.98	108.55	48.06		
9	8/5/21	15.98	108.55	48.06		
10	11/16/21	13.28	107.27	55.13	24.75	
11	2/21/22	13.28	107.27	55.13	24.75	
12	5/28/22	13.28	107.27	55.12	24.75	

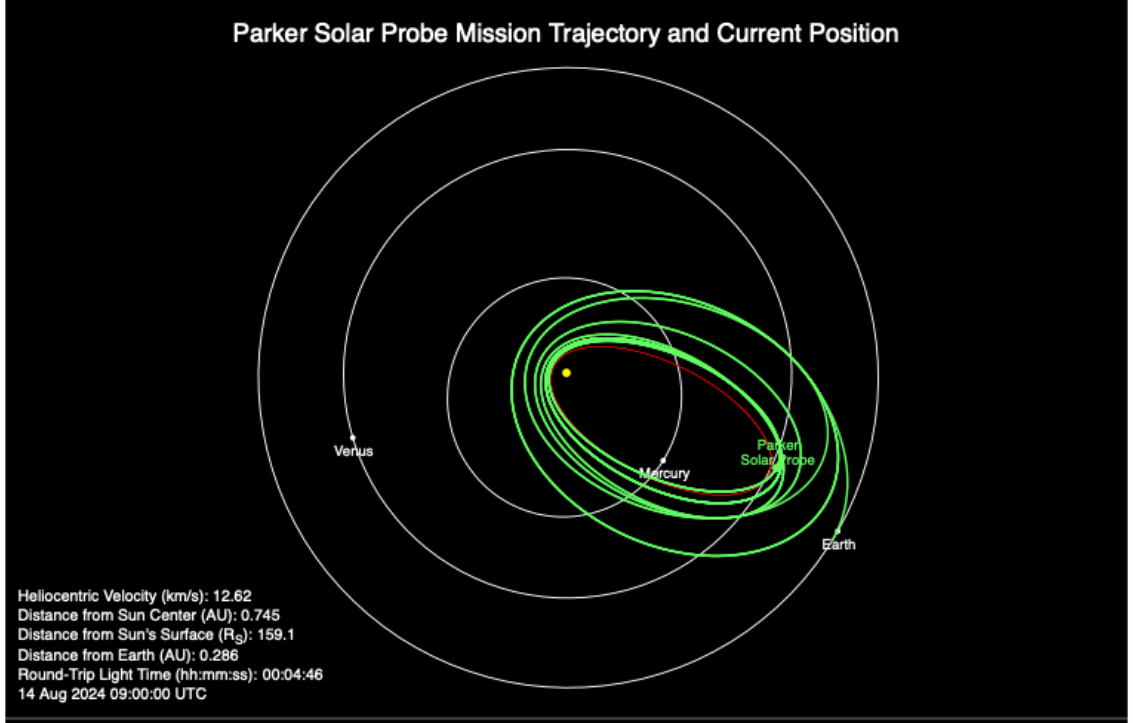

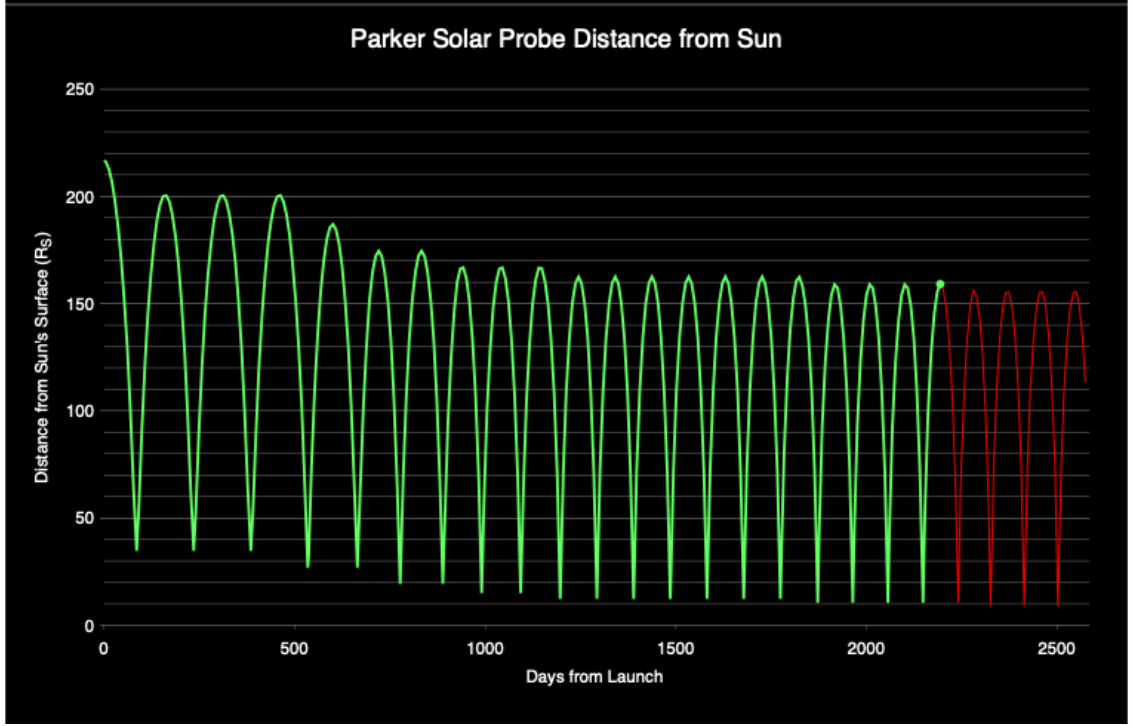

Probe-1st perihelion Magnetic Field

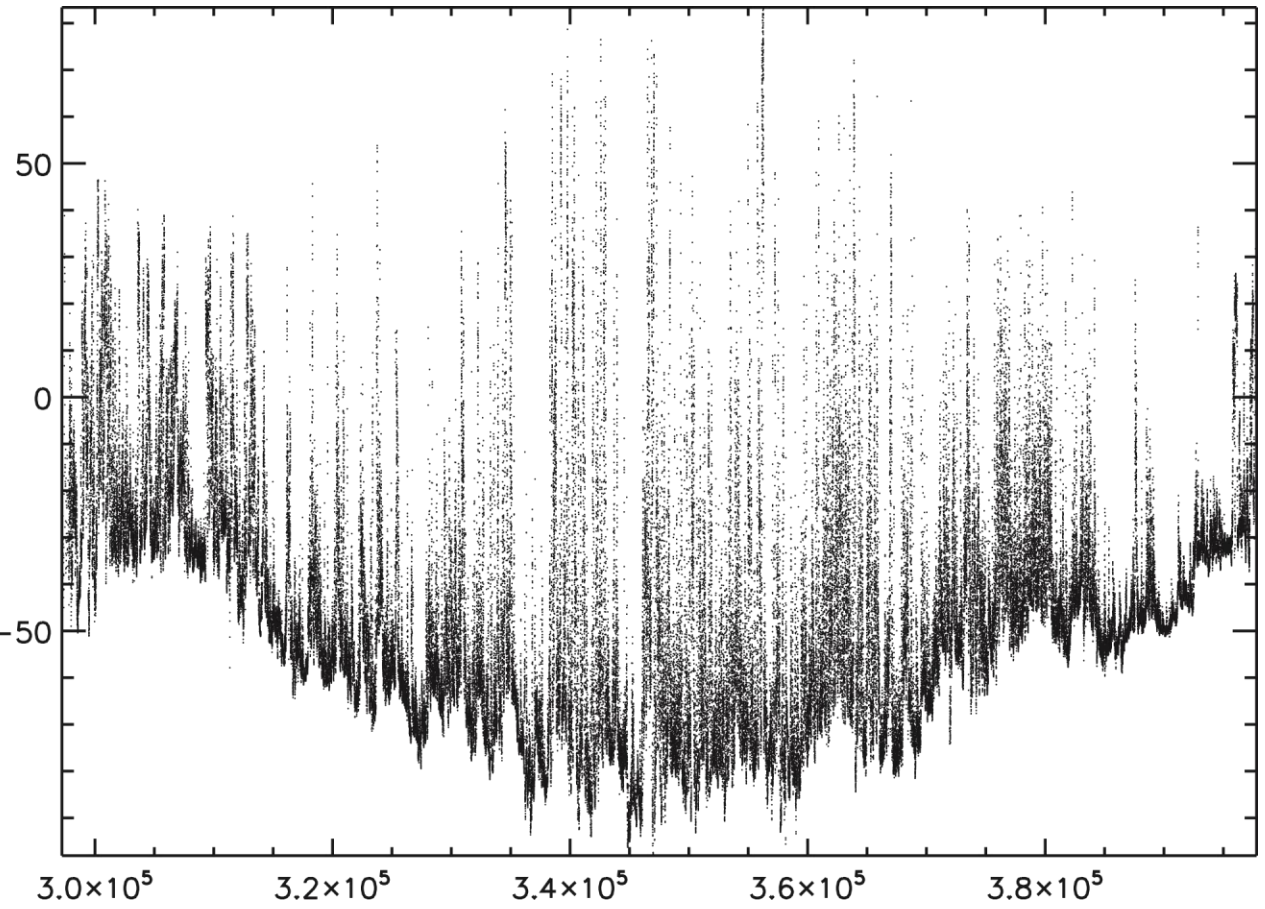

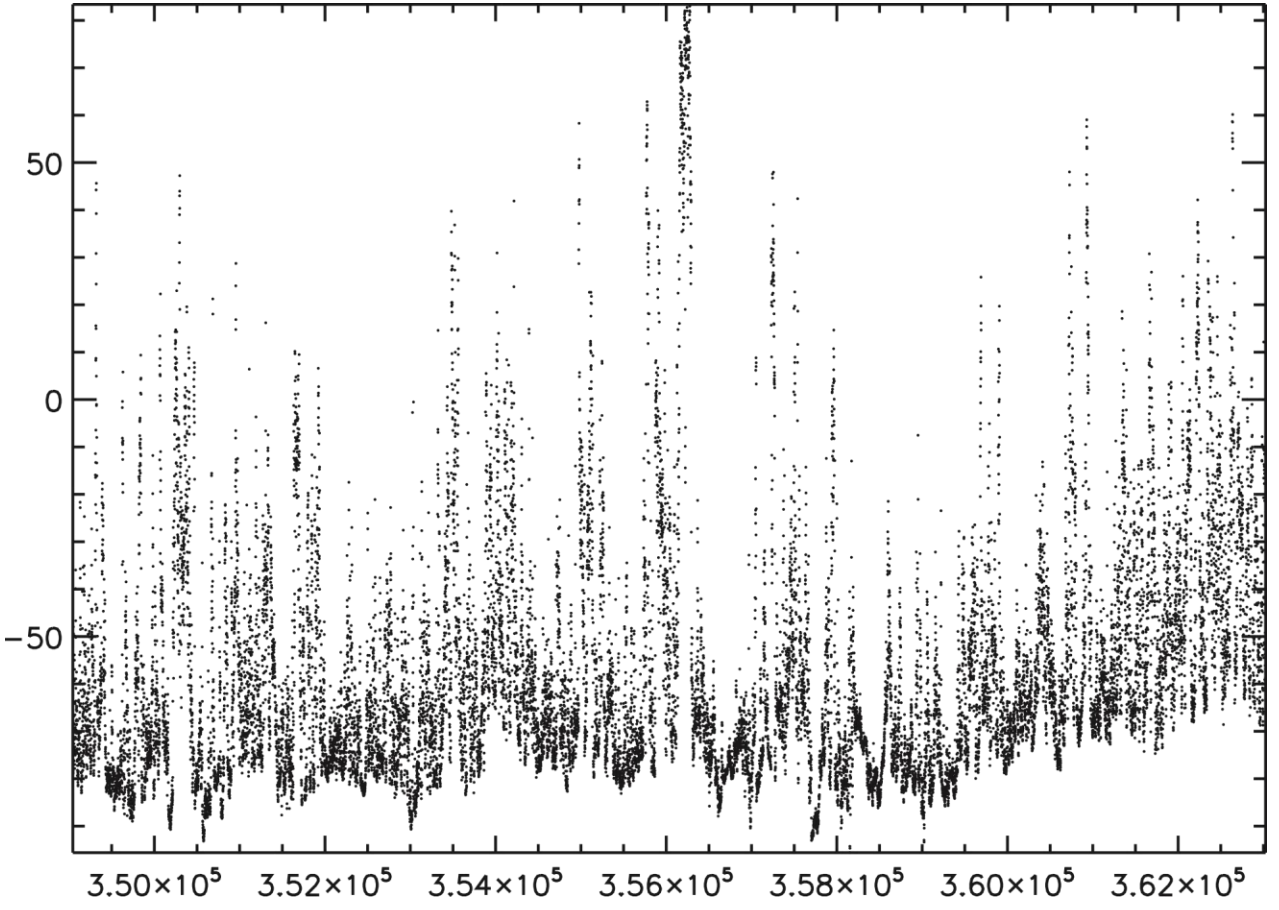

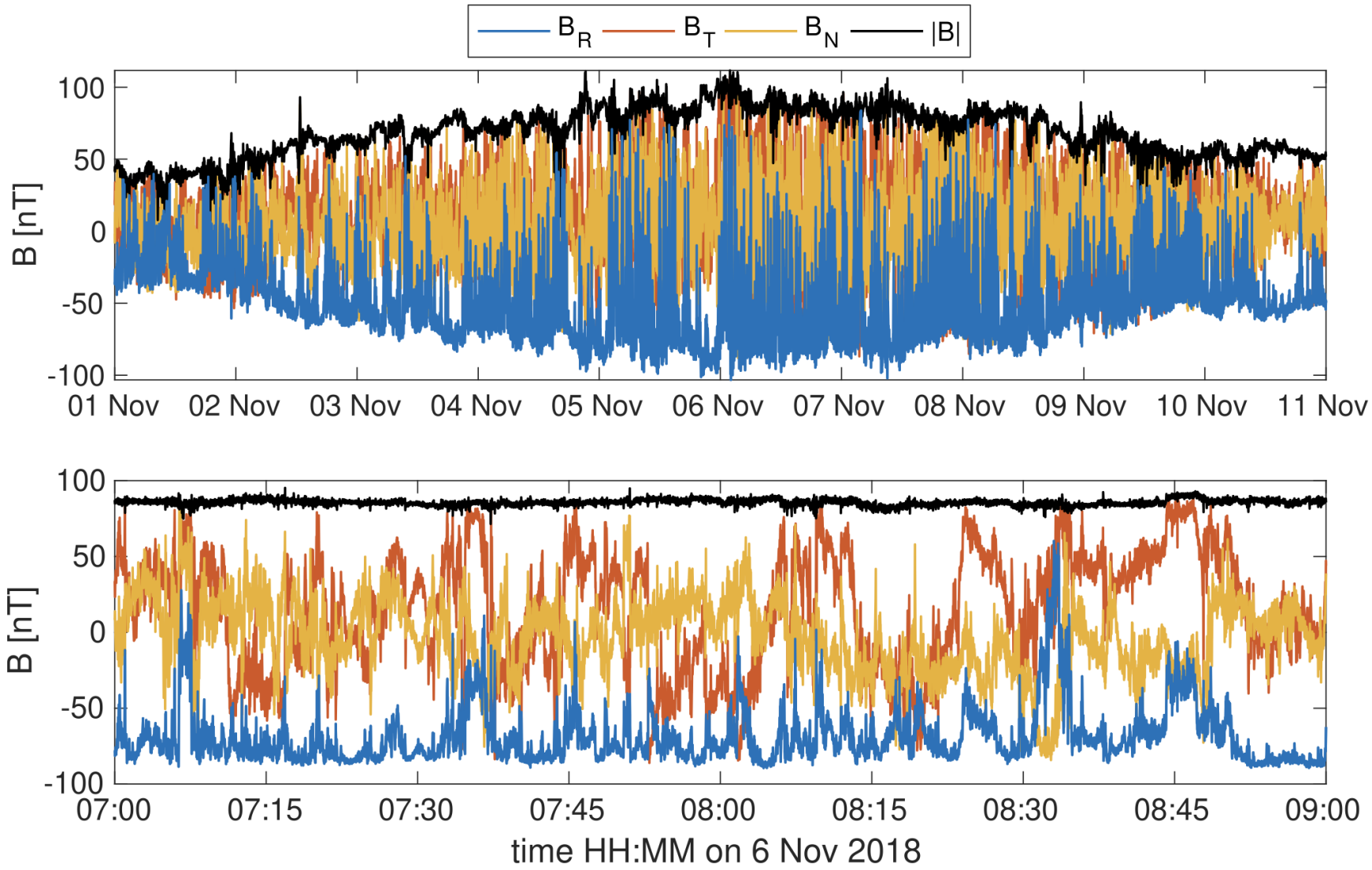

Highly Alfvenic magnetic field ‘switchbacks’ are ubiquitous in the inner heliosphere and are organized into ‘patches’ separated by quieter wind (Bale et al., 2019, Dudok de Wit et al., 2020, Horbury et al., 2020, Mozer et al., 2020, Squire et al., 2020 and many more)

Small, equatorial coronal holes can be a source of solar wind that expands laterally, slowing down, and filling the inner heliosphere (Bale et al., 2019, Nature Panasenco et al. 2019, 2020 ApJS)

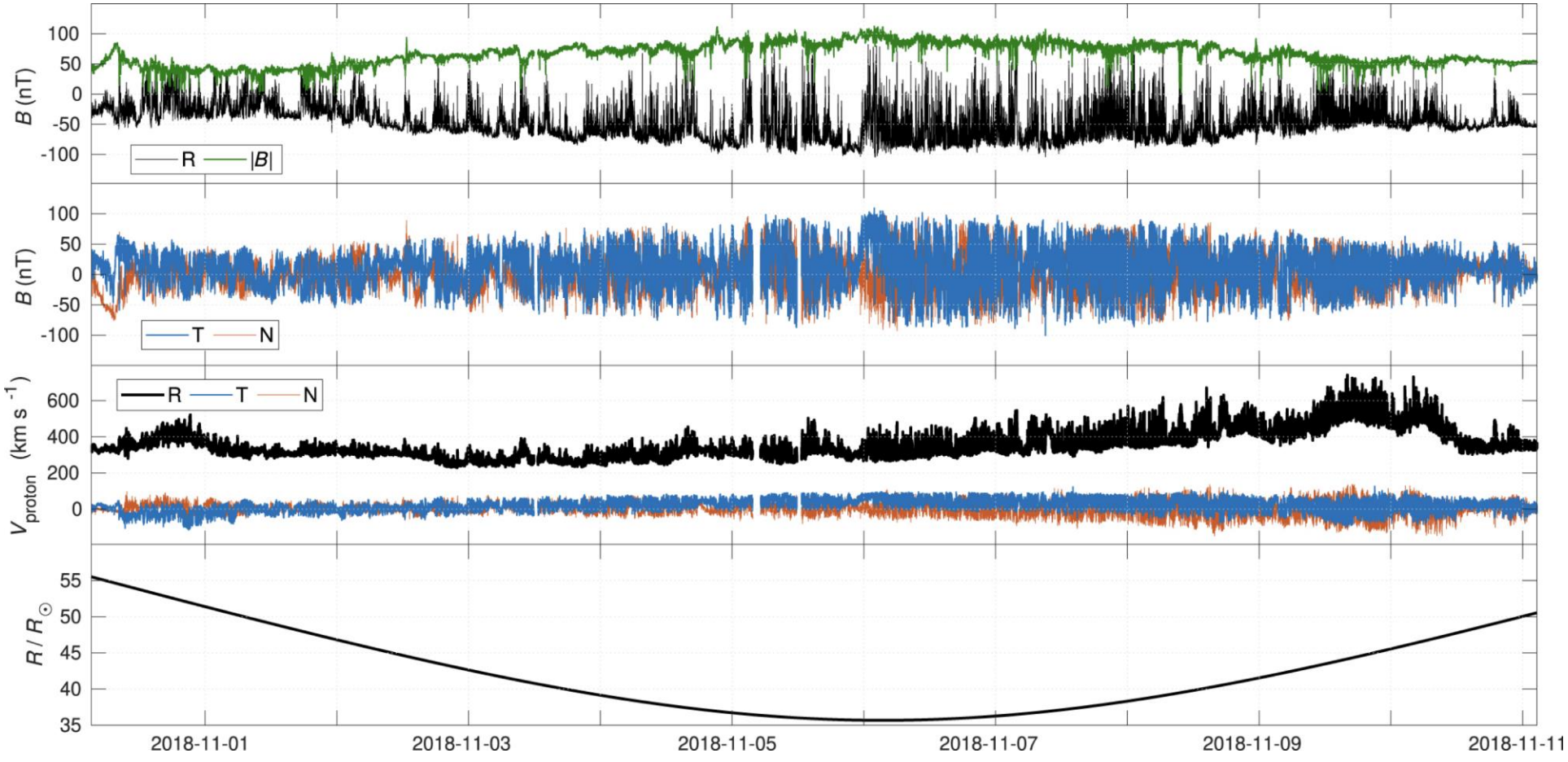

Alfvénic velocity spikes
Kasper et al., 2019, Nature, Volume 576, Issue 7786, p.228-231
Discovery of coherent structures travelling through the solar wind at high speeds called switchbacks.

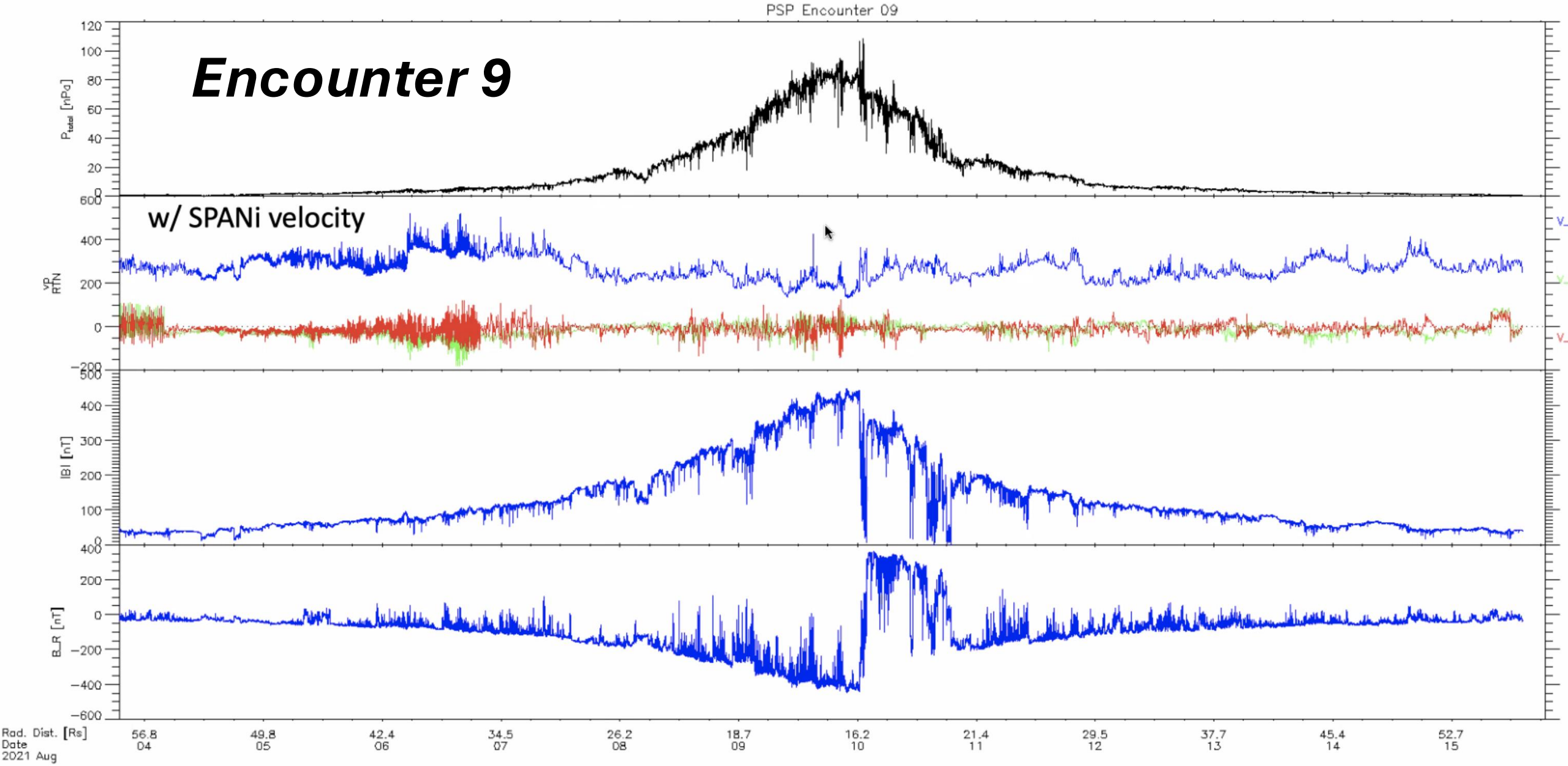
PSP Encounter 09
Encounter 9
w/ SPANi velocity
P_total [nPa]
vp RTN
IBI [nT]
BLR [nT]
Rad. Dist. [Rs]
Date
2021 Aug
56.8 04
49.8 05
42.4 06
34.5 07
26.2 08
18.7 09
16.2 10
21.4 11
29.5 12
37.7 13
45.4 14
52.7 15

Encounter 12

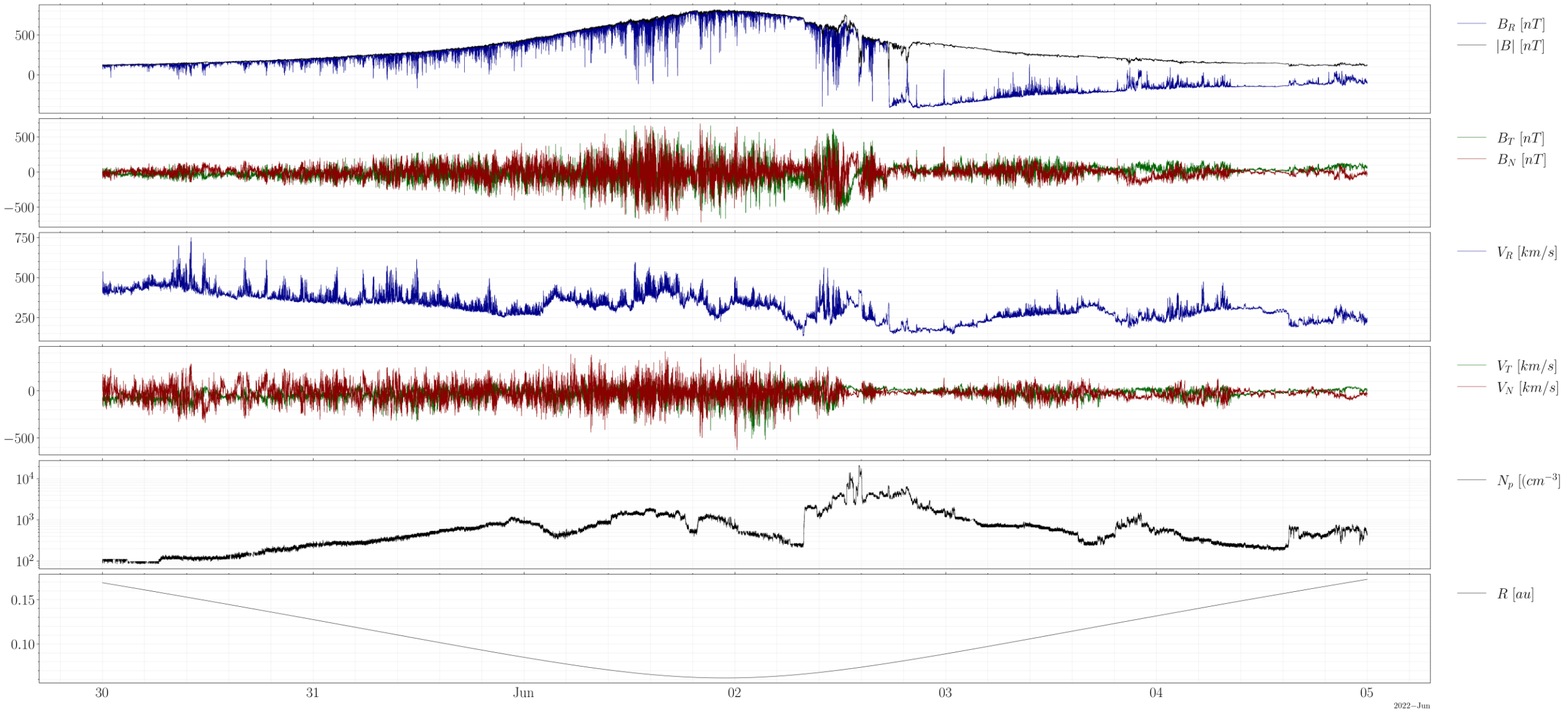

Switchbacks are Alfvénic

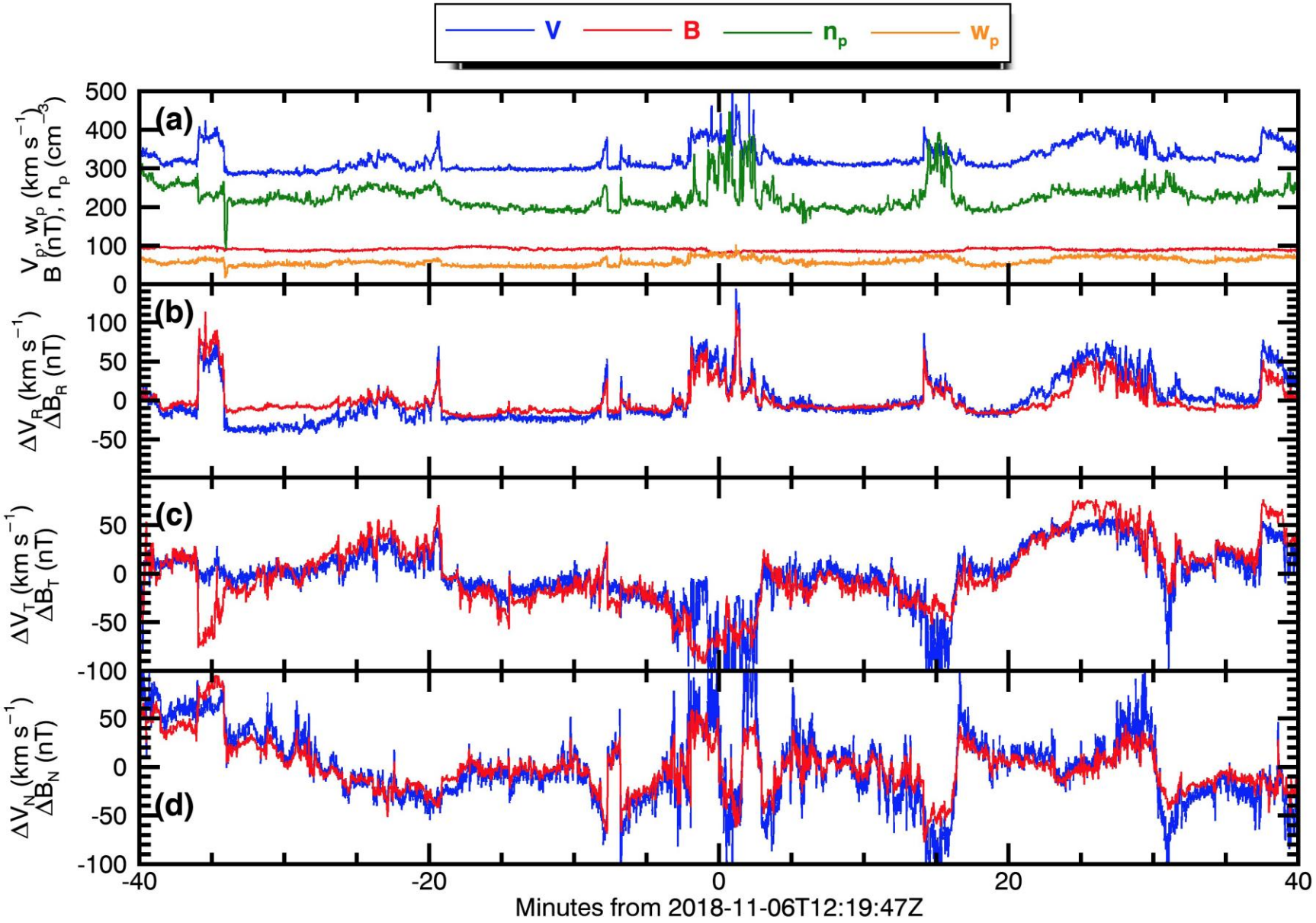

Switchback Jets

Outward AW

$\delta u = -\delta b$

$\delta b_R < 0 \quad \delta v_R > 0$

Outward AW

$\delta u = \delta b$

$\delta b_R > 0 \quad \delta v_R > 0$

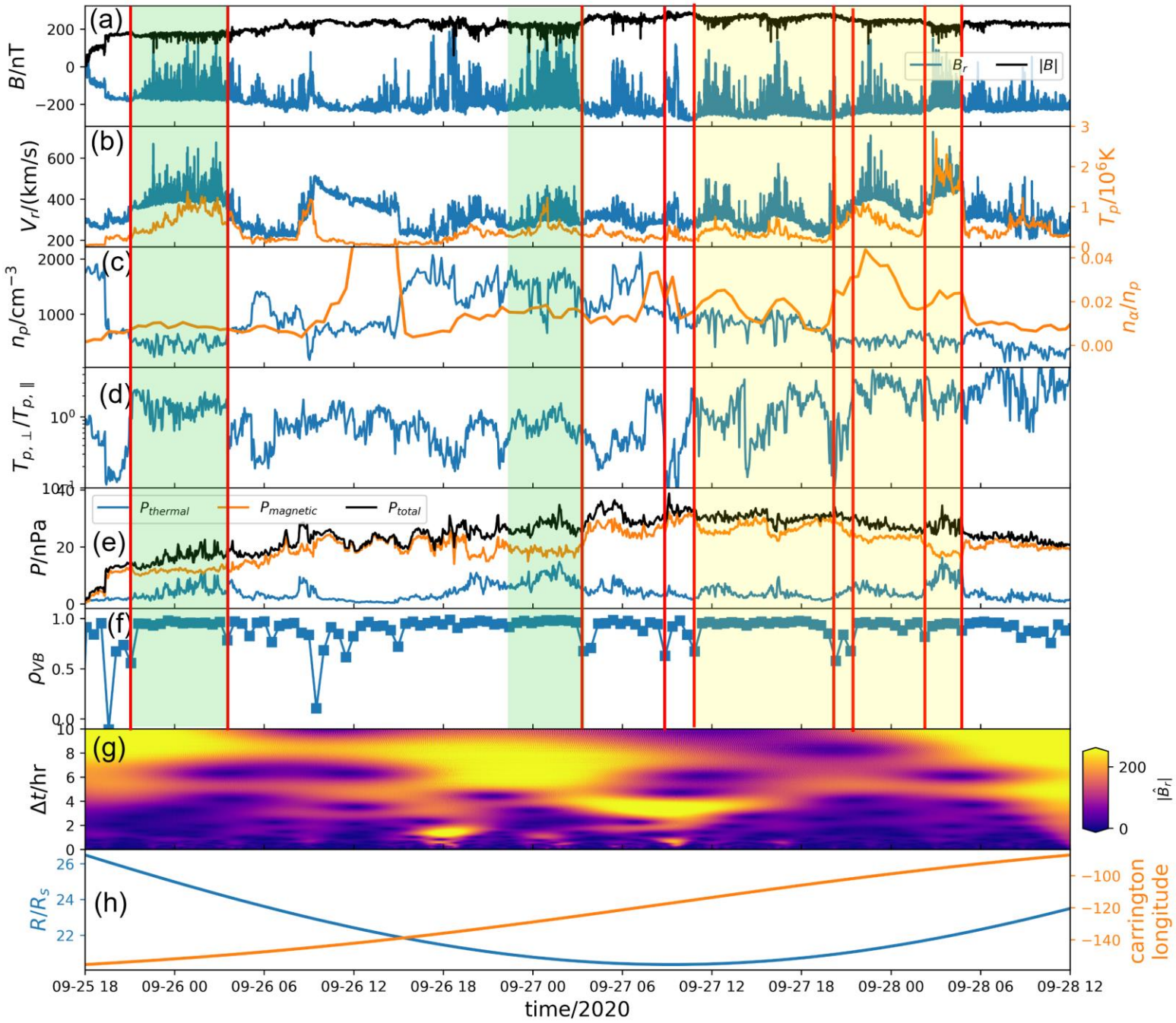
(a)
B/nT
200
0
−200
B_r
|B|
(b)
V_r/(km/s)
600
400
200
$T_p/10^6$K
3
2
1
0
(c)
n_p/cm^{-3}
2000
1000
n_α/n_p
0.04
0.02
0.00
(d)
$T_{p,\perp}/T_{p,\parallel}$
10^0
10^{-1}
(e)
$P_{thermal}$
$P_{magnetic}$
P_{total}
P/nPa
40
20
0
(f)
ρ_{VB}
1.0
0.5
0.0
(g)
Δt/hr
10
8
6
4
2
0
200
0
$|\hat{B}_r|$
(h)
R/R_s
26
24
22
−100
−120
−140
carrington longitude
09-25 18
09-26 00
09-26 06
09-26 12
09-26 18
09-27 00
09-27 06
09-27 12
09-27 18
09-28 00
09-28 06
09-28 12
time/2020

Encounter 6

Supergranule cell scales
may range from 20-75 Mm
Normally
30-36 Mm

Rincon&Rieutord
Living Reviews in Solar Physics ***volume 15,***
Article number: 6 (2018)

Lifetime 24-48 hours

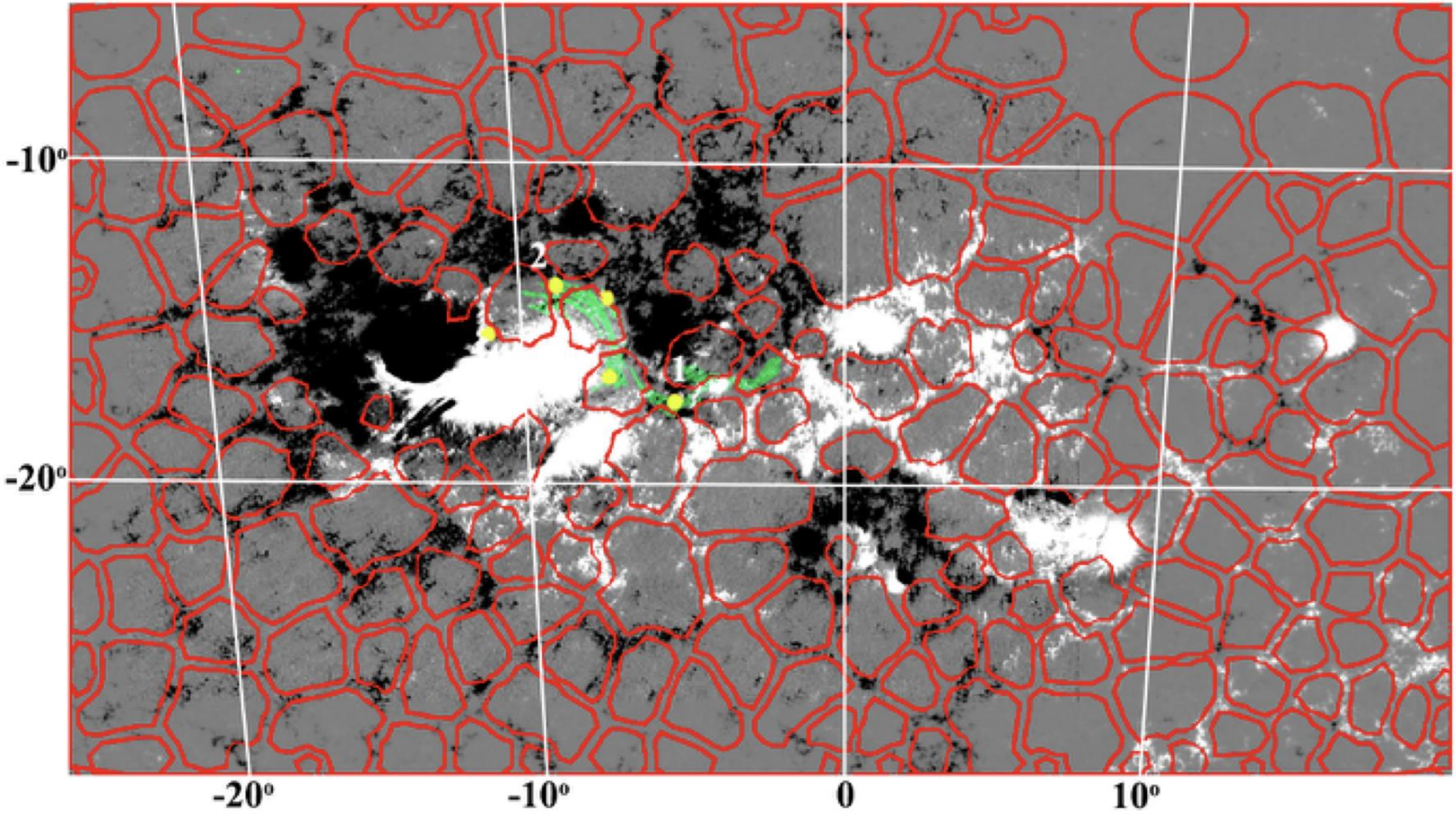

Red cells – supergranules.
AR 11520: HMI magnetogram with filament threads and barbs superposed. Yellow points are sites of the strong magnetic field cancellation = endpoints of barbs = intersections of supergranular cells.

Supergranulation – Panasenco et al. 2021

Solar wind origin/acceleration

Time series measurements of the solar wind plasma and magnetic field through the November 2021 solar encounter. a,b, Hot solar wind ions in a extend in energy to greater than 85 keV as suprathermal tails o the proton particle distribution in b. c, Red arcs mark the solar wind radial
velocity (VR) microstream structure that is organized in Carrington longitude at angular scales associated with supergranulation convection and thenphotospheric network magnetic field (Fig. 2). These microstreams become shorter in duration as the spacecraft accelerates through perihelion near the centre of this figure and sweeps more rapidly through Carrington longitude.
The thermal alpha particle abundance (AHe, blue trace in c) is similarly modulated by the microstream structure. The alpha particle abundance is
frozen-in at the base of the corona. d, Reversals of the radial magnetic field (BR), so-called ‘switchbacks’, are organized by the microstreams and are linked to the radial flow bursts by the Alfv.nicity condition. e, Photospheric footpoints from a PFSS model instantiation indicate two distinct coronal hole sources well separated in Carrington longitude (Lon), shown in Fig. 2 (and as dotted lines in Fig. 1e).

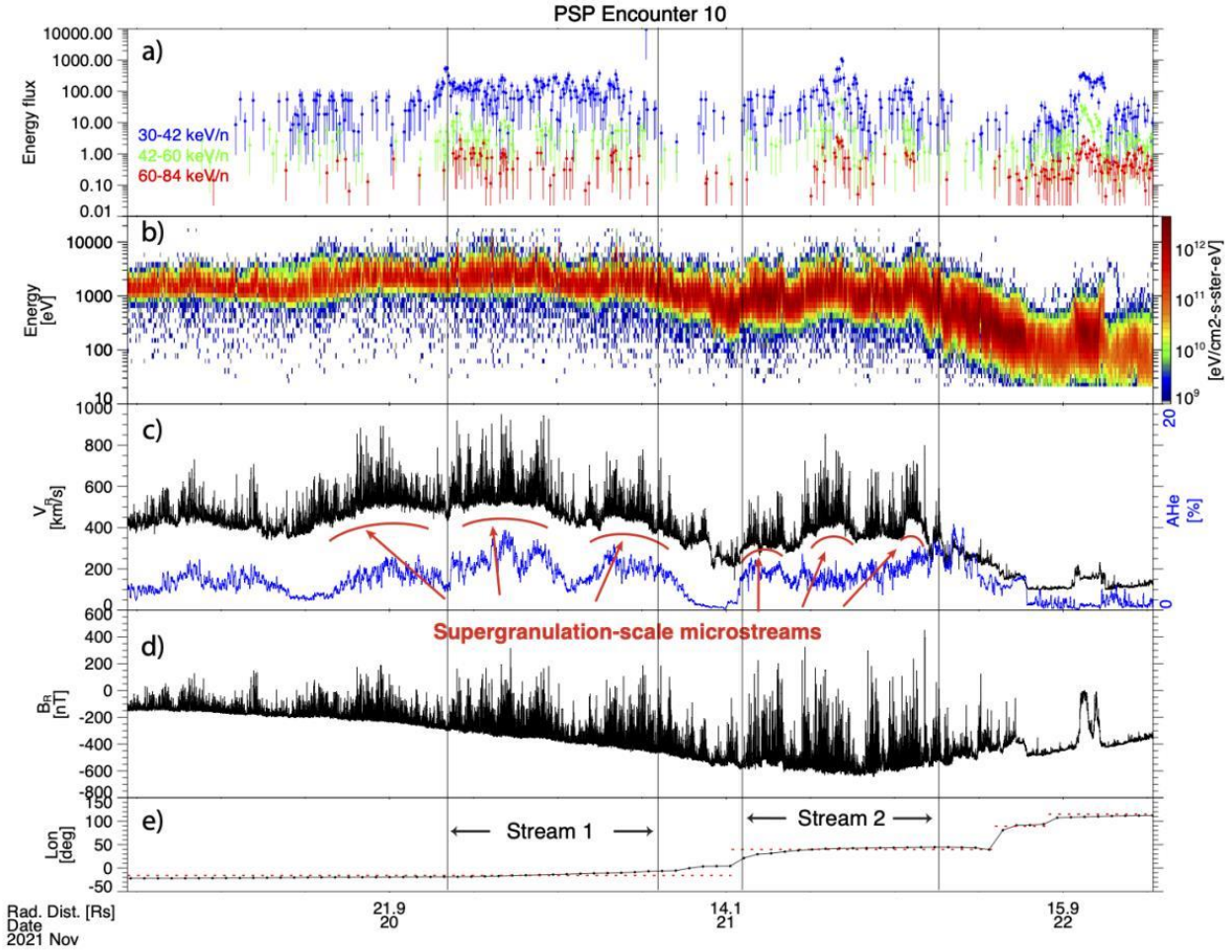

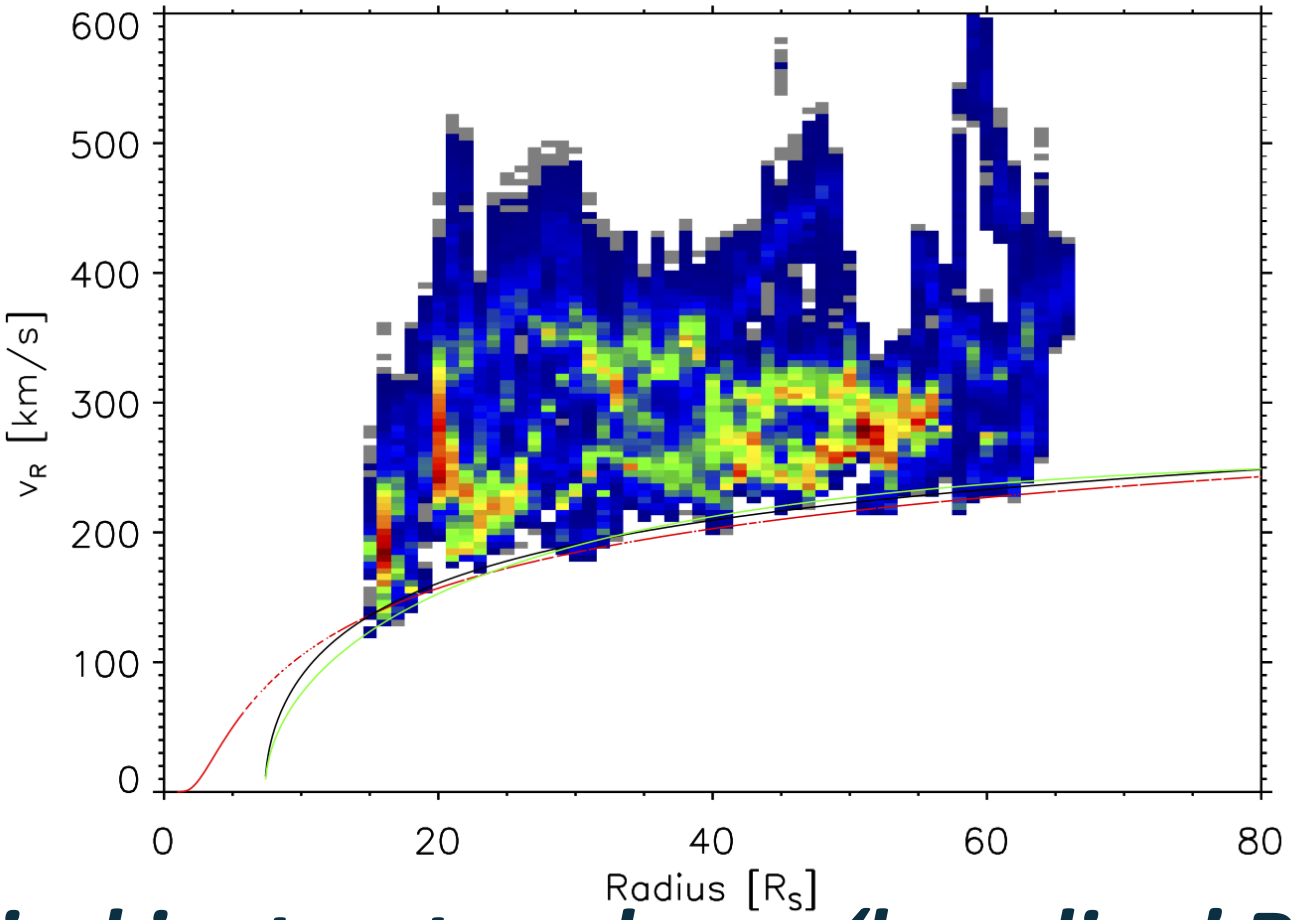

The solar wind is structured as a 'baseline' Parker-like wind beneath smaller-scale microstreams that emerge from supergranulation cell boundaries (Bale et al., 2021, Bale et al., 2022)

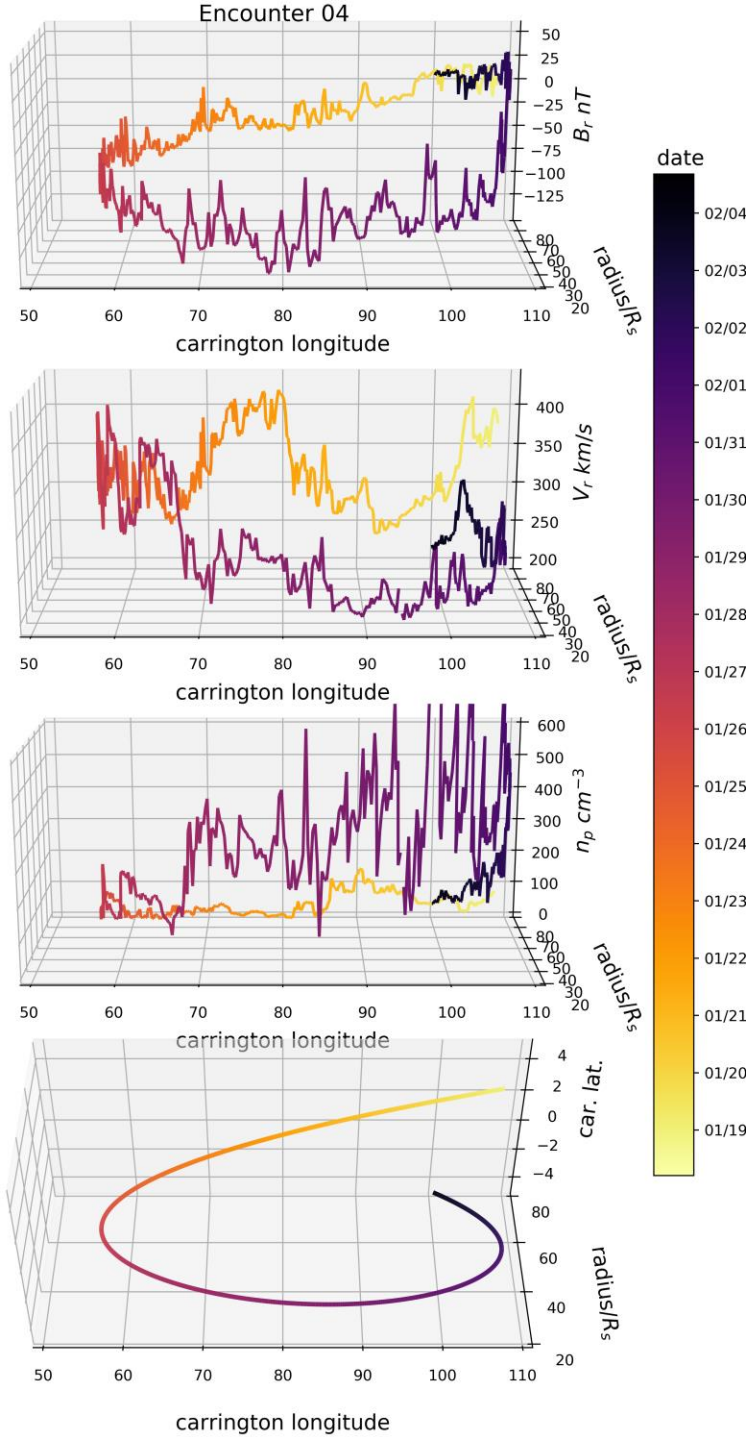

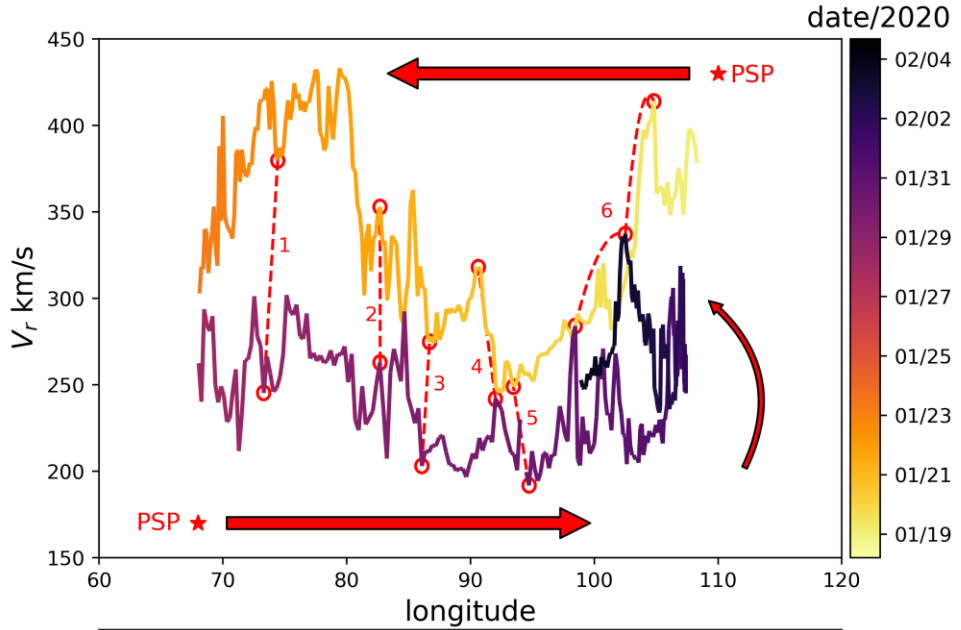

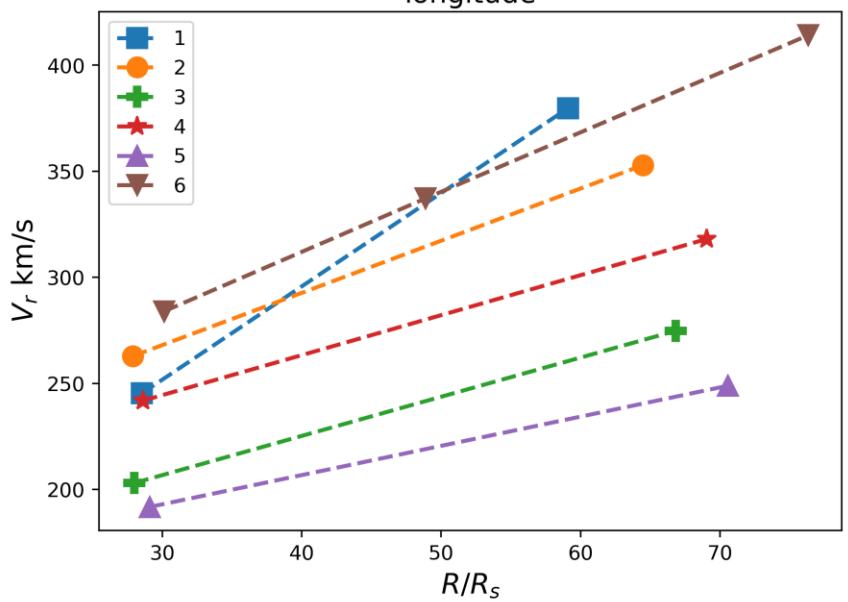

Shi et al 2021

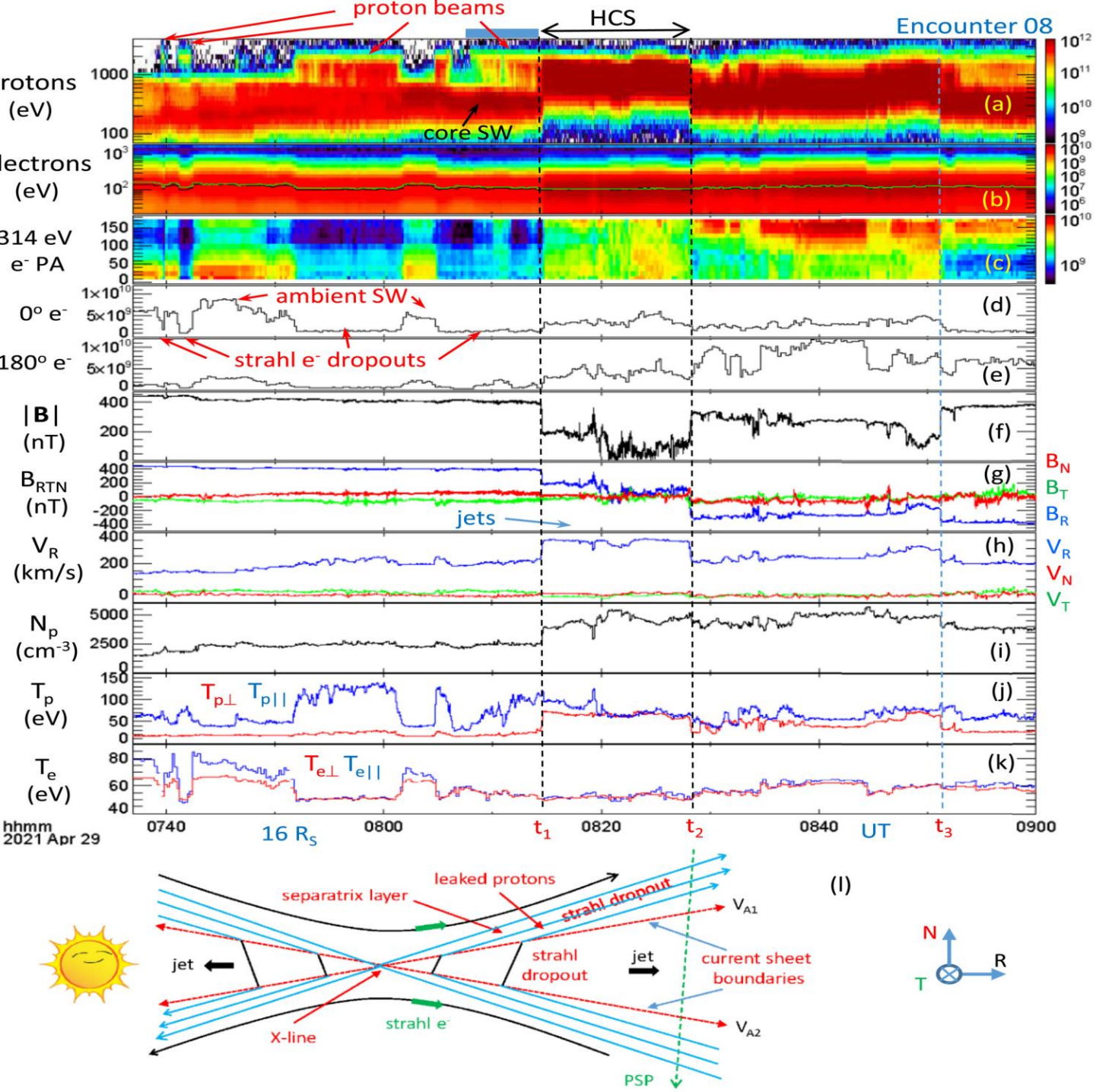

Phan et al. 2022

Reconnection seen in the Solar Wind

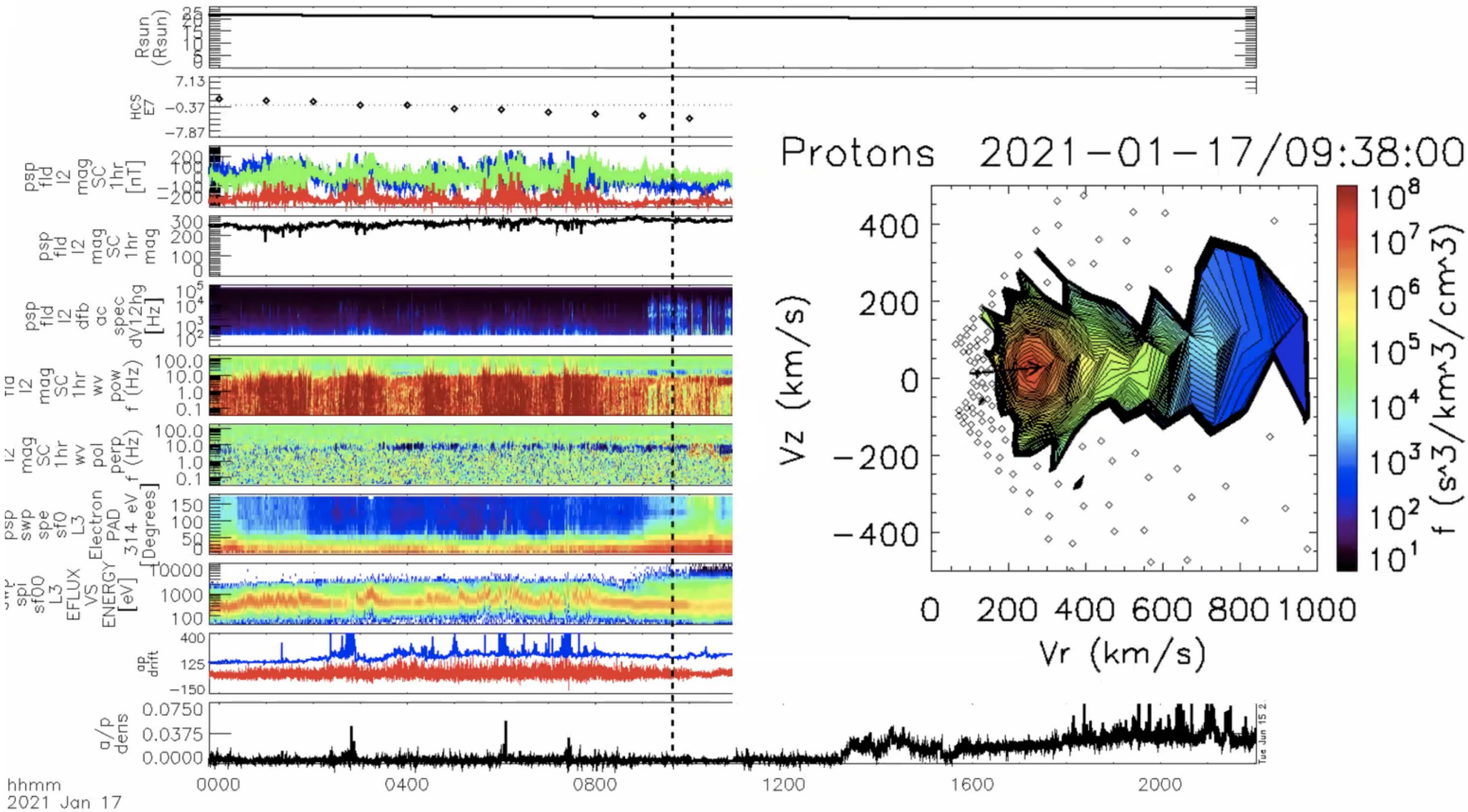

Verniero et al. 2021

PFSS/HMI footpoints and SECCHI 171 Map

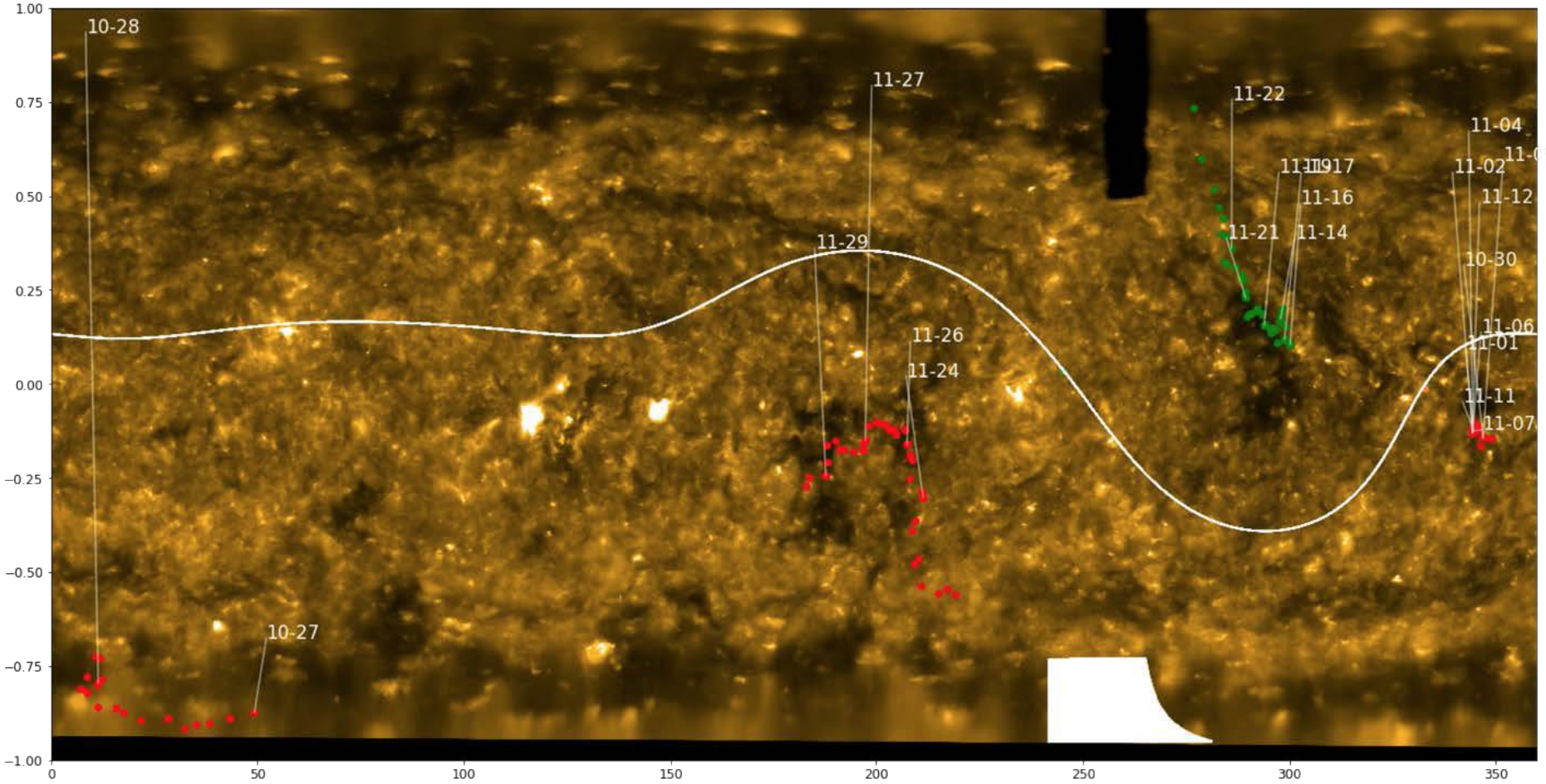

Encounter 1: Slow Alfvenic Wind from a rapidly Expanding Coronal Hole

Why fast and Slow Solar Wind ?
Magnetic Cage

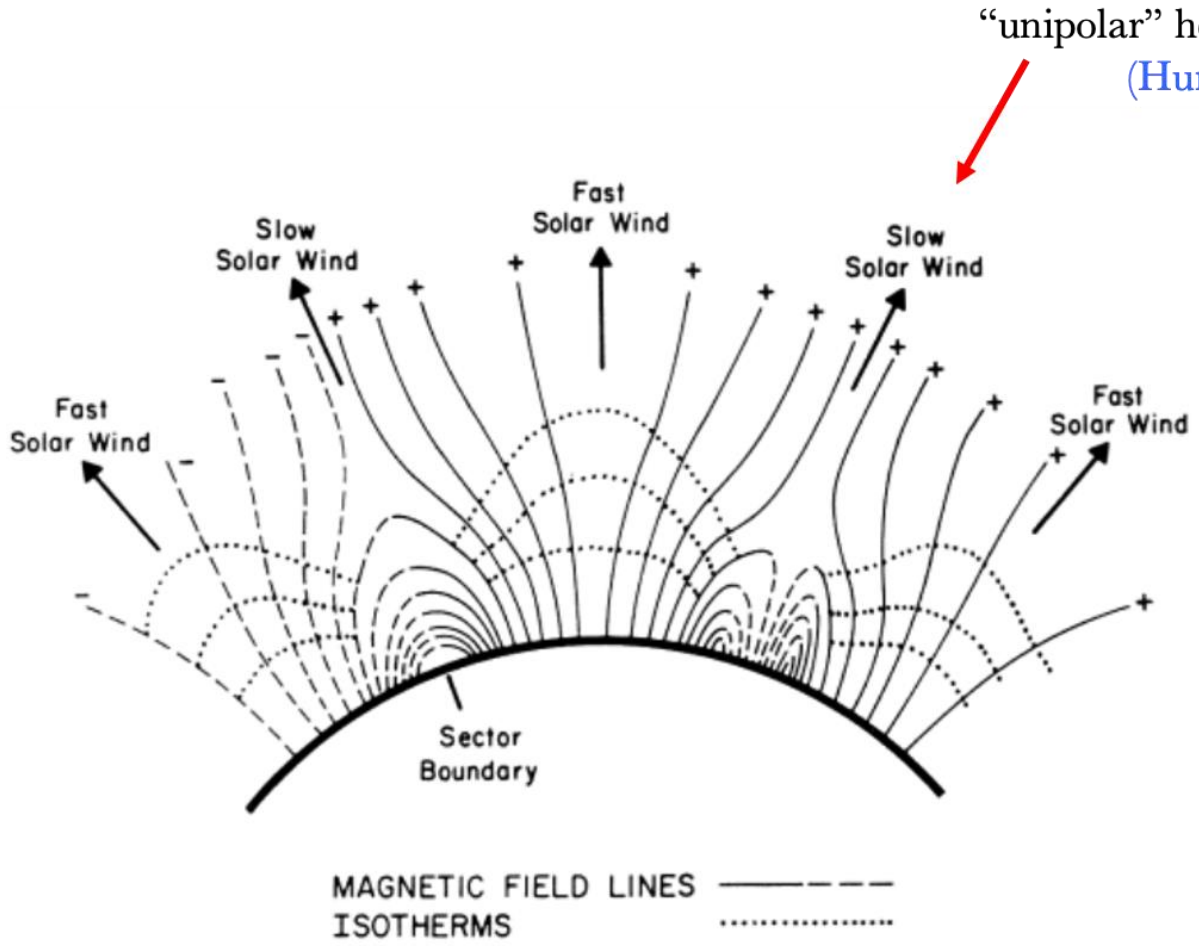

Fig. 7.1 A qualitative (and speculative) sketch of the coronal structure responsible for high-speed plasma streams. This picture is similar to that of Billings and Roberts (Fig. 5.33) except in details (such as the extension of isotherms in closed field regions)

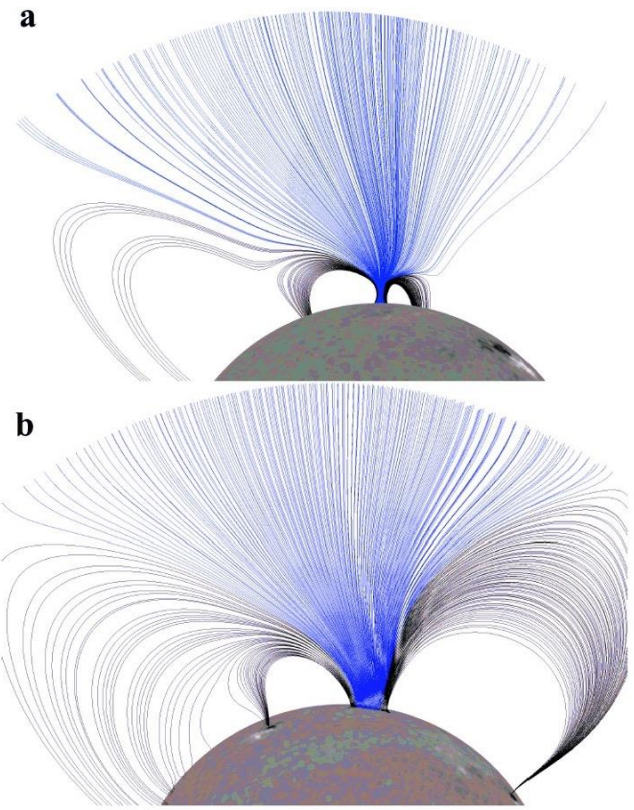

Figure 11. Comparison between funnel-like (a) and regular open magnetic fields (b). The funnel open field (PFSS for Sep 06) evolved into a regular coronal hole one rotation later (PFSS for October 6, 2012). The magnetic field lines for a regular coronal hole (b) show monotonic radial expansion - no rapid funnel-like expansion (PFSS field lines rotated to give a limb view).

Panasenco & Velli 2019

Pseudostreamers are a second defining feature of the corona

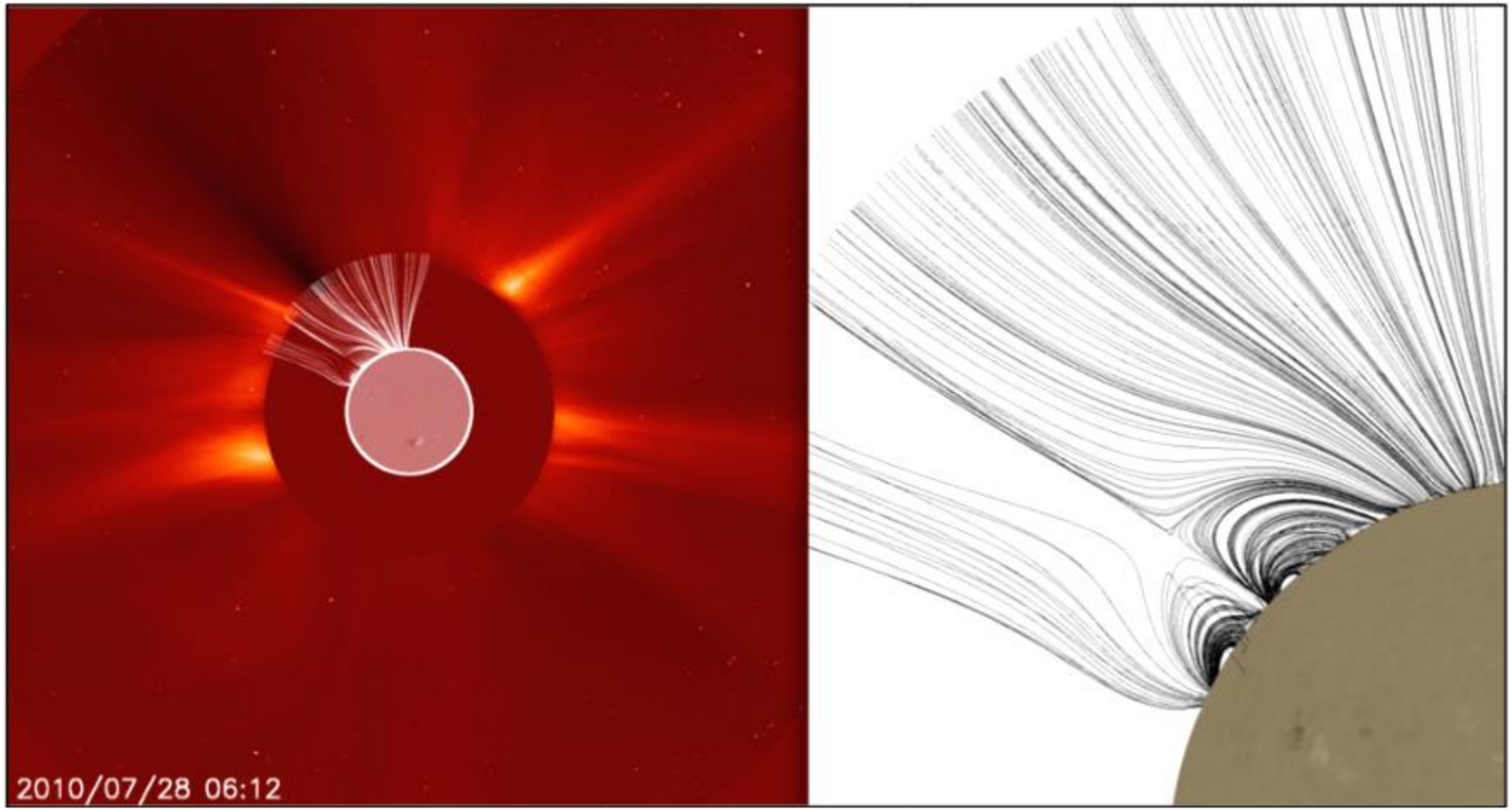

Where and how does the sharp gradient in speeds develop close to the Sun?

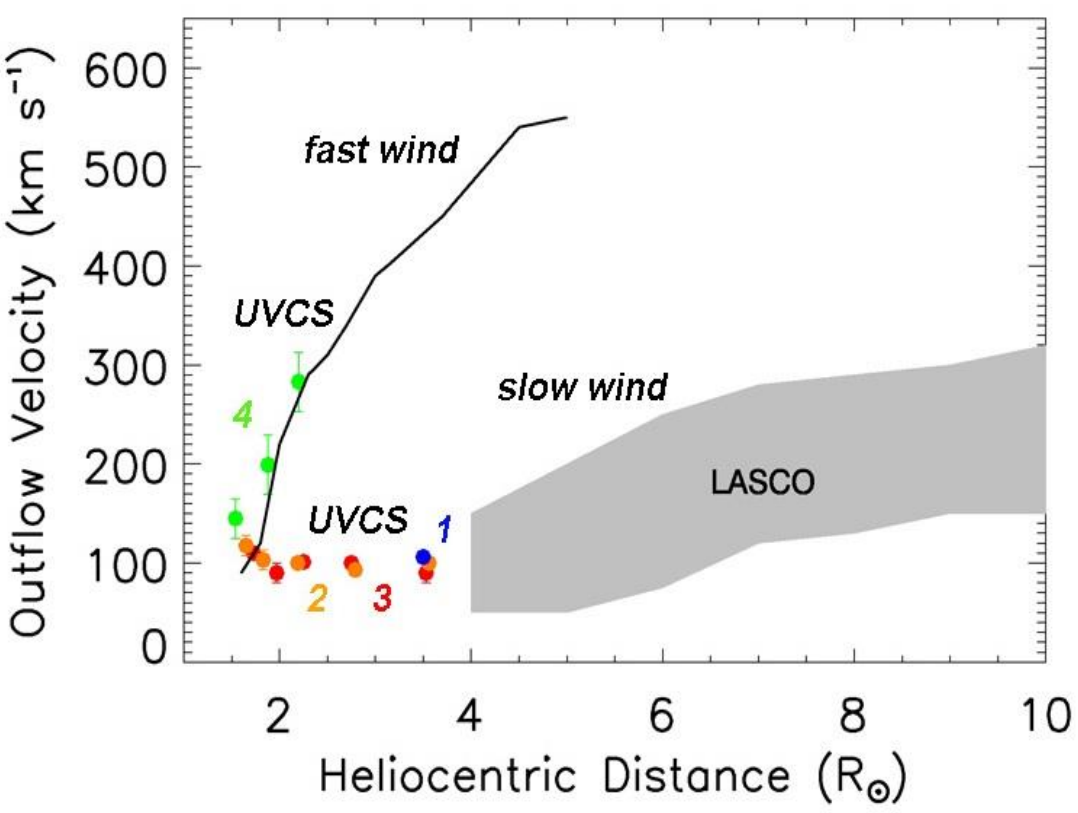

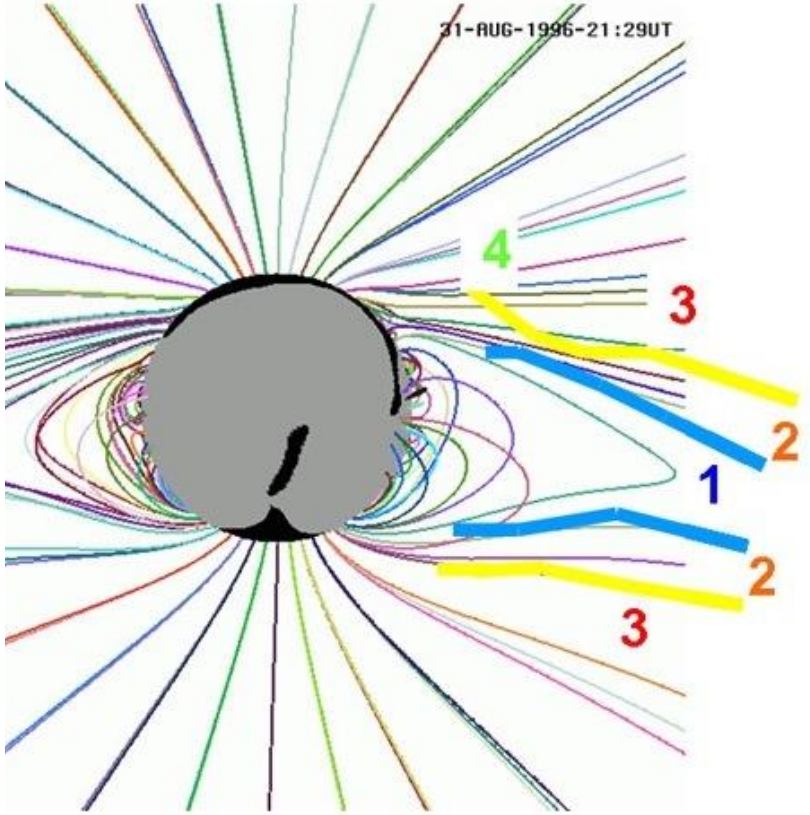

Antonucci et al., Telloni et al.

UVCS on SOHO suggest slow/fast separation already in place by 9 Rs

Where and how does the sharp gradient in speeds develop close to the Sun?

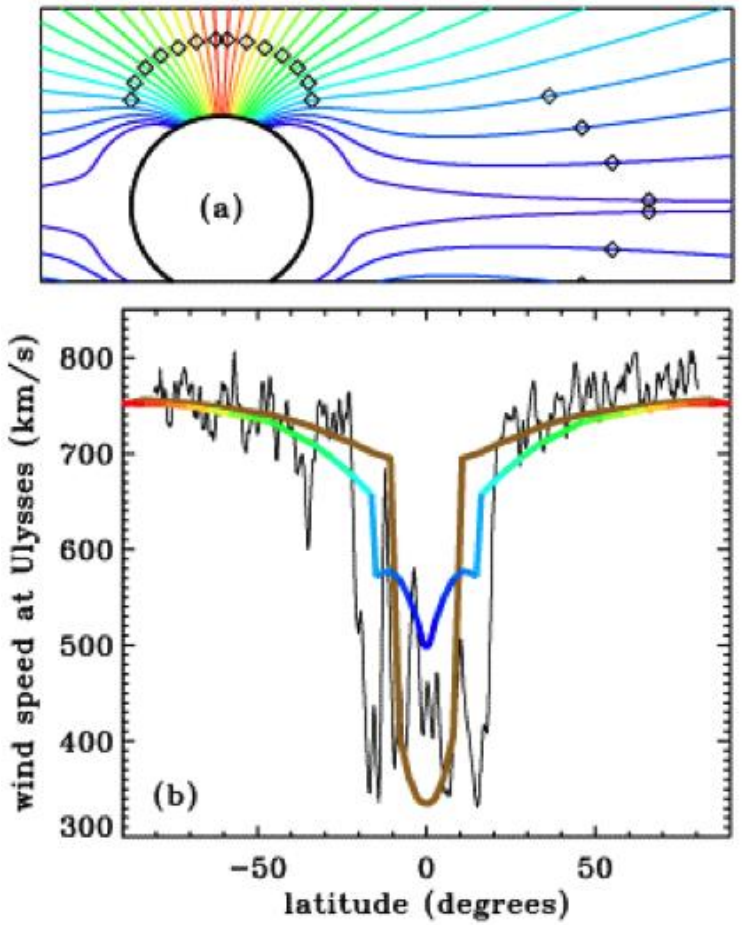

Cranmer et al. 2008

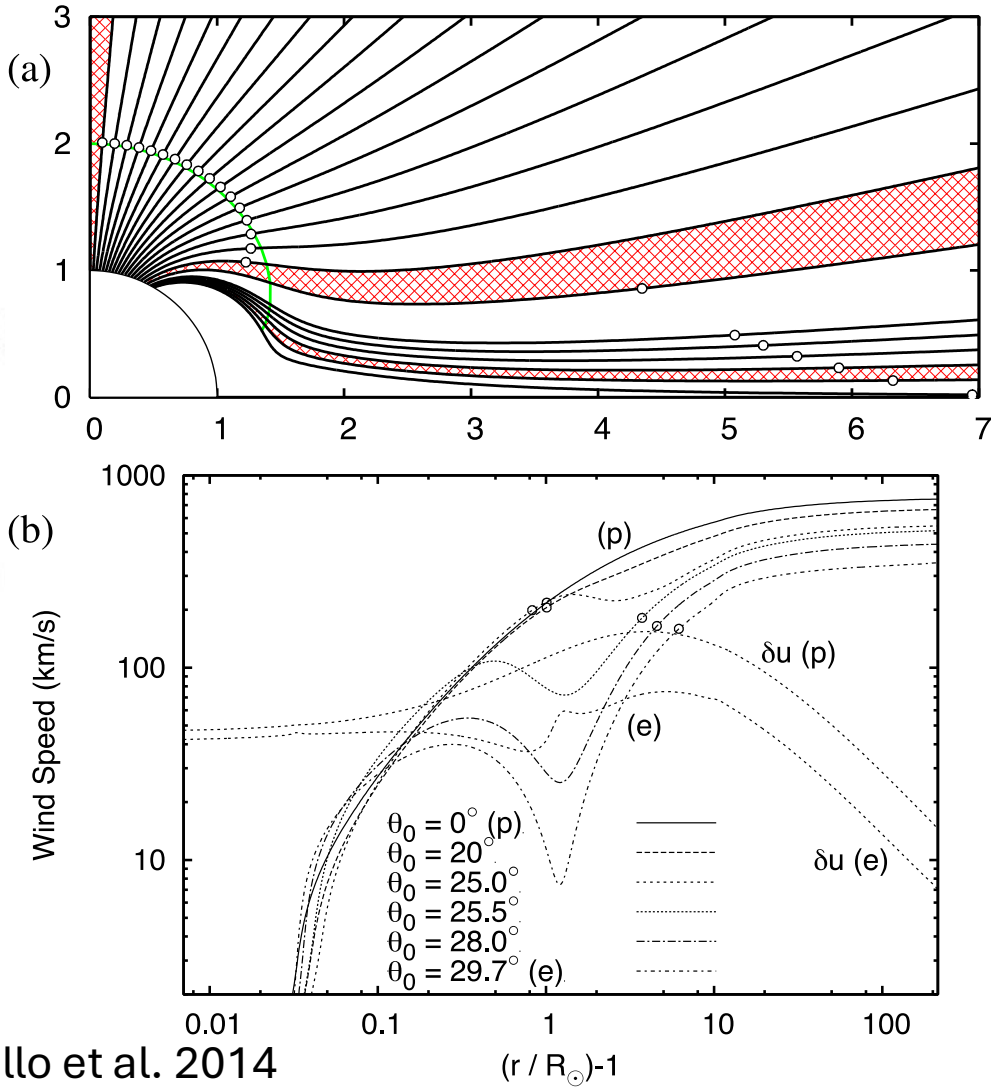

Lionello et al. 2014

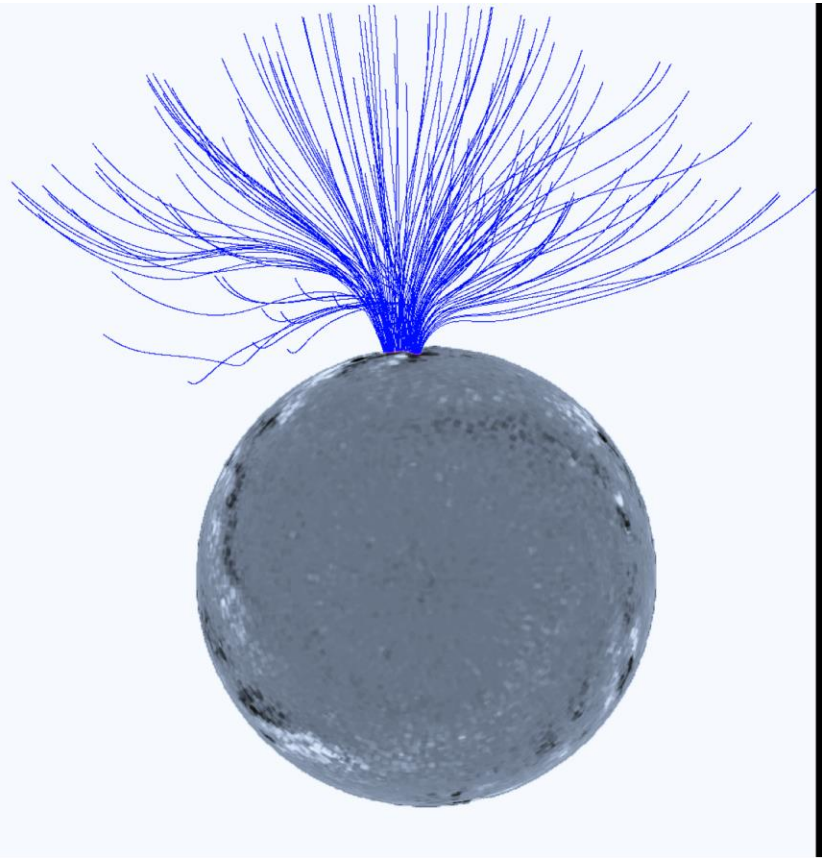

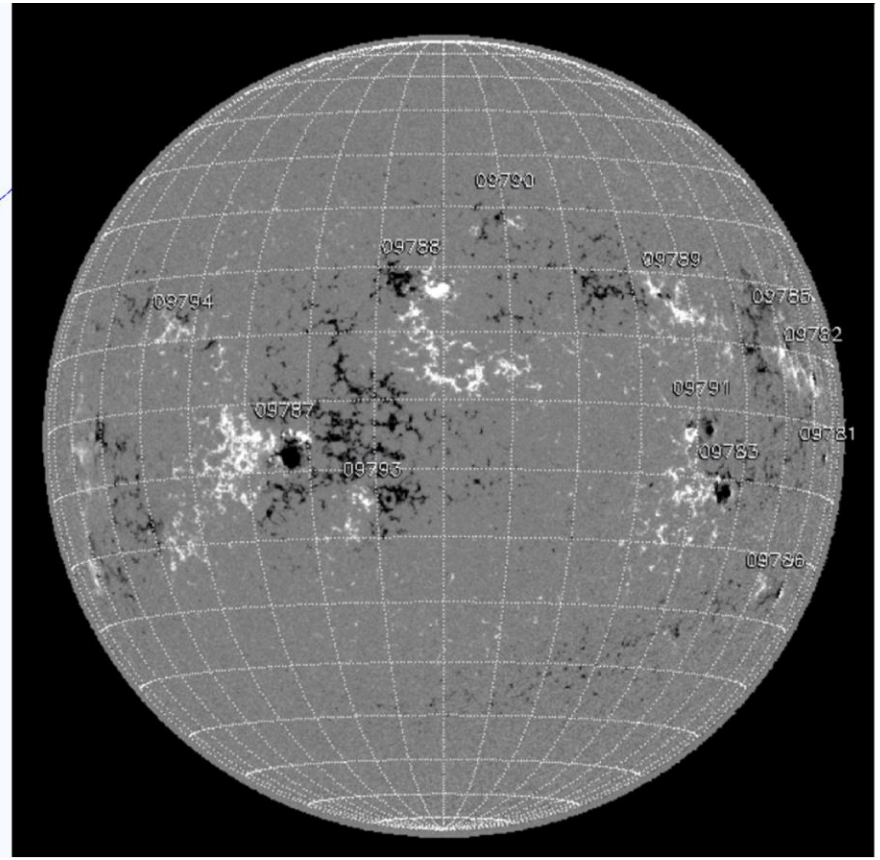

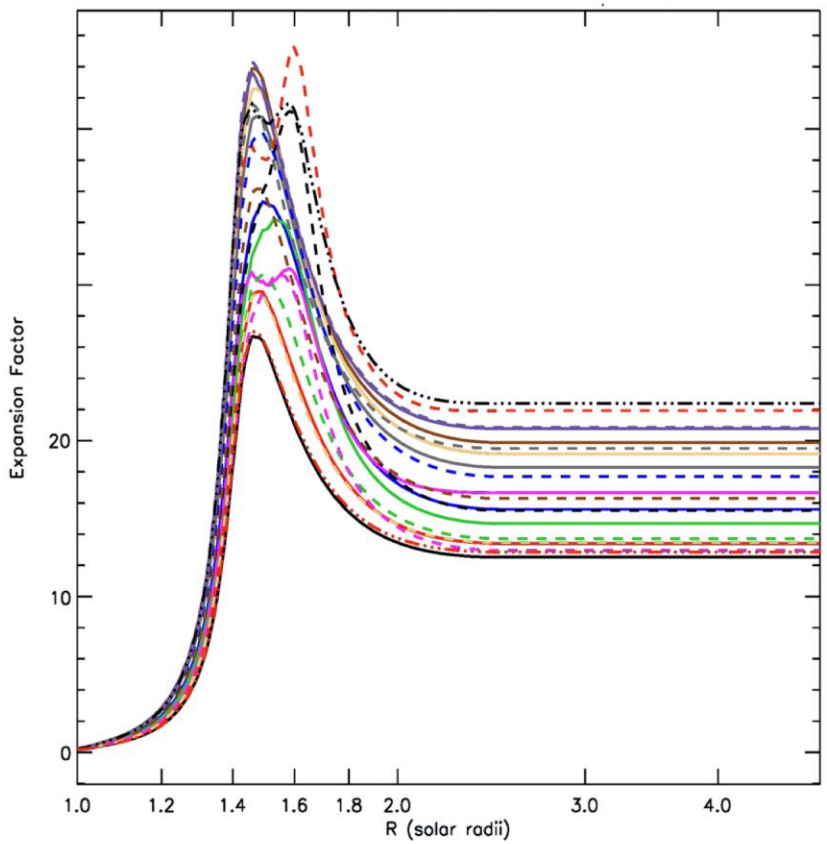

Panasenco et al. 2018

Connection between coronal sources, streamer belt, and heliospheric current sheet (S-Web, Antiochos 2007.2011)

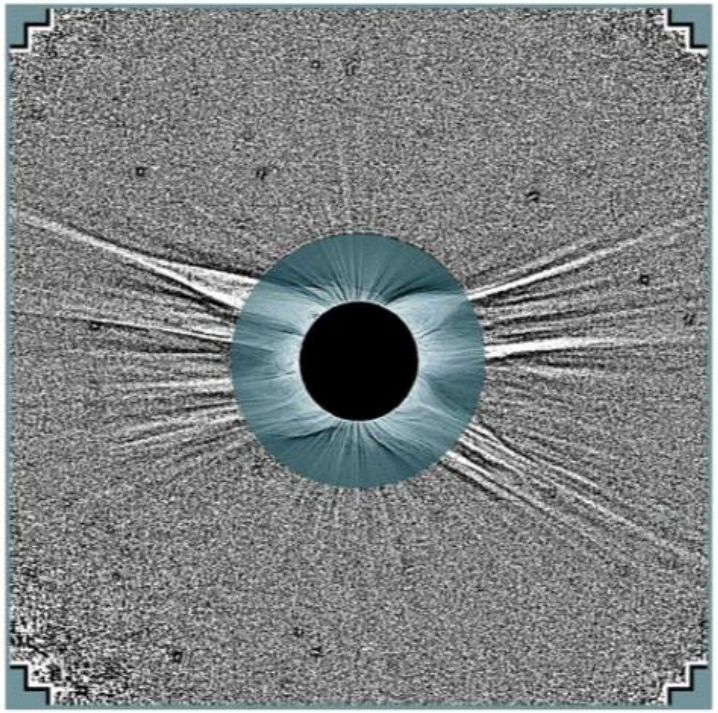

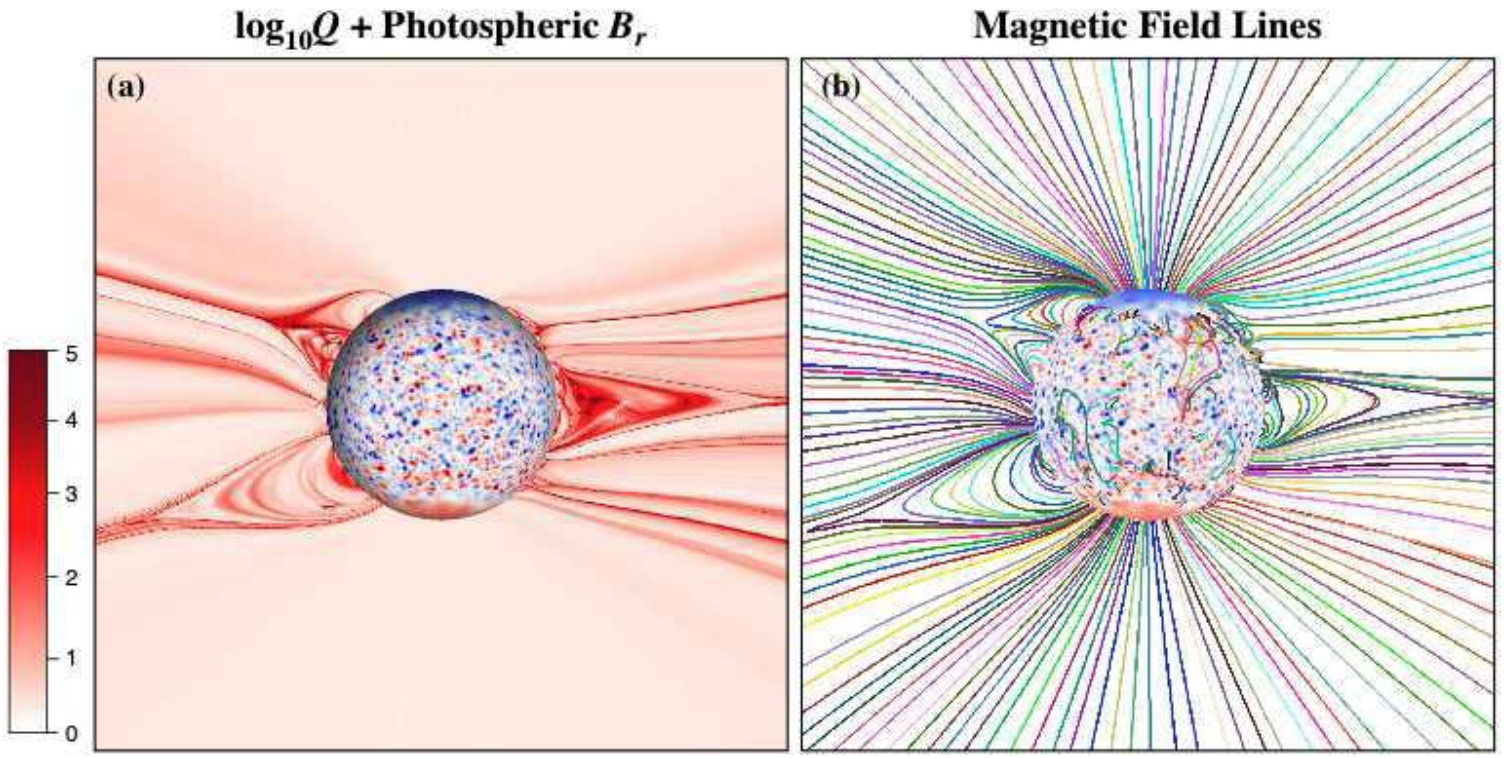

Fast and Slow Solar Wind Origins

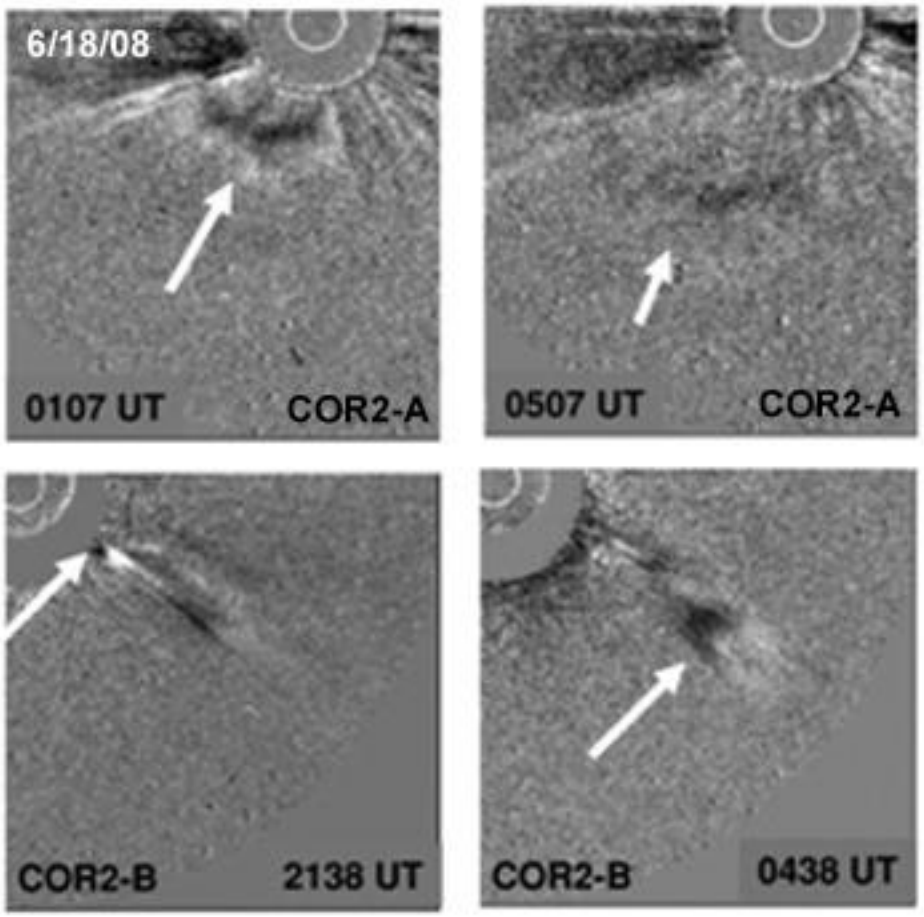

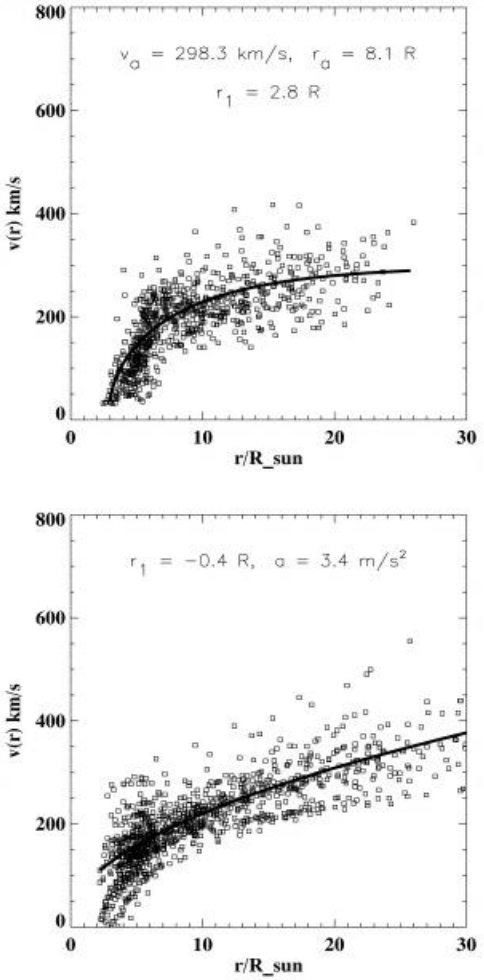

Sheeley et al 2009/Sheeley & Rouillard 2010

Sheeley, et al., 1997

Periodic density structures

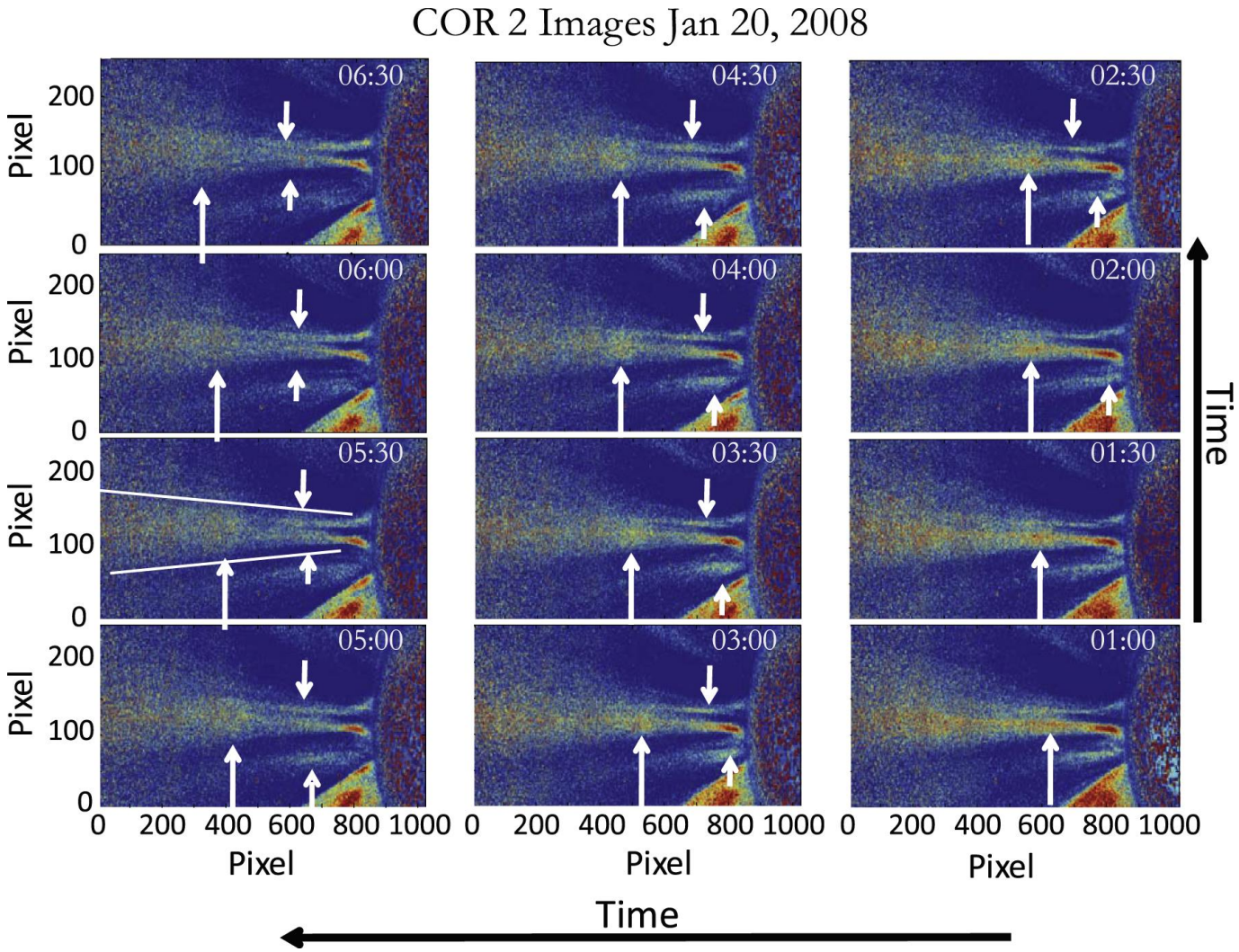

Structures with length scales of hundreds to several thousands of megameters and frequencies of tens to hundreds of minutes.

PDSs are formed in the solar corona as part of the slow solar wind release and/or acceleration processes. (Viall and Vourlidas 2015)

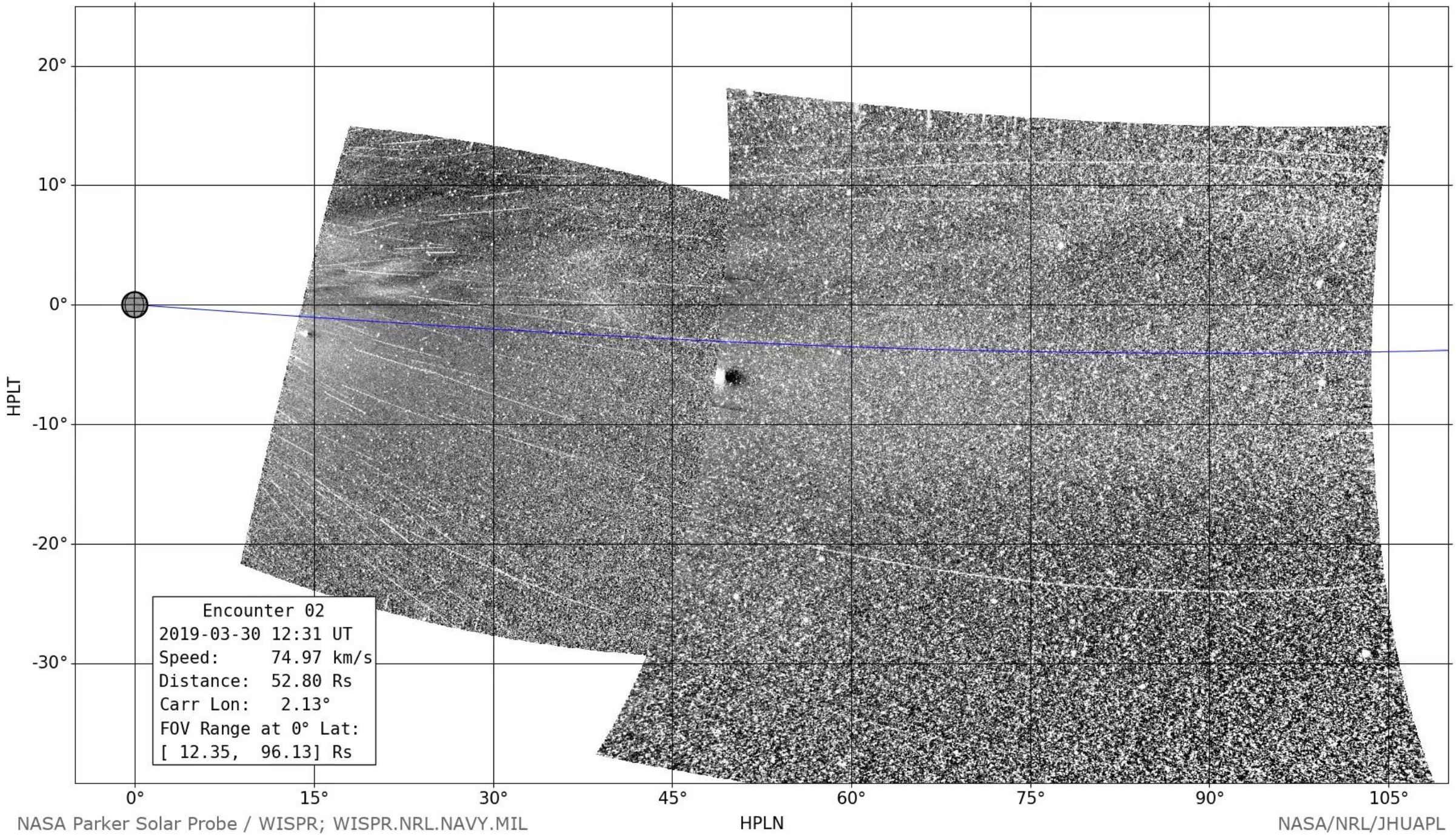
Encounter 02
2019-03-30 12:31 UT
Speed: 74.97 km/s
Distance: 52.80 Rs
Carr Lon: 2.13°
FOV Range at 0° Lat:
[12.35, 96.13] Rs
20°
10°
0°
-10°
-20°
-30°
HPLT
0°
15°
30°
45°
60°
75°
90°
105°
HPLN
NASA Parker Solar Probe / WISPR; WISPR.NRL.NAVY.MIL
NASA/NRL/JHUAPL

Tearing instability and periodic density perturbations in the slow solar wind

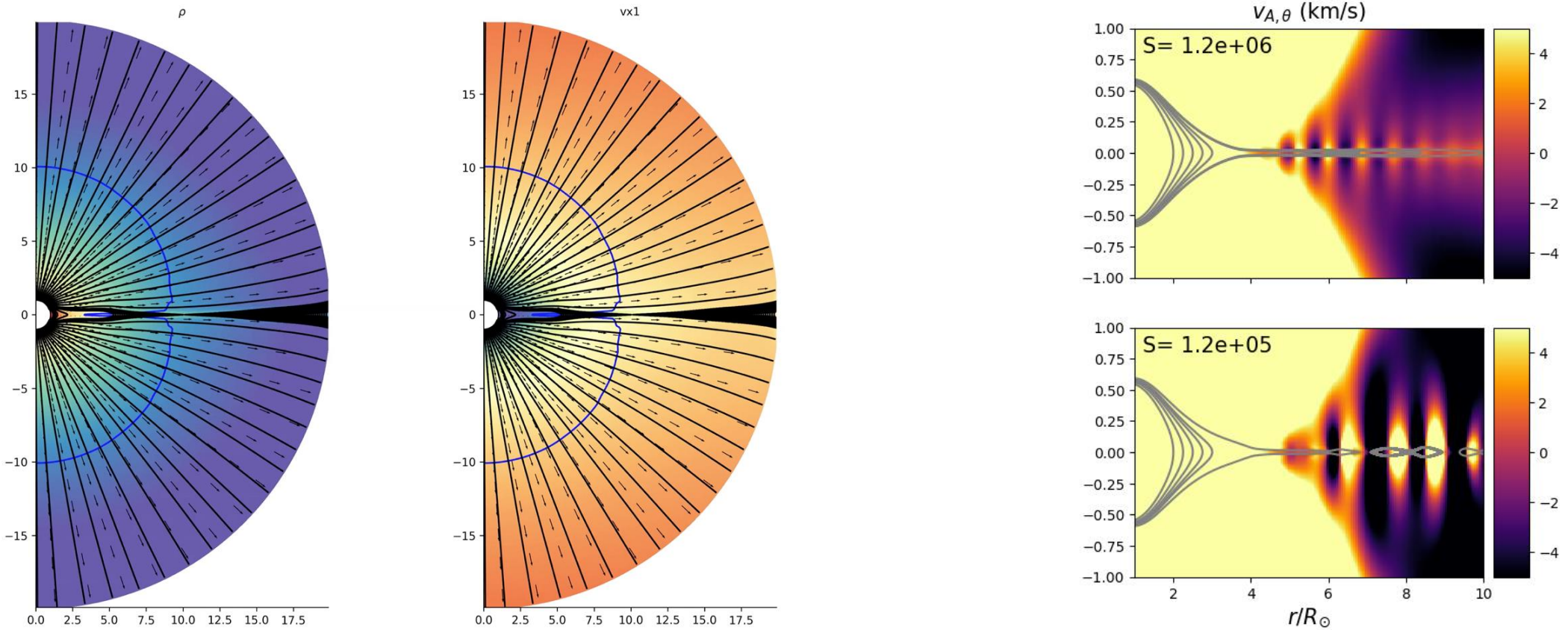

Snapshot of the fastest growing mode of a tearing instability in the current sheet. The background color is the latitudinal Alfvén speed $v_{A,\vartheta}$. The Lundquist number S is equal to 1.2×10^6, 1.2×10^5 in the top and the bottom panel, respectively. The aspect ratio is not respected to ease the visualization of the structures at the HCS. *(Reville, Velli et al. 2020)*

Flux ropes in the Heliospheric current sheet

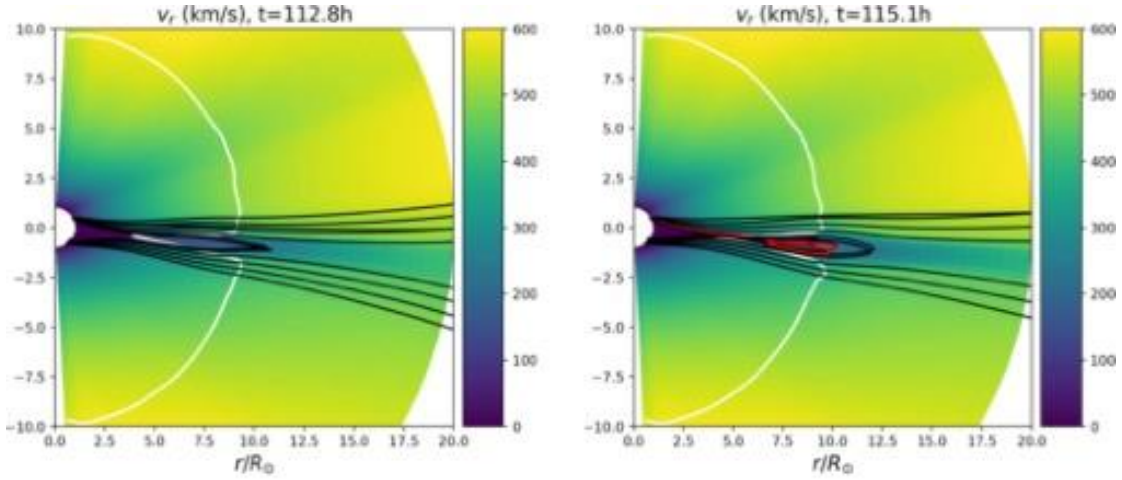

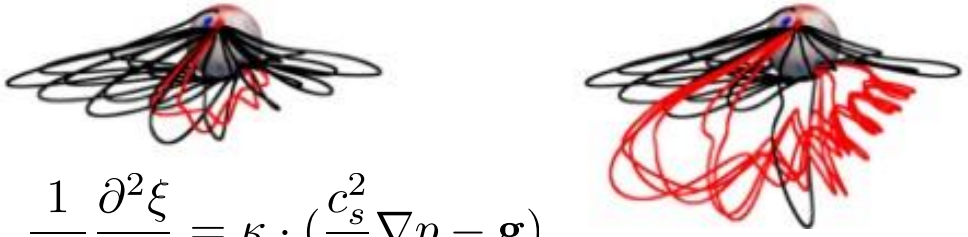

$$\frac{1}{R_c}\frac{\partial^2 \xi}{\partial t^2} = \kappa \cdot (\frac{c_s^2}{p}\nabla p - \mathbf{g})$$

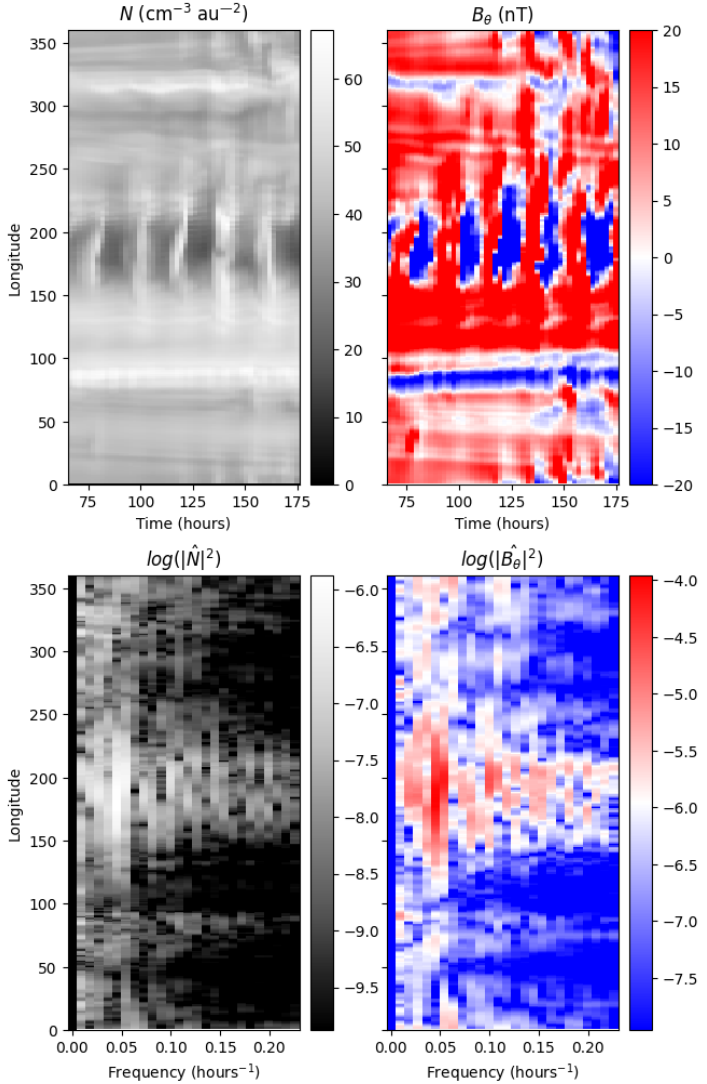

Connection between coronal sources, streamer belt, and heliospheric current sheet (S-Web, Antiochos 2007.2011)

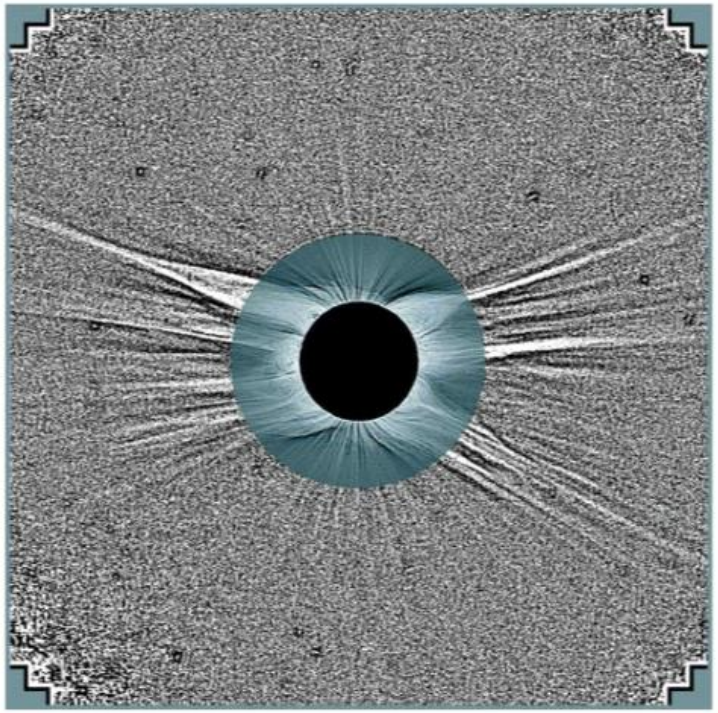

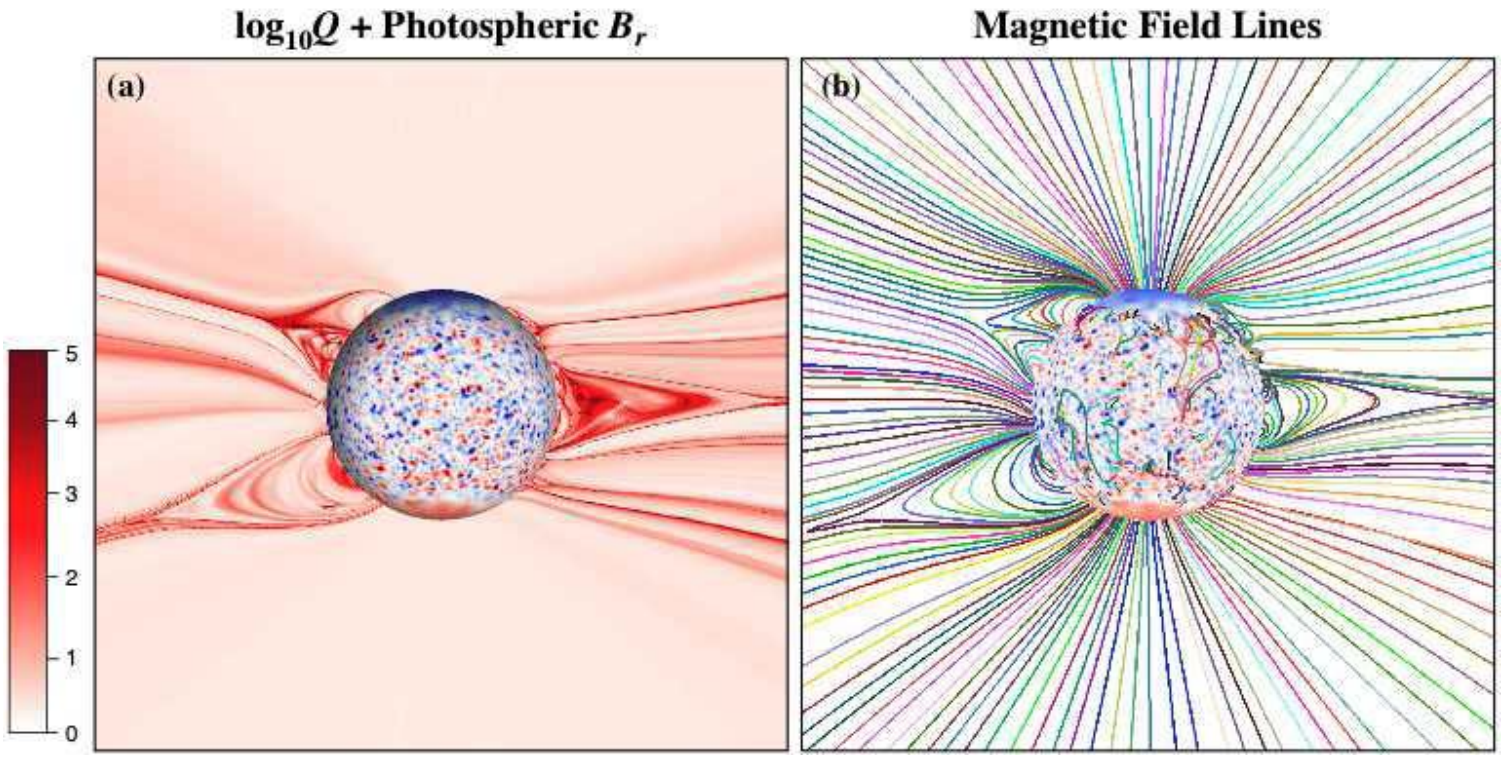

Single vs multiple heliospheric current sheets

THE ASTROPHYSICAL JOURNAL, 780:103 (8pp), 2014 January 1 doi:10.1088/0004-637X/780/1/
© 2014. The American Astronomical Society. All rights reserved. Printed in the U.S.A.

EVIDENCE FOR TWO SEPARATE HELIOSPHERIC CURRENT SHEETS OF CYLINDRICAL SHAPE DURING MID-2012

Y.-M. WANG[1], P. R. YOUNG[2], AND K. MUGLACH[3,4]
[1] Space Science Division, Naval Research Laboratory, Washington, DC 20375, USA; yi.wang@nrl.navy.mil
[2] College of Science, George Mason University, Fairfax, VA 22030, USA; pyoung@ssd5.nrl.navy.mil
[3] Code 674, NASA Goddard Space Flight Center, Greenbelt, MD 20771, USA; karin.muglach@nasa.gov
Received 2013 September 24; accepted 2013 November 20; published 2013 December 13

ABSTRACT

During the reversal of the Sun's polar fields at sunspot maximum, outward extrapolations of magnetograph measurements often predict the presence of two or more current sheets extending into the interplanetary medium, instead of the single heliospheric current sheet (HCS) that forms the basis of the standard "ballerina skirt" picture. By comparing potential-field source-surface models of the coronal streamer belt with white-light coronagraph observations, we deduce that the HCS was split into two distinct structures with circular cross sections during mid-2012. These cylindrical current sheets were centered near the heliographic equator and separated in longitude by roughly 180°; a corresponding four-sector polarity pattern was observed at Earth. Each cylinder enclosed a negative-polarity coronal hole that was identifiable in extreme ultraviolet images and gave rise to a high-speed stream. The two current sheet systems are shown to be a result of the dominance of the Sun's nonaxisymmetric quadrupole component, as the axial dipole field was undergoing its reversal during solar cycle 24.

Key words: interplanetary medium – solar wind – Sun: activity – Sun: corona – Sun: heliosphere – Sun: magnetic fields

Online-only material: color figures

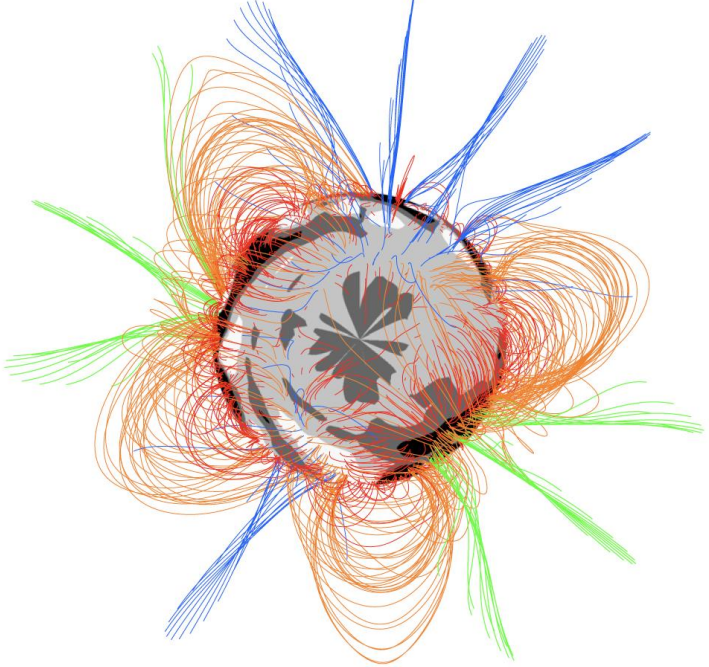

(a) MWO 2124 (SEEN FROM N POLE)

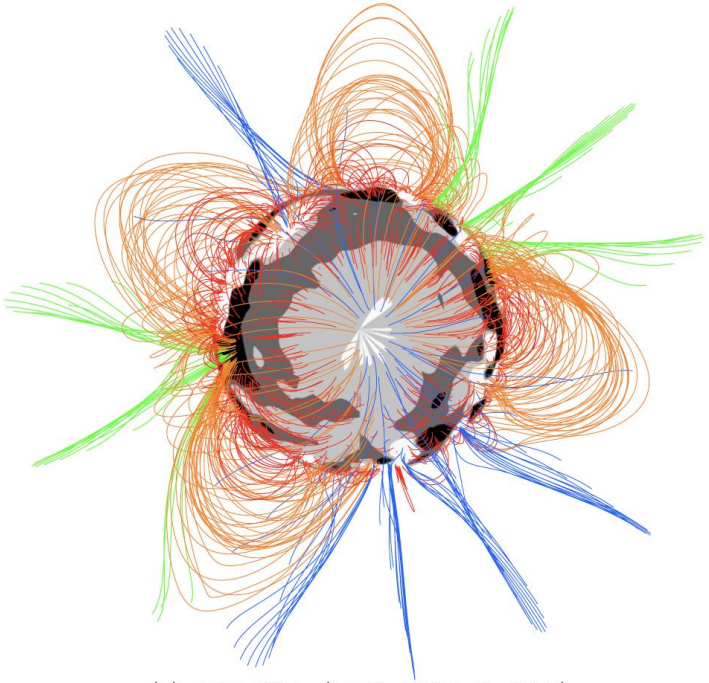

(b) MWO 2124 (SEEN FROM S POLE)

Slow Alfvénic Wind and Solar Wind Origins

Slow solar wind emerges in steady and non-steady ways from different solar coronal regions. Here we conjecture that slow wind emerging from rapidly expanding magnetic field WITHOUT large field gradients (low squashing factor Q) gives rise to SLOW ALFVENIC WIND (SA), seen frequently by PSP in its early orbits. The slow wind emerging from rapidly expanding AND large Q factor regions gives rise to slow wind that is NOT ALFVENIC (SNA)

Velli, Reville, Lionello et al. 2023 in preparation, uses two different 2D/3D MHD models. Below: twolegged distribution of slow wind, high exp and high Q, And high exp only. The first gives rise to SNA, the second to SA.

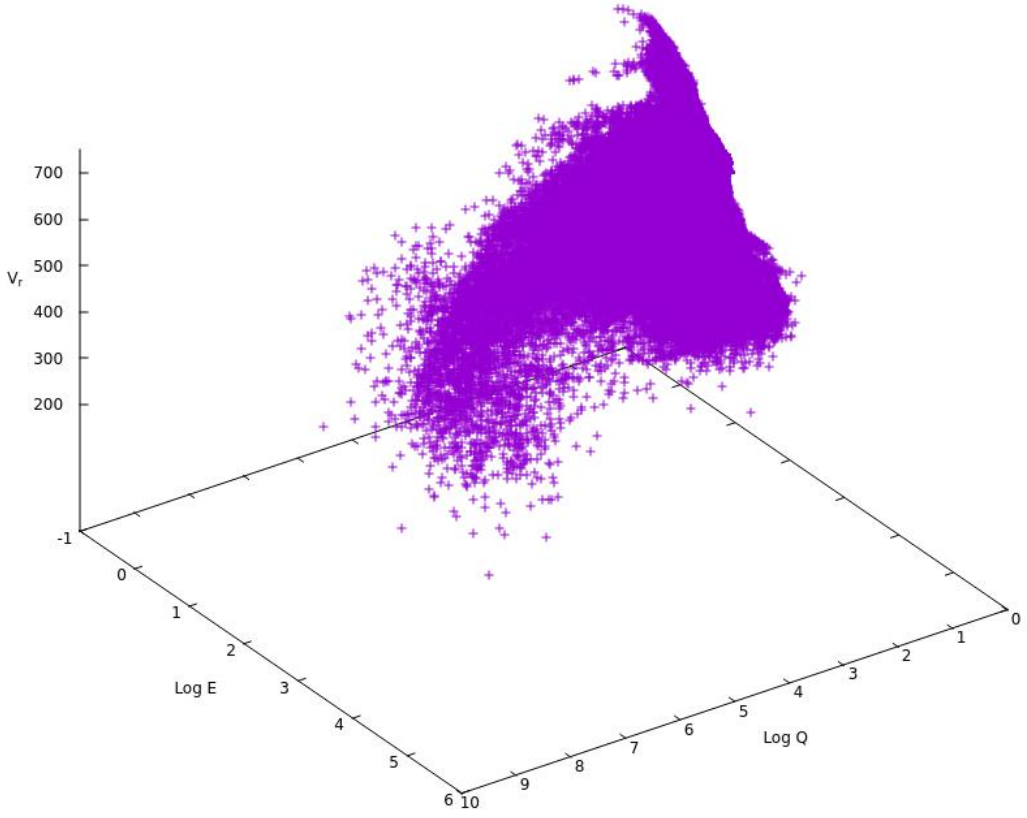

Right: speed and expansion factor. The slow wind of the middle donut is SNA, the purple slow to its left, SA.

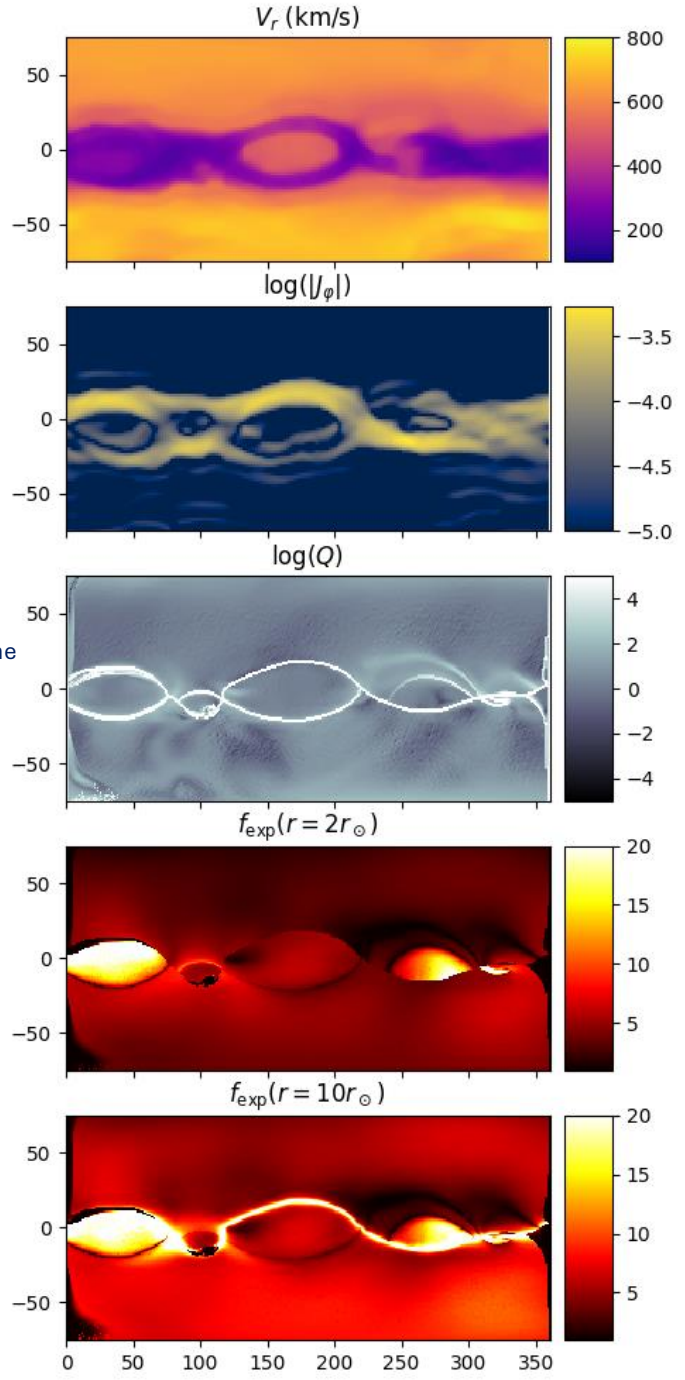

How does the Heliosphere end?

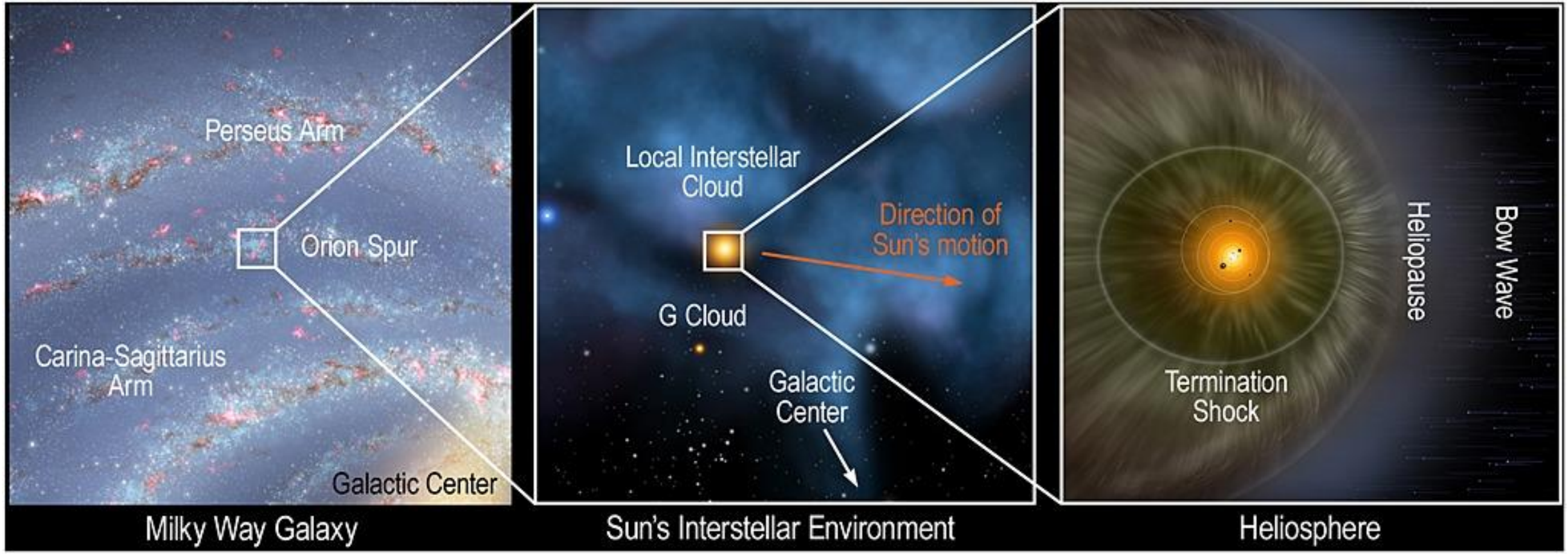

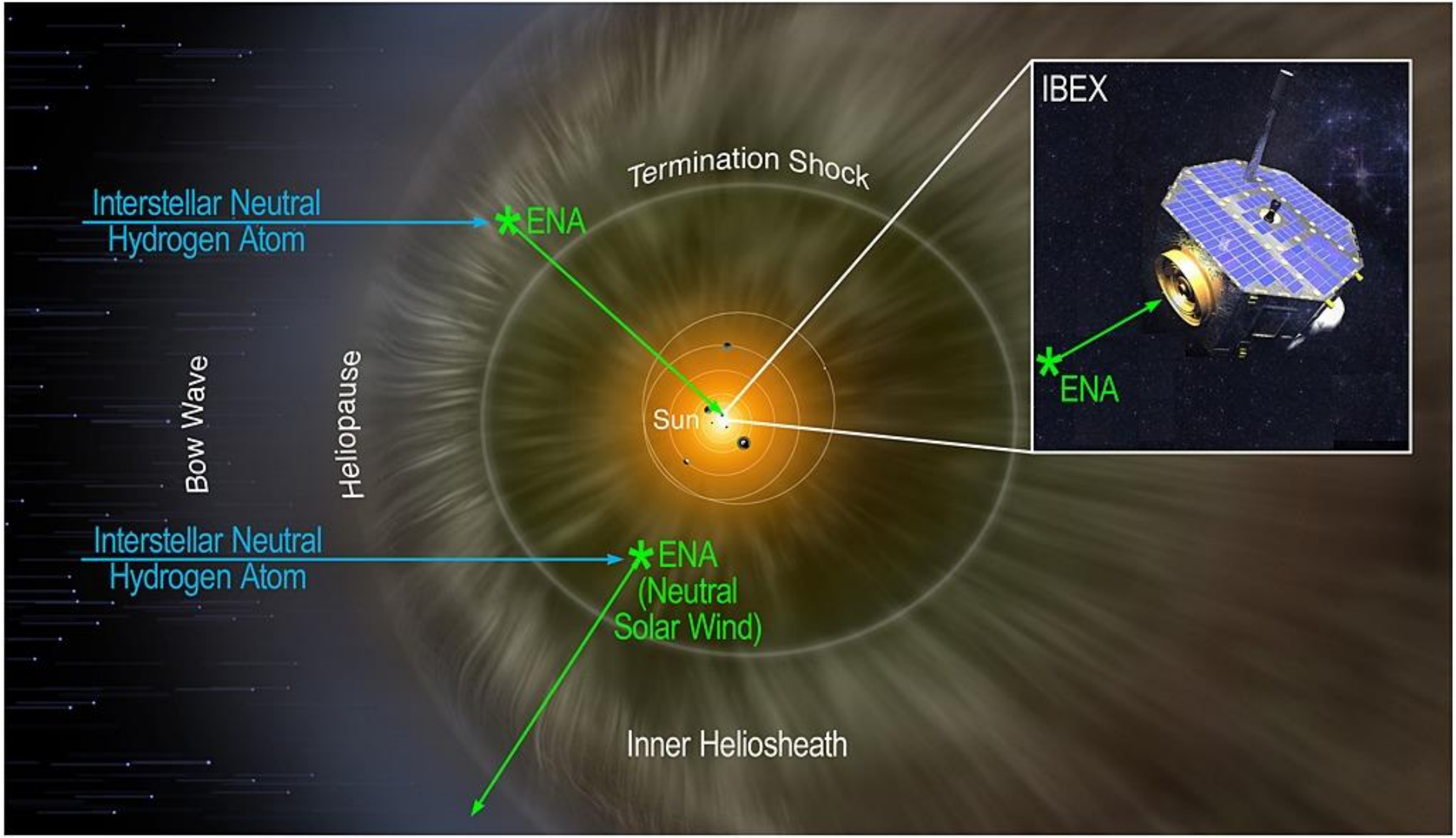
Interstellar Neutral
Hydrogen Atom
ENA
Termination Shock
IBEX
Bow Wave
Heliopause
Sun
ENA
Interstellar Neutral
Hydrogen Atom
ENA
(Neutral
Solar Wind)
Inner Heliosheath

Reasonable LISM plasma parameters indicate that the LISM flow may be either marginally super-fast magnetosonic or sub-fast magnetosonic.

Because the Mach number is only barely super-fast magnetosonic in the 3μG case, the hot and fast neutral H can completely mediate the transition and impose a charge exchange length scale on the structure, making the solar-wind–LISM interaction effectively bow-shock-free.

The charge exchange of fast and hot heliospheric neutral H therefore provides a primary dissipation mechanism at the weak heliospheric bow shock, in some cases effectively creating a one-shock heliosphere (i.e., a heliospheric termination shock only).

(Zank et al. 2013)

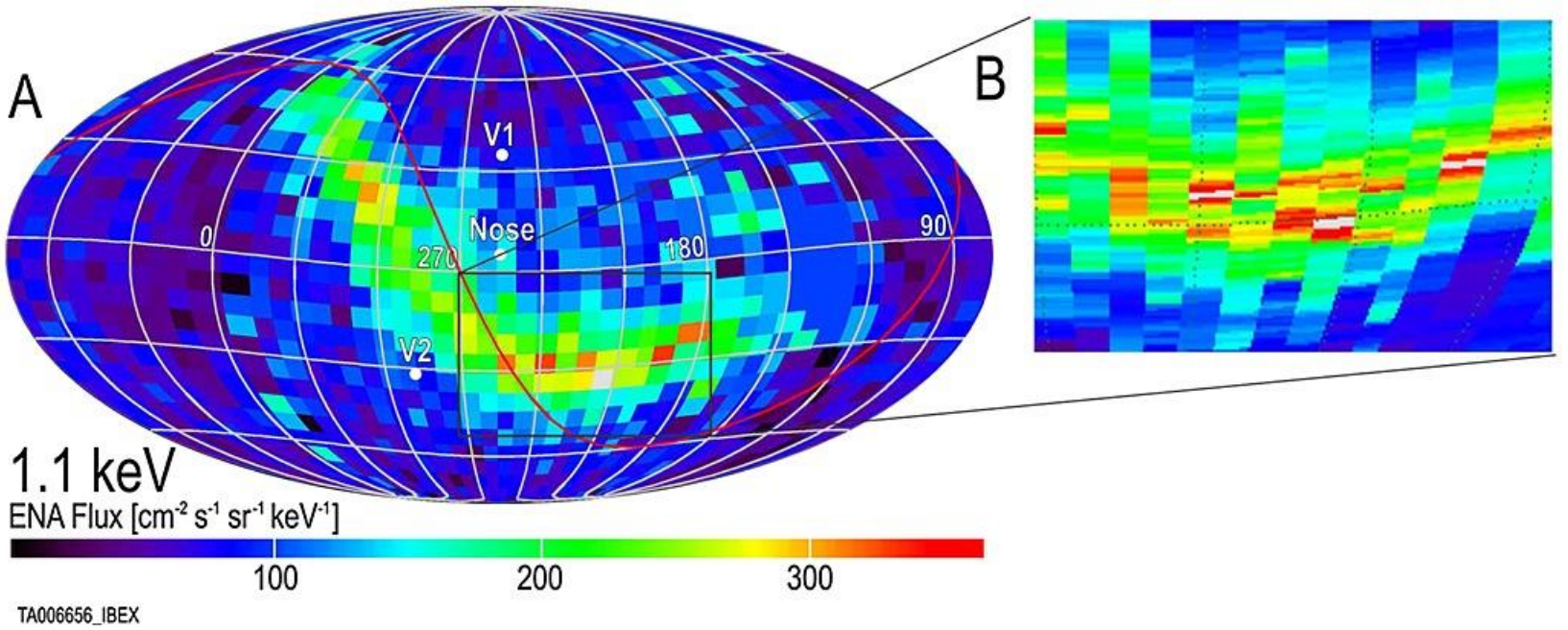

The ribbon is formed by the secondary ENA mechanism. ENAs created in the outward-propagating solar wind (SW) or from the inner heliosheath (IHS) exit the heliosphere into the denser local interstellar medium (LISM). These ENAs eventually charge exchange with interstellar ions, producing pickup ions (PUIs) that gyrate around the ISMF lines. The PUIs will neutralize again after a period of time depending on the PUI energy and the local neutral density, and they may travel back into the heliosphere. Due to their long mean free paths inside the heliosphere, some of these "secondary" ENAs can travel close to the Sun and be observed by IBEX. The ribbon, therefore, is likely formed from secondary ENAs whose intensity is greatest where the observer's line of sight ($\boldsymbol{r}$) is approximately perpendicular to the ISMF ($\boldsymbol{B}$) draped around the heliosphere, i.e., $\boldsymbol{B} \cdot \boldsymbol{r} = 0$. The $\boldsymbol{B} \cdot \boldsymbol{r} = 0$ plane is warped as a function of distance from the heliopause by the draping of the ISMF around the heliosphere (Pogorelov et al. 2011), forming a complex, 3D structure of the ribbon source region as a function of ENA energy (Zirnstein et al. 2015).

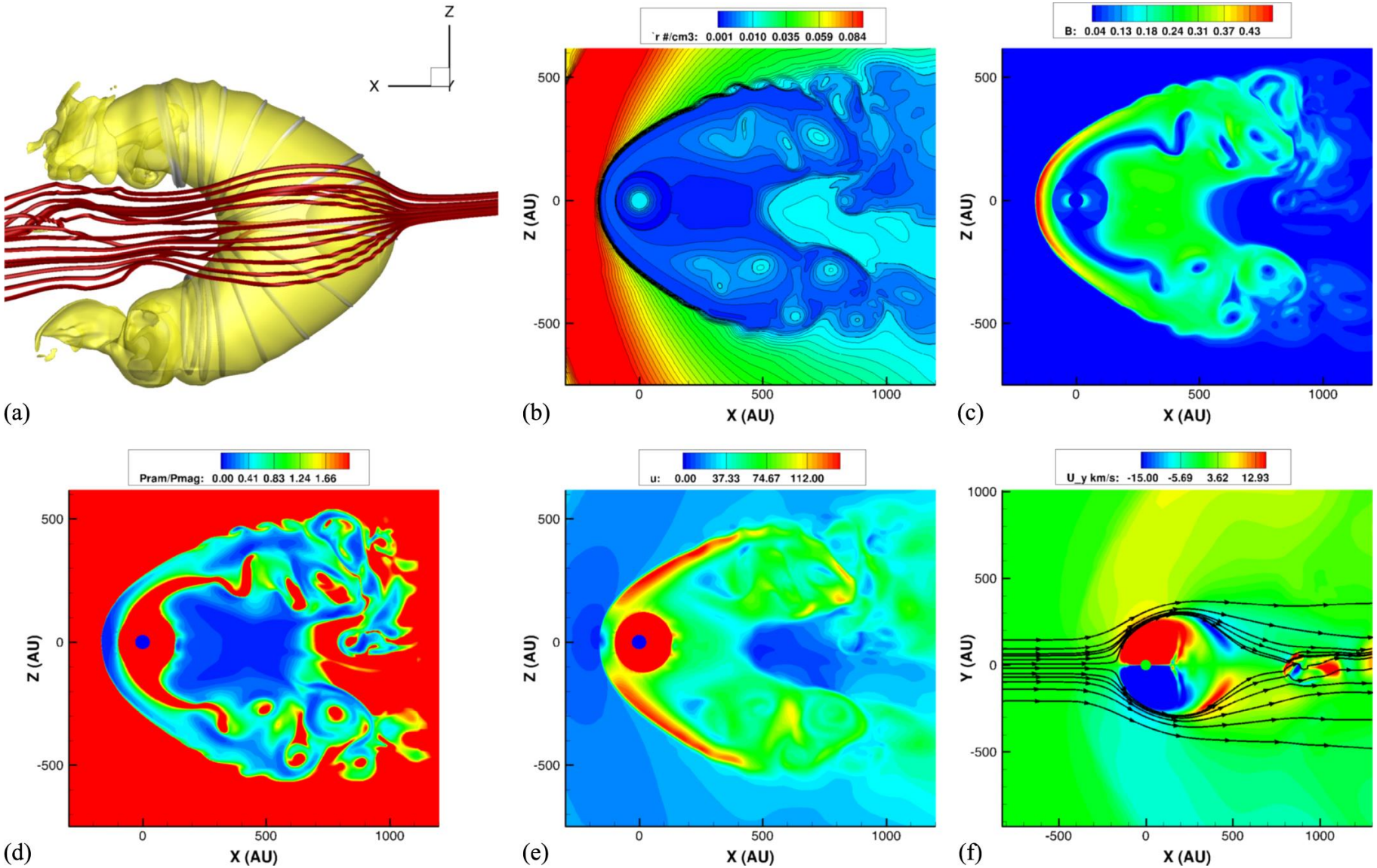
Z
X
(a)
r #/cm3: 0.001 0.010 0.035 0.059 0.084
Z (AU)
X (AU)
(b)
B: 0.04 0.13 0.18 0.24 0.31 0.37 0.43
Z (AU)
X (AU)
(c)
Pram/Pmag: 0.00 0.41 0.83 1.24 1.66
Z (AU)
X (AU)
(d)
u: 0.00 37.33 74.67 112.00
Z (AU)
X (AU)
(e)
U_y km/s: -15.00 -5.69 3.62 12.93
Y (AU)
X (AU)
(f)

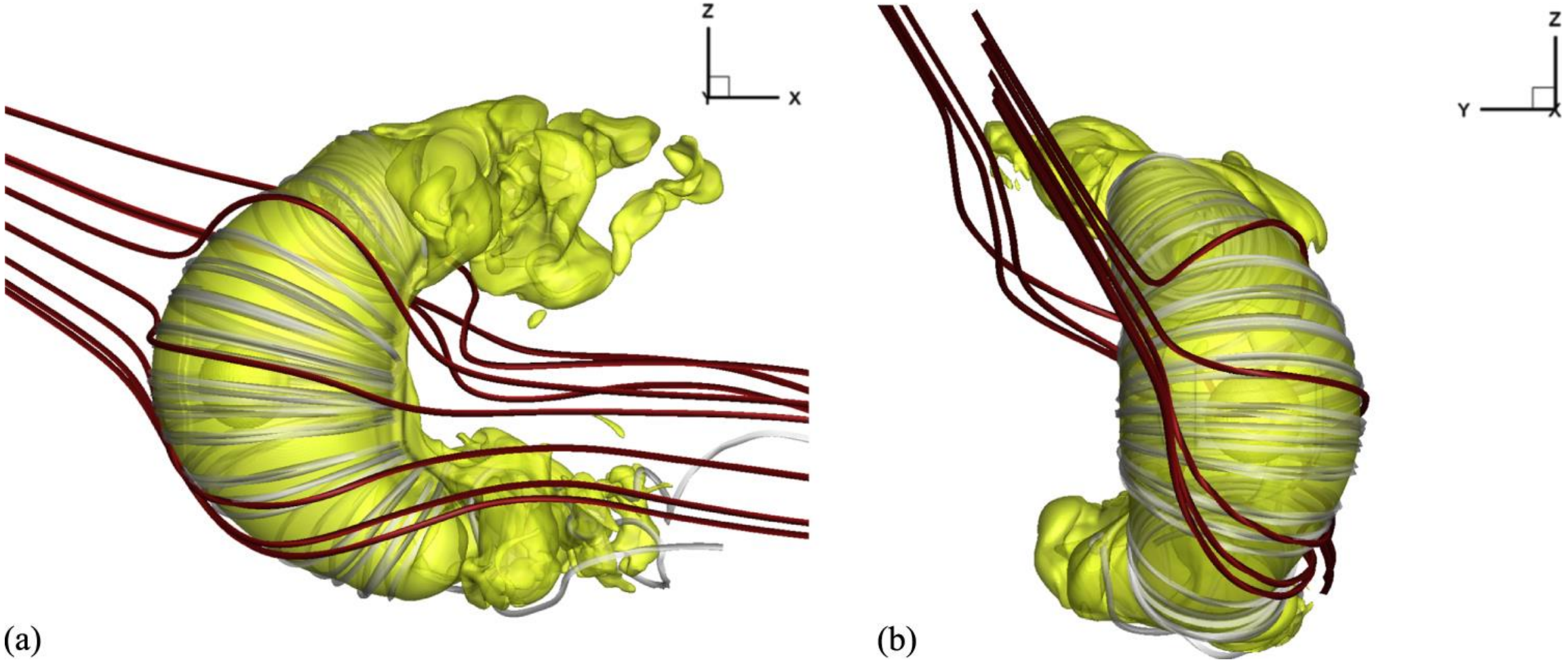
Z
X
Z
Y
(a)
(b)